Peter Lang Langen

Polar Amplification of Surface Temperature Change in a Warming Climate

experiments with an atmospheric general circulation model in a simplified configuration

Ph.D. thesis

Niels Bohr Institute
University of Copenhagen

August 2005

Supervisors:

Vladimir A. Alexeev, Peter D. Ditlevsen and J. Ray Bates

Peter Lang Langen
plangen@gfy.ku.dk

Niels Bohr Institute
University of Copenhagen

Juliane Maries Vej 30
2100 Copenhagen O
Denmark

Supervisors:

Vladimir A. Alexeev
valexeev@iarc.uaf.edu

International Arctic Research Center
University of Alaska Fairbanks

930 Koyukuk Dr. P.O. Box 757340
Fairbanks, Alaska 99775-7340
USA

Peter D. Ditlevsen
pditlev@gfy.ku.dk

Niels Bohr Institute
University of Copenhagen

Juliane Maries Vej 30
2100 Copenhagen O
Denmark

J. Ray Bates
ray.bates@ucd.ie

Mathematical Physics Department
University College Dublin

Belfield, Dublin 4
Ireland

Abstract

Many climate models indicate that, when climate warms, this change is most pronounced at high latitudes. In this thesis, focus is on the mechanisms responsible for this polar amplification. An idealized version of the National Center for Atmospheric Research's Community Climate Model (CCM3) is employed in a series of studies where we seek to understand the mechanisms in simple terms. The degree of idealization varies from substudy to substudy but the model is typically run without a representation of continents (giving a so-called aquaplanet), without sea ice, with annually averaged solar forcing, with uniform specified surface albedo and with either a slab ocean or fixed sea surface temperatures (SSTs). Since these simplifications give the model a number of characteristics in common with the simple energy balance models (EBMs), the relationship between the model and the EBMs is first investigated. In particular, the validity of the EBMs' linear parameterization of the outgoing longwave radiation in terms of local SSTs is assessed and the solution space of the model is investigated. It is found that when a thermodynamic representation of sea ice is included, the zonal symmetry due to the lack of continents gives rise to multiple equilibria reminiscent of those seen in the EBMs.

A statistical analysis based on the fluctuation-dissipation theorem is used to estimate the model response to an external forcing (such as a change in atmospheric CO_2 content) using only the internal variability of the model in a very long run. The linear operator of the system thus reconstructed shows that the polar amplification is a feature inherent to the dynamics of the system even when all feedbacks connected to sea ice are eliminated. A physical explanation of this feature is given and demonstrated in a series of EBM and GCM experiments. It is found that increasing poleward heat transports in a warming climate play a crucial role in warming and moistening the high-latitude upper troposphere. In this manner a low-latitude forcing translates to a longwave forcing at high latitudes. This mechanism hinges on the sensitivity of the meridional heat transport to SST changes and a substudy places further focus on this. It is concluded that in (and around) the present-day climate a uniform increase in temperature will, in fact, lead to increased heat transport. However, the heat transport becomes insensitive to the global mean temperature when warm climate states with weak equator-to-pole temperature gradients are approached. The above mechanism thus predicts polar amplification of climate change around the current regime but fails to explain the very weak gradients inferred from proxy-records for certain periods of the Earth's past.

Finally, the role of temporal cloud variability for the cloud radiative forcing and the change thereof in climate change experiments is investigated. It is concluded that the change in cloud variability associated with a climate change (and not only the change in the mean) plays a part in determining the change in cloud radiative forcing and thus in setting the final magnitude and latitudinal structure of the SST change.

Acknowledgments

The work presented here has been carried out mainly at the Niels Bohr Institute at the University of Copenhagen. However, adding up my three longer stays and two summer schools, I have spent about 9 months at the International Arctic Research Center (IARC), University of Alaska Fairbanks.

Vladimir A. Alexeev has been my supervisor throughout the three years. With Volodya working in Alaska with a ten-hour time difference, we have become very experienced in collaborating via emails, but the most productive times have been my stays in Alaska where a discussion was only a cup of coffee – rather than ten hours – away. I am very grateful for having not only worked, but also gone skiing and fishing, with Volodya. Both in and out of the office, he has been sometimes a collaborator, sometimes an adviser and always a friend.

In Copenhagen, I initially had John Ray Bates as my supervisor. I thank him for his help both with my MSc-work and with getting me properly started with my PhD-work. When Ray got an opportunity to return to Ireland, I was fortunate to get Peter D. Ditlevsen as an excellent replacement. Thanks to Peter for always taking time for discussions of both scientific and non-scientific matters. I am especially grateful for his very thorough reading of the first draft of this thesis.

When I started my PhD, Matt Huber and Rodrigo Caballero were still at the institute. With Matt's knowledge of the CCM3, he was of great help in the beginning. Rodrigo and I have stayed in close contact after he left Copenhagen. I owe him great thanks, both for our collaboration and for encouraging me and Sara to visit him in Chicago.

My stays at IARC and the University of Chicago have been an important part of my PhD-training. The hospitality that I have been met with in Fairbanks amazes me – perhaps the colder the place, the warmer the welcome. Thanks to John Walsh and the rest of the faculty and staff for this. During my one-month stay in Chicago, I was quickly welcomed as a part of the group by Ray Pierrehumbert and the others at the Climate Systems Center. I would also like to thank the developers of the NCAR Command Language (NCL) and the CAM user group who always gave swift and thorough answers whenever I had questions.

Til sidst vil jeg gerne takke min familie og mine venner. Enhver ved, hvor vigtige den slags er, og med den modgang man undertiden kan møde under et PhD-studium, er de bare endnu vigtigere. Sara hører under begge og fortjener den største tak af alle.

Contents

Chapter 1

Introduction

Throughout the age of humans, climate and weather have been considered as something imposed externally on life. Ice-sheets have waxed and waned and rains, snows, droughts and storms have been part of the boundary conditions for the evolution of civilizations, beyond the control of man. These features of nature have frequently been considered either as gods themselves or as consequences of divine actions. Recently (on the time scale of human evolution), however, we have realized that weather is a result of the physical processes governing fluid mechanics, and today (within the last century or so) we are beginning to contemplate that our actions may directly influence it. Who knows?: It may not be entirely inconceivable that we, in the future, may become able to control or design our own climate and weather.

The term "climate" has here been used in a rather intuitive manner, but is usually defined more precisely as the statistical description of weather variables, such as temperature, wind and precipitation, in terms of mean and variance (based typically on 30 year averages, IPCC: Houghton et al., 2001). Instead of its first and higher order moments, climate may also be described in terms of the probability density functions (pdfs) of its variables. To a description of climate belongs also a determination of the characteristic patterns of variability. In a broader context, climate is considered as the state of the climate system comprised of the five components: the atmosphere, the hydrosphere, the cryosphere, the land surface and the biosphere.

The atmosphere is that of the above components which is most intuitively thought of as the key player in the climate system. It is the component first studied in the context of climate and also the one most directly influenced by human emissions of greenhouse gases and aerosols. As such, understanding and prediction of atmospheric flow seems central not only for weather forecasting but also for the field of climate physics. During the 1960's, Lorenz (1963a,b, 1969) laid the foundation for our modern understanding of predictability of the atmospheric flow. He operated with two different classes of deterministic flows: quasi-periodic (or strictly periodic) flows and nonperiodic flows (Lorenz, 1963b). In the former class, the flow will attain a state arbitrarily similar (or identical) to one encountered earlier and the

subsequent evolution of the flow will be arbitrarily close (or identical) to the history of the earlier state. A nonperiodic flow – known today as chaotic flow – may attain a state close to one encountered earlier but the subsequent evolution will not remain close. He studied such a situation in his celebrated 1963-paper (Lorenz, 1963a), in which a three-dimensional set of non-linear differential equations designed to study finite amplitude convection was found have a peculiar solution structure. The phase space trajectories followed a surprising topology, the Lorenz attractor, which seemingly consists of two merging planes (making it look like the wings of a butterfly), but is, as Lorenz described it, an infinite complex of surfaces. It is today recognized as a so-called *strange attractor* and has a fractal dimension of 2.05 (Strogatz, 1998). A characteristic of strange attractors is that nearby phase-space trajectories initially diverge exponentially, and eventually their separation will be of the order of the size of the attractor. This may also be the case for atmospheric flow; in fact, Lorenz (1969) considered a simplified version of the spectral vorticity equation and found that, although deterministic, the resulting flow was essentially unpredictable beyond a certain range due to the exponential growth of small-scale errors. Though careful not to make too strong parallels to the real atmosphere, he deemed it plausible that weather prediction had such an inherent finite range. This range is today believed to exist and take on a value of about 14 days.

With an inherent predictability range of two weeks for (one of) the key players in the climate system, how can we expect to model or predict climate changes with any reasonable accuracy? The answer to this question lies (hopefully) in our earlier definition of climate in terms of moment statistics and pdfs: we will not be able predict a heavy snow shower in central Copenhagen on the afternoon of Christmas day 2087, but we may, when sufficient physical understanding and computer power has developed, be able to say something about typical Decembers in Denmark at that time, in terms of, for example, temperatures, precipitation and extreme events. In terms of the above discussion, we cannot expect to determine the exact phase-space trajectory of our realization of climate, but we may hope to map the gross future changes in the shape of the attractor. One perfect model, yielding the correct representation of all processes and giving the correct distribution of climate variables, is unlikely to be available to us in the near future (When will we know when this is achieved?). Until then we have to rely on the model ensemble comprised by the efforts of the many modeling groups around the world. Not just the mean "consensus" result of this ensemble should be reported; in fact, the pdfs have greater value to decision makers than just the mean (Räisänen and Palmer, 2001; Allen and Ingram, 2002).

The study by Arrhenius (1896) can be thought of as the first climate modeling study, attempting to quantify the changes in the surface temperature resulting from changes in the atmospheric CO_2 content. He evaluated the wavelength dependent absorption of atmospheric CO_2 and water vapor[1] and wrote a simple energy balance equation for the Earth's surface in

[1]Due to the overlaps between CO_2 and H_2O absorption in the 5–20 μm range, part of the water vapor

terms of radiative and turbulent (sensible and latent) heat fluxes. Solving this equation for the surface temperature, Arrhenius arrived at a number of results consistent with what we know today. For example, he realized that the surface temperature change depends logarithmically on the CO_2 change, such that subsequent doublings of CO_2 yield similar temperature increases.

Since then, climate modeling has undergone an ever-accelerating development in several different directions to be reviewed briefly later in this chapter. This includes energy balance models (EBMs), 1-D radiative-convective models (RCMs), 2-D models, general circulation models (GCMs) and Earth system models of intermediate complexity (EMICs). Today we are in a situation where the most comprehensive models (the GCMs) of both the atmosphere and ocean are coupled to each other and to dynamical models of the land surfaces, the cryosphere and, in these very years, the biosphere. These fully coupled comprehensive models are designed to give us the most accurate and detailed projections of future climate changes, but there is still plenty of room left for exploration with the less comprehensive of models. Far from all mechanisms in the system are understood, and this is where simpler models or simplified versions of the comprehensive models come into play. Odd questions sometimes lead to unusual studies and interesting conclusions, and one could for example remove the mountains and see what happens to the temperatures in Northern Europe (Seager et al., 2002) or specify a constant insolation everywhere in an all-ocean world (aquaplanet) and see how the atmospheric circulation organizes itself (Barsugli et al., 2005).

1.1 Forcing, sensitivity and feedbacks

Given the broad spectrum of climate models currently available, simple tools are needed for comparison of their characteristics. The concepts of *radiative forcing*, *climate sensitivity parameter* and *feedback parameters* are such tools. The IPCC (Houghton et al., 2001) definition of *radiative forcing*, ΔF_Λ, is the change in net irradiance at the tropopause resulting from a perturbation in or introduction of an agent, Λ, AFTER letting the stratospheric temperatures adjust to radiative equilibrium. The surface-troposphere system is held fixed during this adjustment process. Once the radiative forcing is determined, the surface and troposphere may be allowed to equilibrate (radiatively and dynamically), and the resulting equilibrium surface temperature change, ΔT_S, can be evaluated. This yields the *climate sensitivity parameter*,

$$\lambda = \frac{\Delta T_S}{\Delta F}, \tag{1.1}$$

where we stress that ΔF is measured before the surface-troposphere system equilibrates and ΔT_S after. We have suppressed the agent-subscript on ΔF for exactly the reason that makes

absorption was ascribed to CO_2 leading to an overestimate of the latter.

the sensitivity parameter a useful tool: It is a (more or less) constant number characterizing a model or climate system independently of the nature of the forcing agent, Λ. While it may vary from model to model, λ yields a first-order estimate of the relationship between forcing and response in a model. This has the useful consequence that the impact of various forcing agents may be estimated and compared without having to run the model to equilibrium for each of them. One only needs to perform the (usually less costly) exercise of determining the radiative forcing and the total change in temperature can be estimated as $\Delta T_{S,tot} = \lambda \sum_\Lambda \Delta F_\Lambda$,where the sum is taken over all forcing agents.

When the climate sensitivity parameters have been determined for a group of climate models, this number can be used to make a model inter-comparison. Based on one number alone, this exercise is not particularly informative; the models may be ranked according to this number, and the mean and ranges may be considered, but the inter-model differences leading to the spread in sensitivity are still unknown. Not until the sensitivity differences can be decomposed on a process-by-process level do we begin to learn about the different merits of the models. To this end, the concept of *feedback parameters* becomes useful. A climate feedback is a process by which a change in one climate variable leads to a change in another which, in turn, leads to a change in the former. If the initial change is amplified (damped) the feedback is positive (negative). Consider a climate system having only the so-called surface temperature feedback by which a radiative forcing, ΔF, leads only to a change in surface temperature and an associated fixed-lapse rate tropospheric temperature change. This is the basic temperature change resulting from the radiative forcing in absence of any other feedbacks, be it, for example, changes in atmospheric lapse-rate, specific humidity, cloud cover, cloud optical properties, or surface variables such as vegetation type, ice and snow covers. Provided that the forcing is small enough for our linear framework to be valid, this non-feedback response can be written

$$\Delta T_0 = \lambda_0 \Delta F, \tag{1.2}$$

and λ_0 is the sensitivity parameter in the absence of feedbacks. General circulation model studies yield a value of this parameter of about 0.3 K/(Wm^{-2}) (e.g., Manabe and Stouffer, 1988; Colman, 2003). If the temperature change, ΔT_0, leads to a change in another climatic variable and thus to a modification of the radiative forcing, the stage is set for climate feedback. Let h_i denote the derivative, $\partial F_i / \partial T_S$, of the tropopause radiation budget with respect to surface temperature owing to the ith feedback process. With this extra forcing, the surface temperature change will be given by

$$\Delta T_S = \lambda_0 (\Delta F + h_i \Delta T_S). \tag{1.3}$$

In the case of multiple feedbacks acting linearly and independently of each other (or "in parallel" with reference to the electrical circuitry jargon from which the feedback concept is

taken), the temperature change must satisfy

$$\Delta T_S = \lambda_0(\Delta F + \sum_i h_i \Delta T_S), \tag{1.4}$$

where the sum is taken over all feedbacks. This solves to

$$\Delta T_S = \frac{\lambda_0 \Delta F}{1 - \lambda_0 \sum_i h_i} = \frac{\Delta T_0}{1 - \sum_i f_i}, \tag{1.5}$$

where we have introduced the *feedback parameter*, $f_i = \lambda_0 h_i$, associated with the ith feedback process. Note that a positive (negative) feedback parameter amplifies (dampens) the final temperature response relative to the non-feedback response. With carefully designed experiments, where changes in relevant fields are either suppressed or sustained, individual feedback parameters may be evaluated. This can, as in the review by Colman (2003), be used to pinpoint processes on which models disagree the most. He found that the inter-model spread in the values of individual feedbacks often was greater than the spread in the net feedback (with clouds yielding the largest uncertainty). The analysis of the climate sensitivity parameter in terms of individual feedbacks thus provides a much richer basis for model inter-comparison.

In the above, the distinction between a forcing and a feedback lies in the definition of radiative forcing. The forcing is the imbalance at the tropopause after stratospheric radiative adjustment and all other processes contributing to the temperature change are part of the feedback system. This distinction works reasonably well as long as the different forcings of the system work in a similar manner. We mentioned earlier that the sensitivity parameter is *more or less* constant with respect to the forcing imposed, but there are cases where this breaks down and not only the magnitude but even the sign of the climate sensitivity depends on the specific agent (e.g., Hansen et al., 1997; Shine et al., 2003). A good example is aerosol forcing, where both the so-called semi-direct and indirect effects are neglected when evaluating radiative forcing as above (e.g, Ramanathan et al., 2001). The semi-direct effect is due to the absorption of aerosols altering the cloud cover locally, while the indirect effect hinges on aerosols affecting the nucleation processes and thus altering the optical properties of clouds. The question then arises whether these effects are forcings or feedbacks. One may consider them as feedbacks, but this leads to inconsistencies in the above framework, since they do not amplify (or damp) *any* forcing agent; they only modify aerosol forcing. If they are considered as part of the forcing, then consistency is maintained, but how does one include in the radiative forcing effects that cannot be detected if the troposphere is to be held fixed?

A solution is to let not only the stratosphere but also the troposphere attain equilibrium after insertion of the agent. This is done by simply fixing the surface temperature (land and ocean) and running the model, an option which has been explored by Alexeev (2003)[2] and

[2]The technique of Alexeev (2003) will be covered in detail in Section 3.1.

Shine et al. (2003) independently of each other. When the surface temperatures are held fixed, the atmosphere attains a quasi-equilibrium in which there is an imbalance in the net energy flux at all levels (surface, tropopause, top-of-atmosphere and all levels in between), but where the divergence of the time-mean flux vanishes. Hence, there is no net heating (or cooling) anywhere in the atmosphere and its temperature stays constant. The imbalance can be measured at any level and Shine et al. (2003) dubbed it the *adjusted troposphere and stratosphere forcing*, ΔF_{ats}. They found the climate sensitivity parameter, calculated as

$$\lambda_{ats} = \frac{\Delta T_S}{\Delta F_{ats}}, \tag{1.6}$$

to be superior to that calculated from eqn. (1.1). Not only did it alleviate the problems with aerosols (for which the standard method was completely useless), it also gave remarkable increases in consistency between the "easier" forcings such as changes in insolation, CO_2 and O_3. Moreover, the method circumvents the non-trivial issue of determining a suitable tropopause level in the model, which one faces in the standard framework.

Changing the atmospheric CO_2 content is the most common climate perturbation experiment (again, cf. Arrhenius, 1896). Especially the "$2\times CO_2$" experiment, in which the CO_2 content is doubled, has become a canonical choice for feedback and process studies as well as benchmarking purposes. Two reasons are obvious: i) The atmospheric CO_2 content *is* increasing (a fact admitted even by the more skeptical side of the global warming debate) due to anthropogenic emissions (IPCC: Houghton et al., 2001). ii) CO_2 is the most important greenhouse gas after water vapor[3].

A negative feedback involving CO_2 and the weathering rate of silicate rocks is believed to stabilize Earth's climate on the extremely long time-scale (Kasting, 1989). 4.8 billion years ago (b.y.), the solar luminosity was roughly 70% of the present-day value and has increased monotonically since. This implies that with present-day atmospheric conditions, Earth should have been completely frozen over prior to about 2.3 b.y., but there is evidence of liquid water as early as at least 3.8 b.y. There have been large temperature excursions throughout the history of Earth – just the last 1 b.y. has seen both deep freezes and very warm periods – but the record indicates that these are oscillations about a state with liquid water. On long time scales, CO_2 is controlled by the following geochemical cycle: Weathering of silicates consumes atmospheric CO_2 and produces carbonates which are deposited on the sea-floor. Here they are subducted downward to levels where high temperatures and pressures reverse the above silicate process. The gaseous CO_2 is then returned to the atmosphere through volcanoes. Since the weathering rate increases with atmospheric temperatures as well as precipitation (which,

[3]The time-scale of water vapor cycling in the atmosphere is, however, so short that human water vapor emissions will not influence the humidity. The processes determining atmospheric humidity are not completely understood, but one could popularly say that the atmosphere "knows" what the right humidity is and adjusts accordingly, regardless of human emissions.

in turn, increases with temperature), and the reverse branch of the cycle depends on neither, high temperatures will lead to a depletion of atmospheric CO_2 and subsequent cooling and vice versa.

On shorter time-scales such as tens of thousands of years, ice-cores indicate that the CO_2 content and the surface temperature follow each other closely (e.g., Petit et al., 1999). This is generally believed to be due to a positive feedback between ocean temperature and CO_2: The solubility of CO_2 in water decreases with temperature and a warming ocean thus releases CO_2 to the atmosphere, which, in turn, amplifies the warming. The oscillations thus seem to pose a hen-and-the-egg problem, but are widely thought to be controlled by Earth's orbital parameters with this feedback (and many others) modifying the response.

Due to this wide range of time-scales of interactions between CO_2 and climate, the CO_2 change experiments serve not only to indicate what the future will bring; they serve to help us understand the workings of the climate system on a more fundamental level. Past, present *and* future. The above framework of climate forcing, sensitivity and feedbacks focuses mainly on global averages of temperature and radiative fluxes[4], but regional aspects and latitudinal structure of the climate change are equally important for the utility of the modeling results. Manabe and Wetherald (1975) were among the first to perform an annually averaged CO_2 doubling experiment with a GCM and thus to begin to determine what the impacts of this would be on the meridional temperature gradient, land-ocean differences, hydrologic cycle, energetics and circulation. Later, Manabe and Stouffer (1980) and Washington and Meehl (1984) coupled their GCMs to a simple representation of the ocean mixed-layer and could thus include the seasonal cycle. The time since has seen thousands of CO_2 doubling GCM studies focusing on all aspects of the system. Some focus, for example, on cloud-climate interactions (e.g, Cess and Potter, 1987; Senior and Mitchell, 1993; Senior, 1999), some on surface budget interactions (e.g, Boer, 1993), some on the momentum budgets (e.g, Rosen and Gutowski, 1992; Räisänen, 1998) and some on cyclone/anticyclone activity (e.g, Zhang and Wang, 1997).

1.2 Polar amplification

One feature common to the bulk of these CO_2 increase GCM experiments is an increasing warming response with latitude, for CO_2-doubling experiments (e.g, Manabe and Wetherald, 1975, 1980; Hansen et al., 1997; Hall, 2004) as well gradual 1% yearly increase experiments (e.g, Räisänen, 2001) and projected CO_2-scenario experiments (IPCC: Houghton et al., 2001; ACIA, 2004). Apart from being the region where the largest climatic changes are projected by the currently available models, the Arctic is also the region where these models disagree the most. In fact, when comparing control runs[5] of 8 coupled atmosphere-ocean GCMs, Walsh

[4]The IPCC (Houghton et al., 2001) quotes 3.7 Wm^{-2} as the best estimate of the $2\times CO_2$ radiative forcing.
[5]Unperturbed present-day conditions.

et al. (2002) find that the inter-model spread in Arctic temperature and precipitation exceeds the projected changes in the 21st century. Nevertheless, the so-called *polar amplification*, i.e., the larger polar response, of surface warming stands out as a very robust result in all kinds of models ranging from the very simplest to the most comprehensive.

Polar amplification is generally ascribed to the positive ice-albedo feedback, which is one of the most classical and instructive illustrations of a climatic feedback loop: Surface warming (cooling) will lead to an advance (retreat) of ice and snow cover. This, in turn, decreases (increases) the surface albedo and thus increases (decreases) the absorption of solar radiation and amplifies the initial warming (cooling). This feedback is, in nature, complicated by a number of factors. For example, clouds can greatly decrease its effect (Cess et al., 1991), while increasing snowfall with temperature is a possible countering mechanism (e.g, Lindzen, 1990). In spite of such effects, the ice-albedo feedback is almost beyond doubt a very important amplifier of high-latitude climate responses (Hall, 2004).

With the presence of such an amplifier, the Arctic seems a good place to look for the earliest signs of an anthropogenic influence on climate: If the globe is warming, it definitely ought to be visible in the Arctic parameters. This has stimulated a massive focus on the Arctic concurrent with the increasing concern of global warming. Possible Arctic warming and associated cryospheric changes are, however, more than merely a harbinger of global warming; it can pose a threat to the sustenance of rich Arctic cultures and terrestrial and marine ecosystems, but also ease industrial development and navigation. The purpose of the Arctic Climate Impact Assessment (ACIA) is to map current trends and possible future climate scenarios for the Arctic along with such negative and positive ecological and socio-economic impacts.

For the period since the 1960s, Chapman and Walsh (1993) have found an Arctic warming of surface air temperatures (SAT) in the winter and spring seasons, which has been corroborated by more recent studies (e.g, Rigor et al., 2000). With some regional specificities, this warming is accompanied by a lengthened melt-season (Rigor et al., 2000; Comiso, 2003) and decreases in both sea ice area (Chapman and Walsh, 1993; Parkinson et al., 1999) and thickness (Rothrock et al., 1999). The trend in sea ice seems associated with a trend in the dominant circulation patterns manifest in phase shifts of the North Atlantic and Arctic Oscillations (Deser et al., 2000). Further, Zhang et al. (2004) have found Arctic summer cyclones to increase in both number and intensity, while Abdalati and Steffen (2001) find a positive melt trend of 1%/yr over the Greenland ice-sheet during the period 1979–1999[6].

While these and other observations indicate that conditions certainly are changing in the Arctic, Polyakov et al. (2002) have studied a 125 yr record of SAT and found previous incidents of comparable warming. More specifically, the SAT and sea ice parameters seem to be controlled by a low-frequency oscillation with drastic warming from 1920–1940, cooling

[6]The trend falls, however, just below the 90% significance level.

from 1940–65 and a subsequent warming. The authors point out that when calculating trends from such a time series they will naturally depend sensitively on the choice of end points. In a combined observation and modeling study, however, Johannessen et al. (2004) found the warming patterns in the two periods to be vastly different signifying different underlying mechanisms. In fact, unforced coupled model runs displayed warming events similar to the early twentieth century warming while anthropogenic forcing had to be added before the late twentieth century warming could be reproduced. This agrees with the findings of Vinnikov et al. (1999), who used another coupled model to estimate that the probability of the 1978–1998 sea ice trend being a natural fluctuation is less than 2%. In conclusion, the early twentieth century warming (and subsequent cooling) is most likely due to natural variability while the later trend seems anthropogenic in origin.

Polar amplification has, as mentioned, been seen in even the simplest models, but there it typically owes exclusively to the ice-albedo feedback (but not in always; Chen et al., 1995; Bates, 2003). In this thesis, focus is on those mechanisms leading to polar amplification unrelated to the ice-albedo feedback. Schneider et al. (1999) studied the tropospheric water vapor feedback[7] in a GCM configuration where sea ice was excluded and found a polar amplified response to doubled CO_2 (without looking closer at it, though). The model had continents on which the snow cover could be part of a snow-albedo feedback, but the polar amplification is most likely a result of the non-albedo mechanisms focused on here. Alexeev (2003) (hereinafter A03) employed an even simpler model configuration (the same as employed here), in which both continents and sea ice was excluded, and also found a significantly polar amplified response. The amplification was described as a property of the linear dynamics of the system (see Section 3.1), but here we go a step further and look at the actual physical mechanisms behind it.

The strong stratification of the high-latitude troposphere is often quoted as the most important mechanism – after the ice-albedo feedback – leading to polar amplification (e.g, Hansen et al., 1997), but the results to be presented here (Section 3.2) indicate that more non-local effects are at play. In fact, several investigators have found that a tropical sea surface temperature anomalies can have global ramifications (e.g, Schneider et al., 1997; Rodgers et al., 2003) and a similar idea is the basis of the our investigations. Outside the subtropics, mid-latitude eddies dominate the poleward atmospheric heat flux (e.g, Holopainen, 1965), which consequently will depend on the meridional temperature gradient. It was early on suggested that, in the absence of an ice-albedo feedback, the poleward eddy transport of latent heat could contribute to a polar amplification due to the increased efficiency of the eddies in a warmer and moister atmosphere (Manabe and Wetherald, 1980). Graversen (2005) studied the mean Arctic SAT trend in the period 1958–2001 and concluded that a significant portion of it may be associated with the atmospheric poleward energy transport, but it was not detailed

[7] Warming leads to increased humidity which again leads to increased greenhouse effect.

what the relative roles of latent and dry static energy transports were. In the present thesis, we study a simple mechanism for increased heat transport leading to polar amplification. We argue that the nature of the mechanism is such that it is difficult to identify by simply comparing the equilibria before and after the CO_2 perturbation (as was done in Manabe and Wetherald, 1980).

1.3 Simple climate modeling

All climate models considering the atmosphere are based in some way on the fundamental governing equations of atmospheric motion, temperature and humidity. Kiehl (1992) very elegantly demonstrates how the different climate models arise as results of different types of averaging of the governing equations. For example, the simplest conceivable model, the zero-dimensional energy balance model, arises when the equations are averaged vertically, horizontally[8] and over time. What remains is a requirement that balance exists between the absorbed solar radiation and the outgoing longwave radiation (OLR). This model is a widely used pedagogical introduction to climate modeling since even with very simple principles and parameterizations it has a rather interesting behavior. If the OLR is given by some monotonically increasing function of the global average temperature (see discussion of energy balance models and Section 2.1) and the albedo is given by a decreasing function of temperature which saturates at low (ice-covered) and high (ice-free) temperatures, the model can exhibit three equilibria. One is unstable, while the two others correspond to stable warm and cold climates. Such multiple equilibria are seen in various types of climate models (see Section 2.2) and are frequently used (at least conceptually) when interpreting proxies of past climates.

When the governing equations are averaged only horizontally, a set of time-dependent equations for the globally averaged vertical atmospheric profile remains. This type of one-dimensional model is frequently called radiative-convective models (RCMs) and in this field the studies of Manabe and Strickler (1964) and Manabe and Wetherald (1967) have played a large role. The former were the first to numerically solve this set of equations incorporating both radiative and convective effects (convection was included by dynamically adjusting the lapse rate to be less than the moist adiabatic lapse rate). While absolute humidity was fixed in the former, the latter employed the more observationally justifiable assumption of fixed relative humidity. This had the effect of increasing the absolute humidity and, in turn, tropospheric opacity to longwave radiation with temperature, and thus led to inclusion of the water vapor infrared feedback. This type of model is very useful for simplified studies of the effects of increasing greenhouse gases (e.g, Manabe and Wetherald, 1967; Augustsson and Ramanathan, 1977; Ramanathan, 1981; Lindzen et al., 1982) and the interplay between stratospheric and upper tropospheric variables and the surface temperature becomes readily

[8]Both *meridionally* (along meridians) and *zonally* (along latitude circles).

apparent. Temperature dependent surface albedo has been employed and the models can thus be used to study the increase in climate sensitivity due to the ice-albedo feedback (e.g, Wang and Stone, 1980) and the possibility of multiple equilibria (e.g, Li et al., 1997). The interaction of the albedo feedback with the atmospheric variables in this kind of model should, however, be interpreted cautiously due to the way in which the modeled atmospheric profile is to represent the global mean atmosphere. This global mean atmosphere may be quite different from the actual polar atmosphere that encounters the ice-covered surfaces.

The latitude-dependence of the albedo is a main ingredient of the one-dimensional energy balance climate models (EBMs), which arise when the governing equations are averaged vertically, zonally and in time. In 1969, two papers were published where zonally averaged models were constructed in order to study a variety of climate change scenarios (Budyko, 1969; Sellers, 1969). The models incorporated solar radiation (and albedo), OLR and meridional heat transports. The energy balance equation as obtained through the above averages appears as,

$$Q(\phi)(1-\alpha(\phi)) - F_{LW,TOA}(\phi) = H(\phi), \tag{1.7}$$

where ϕ is latitude, Q the incoming solar radiation at the the top of the atmosphere (TOA), $F_{LW,TOA}$ the OLR, α the albedo and H the meridional redistribution of heat.

For the OLR, Budyko utilized a parameterization in terms of the surface temperature,

$$F_{LW,TOA} = A + BT_S - (A_1 + B_1 T_S)n, \tag{1.8}$$

where A, B, A_1 and B_1 are positive constants and n is the fractional cloud cover. In the form where the cloud terms are left out, this relationship has in many ways become the standard way of parameterizing the OLR and its validity in our GCM configuration is investigated in Section 2.1. Sellers used a slightly different parameterization of the infrared radiation but when linearized it agrees with Budyko's to within about 5% (North, 1975a). Budyko parameterized the meridional heat transports linearly in the difference between the local temperature and a planetary mean temperature, while Sellers used many different terms representing the individual atmospheric and oceanic processes. Albedos are in both models calculated for each latitude band in terms of observed present day albedos, model temperatures and ice-line latitudes.

Tuned to present day climate, the two models were used to project consequences of changes in various forcings, such as increased volcanic activity, changes in atmospheric infrared transmissivity and even changes in anthropogenic heat release. Large variations in the extent of the polar ice-caps were found and a completely ice-covered Earth was concluded to be a possible consequence of reductions in the solar constant of 1.6% for the Budyko model and 2% for the Sellers model. Chýlek and Coakley (1975) reconsidered the Budyko model making a few simplifications enabling them to solve the system analytically for the latitude of the ice-line.

In addition to the completely glaciated state, two other solutions were found. One corresponds to the present day situation (with the ice-line situated at approximately 72°) while the other represents an ice-cap extending to much lower latitudes ($\sim 35°$). When the solar constant is decreased, the two solutions approach each other, and at the critical reduction of 1.6% they merge at $\phi = 50°$, leaving the fully glaciated state the only solution.

G. R. North has made important contributions to the field of EBMs (including a couple of excellent reviews: North et al., 1981; North, 1990). By representing the meridional distribution of solar radiation in terms of a second order Legendre polynomial[9] and using a diffusive heat transport, North (1975a) obtained qualitatively the same multi-branch solution structure as Chýlek and Coakley but was able to perform a stability analysis. The branch containing present day conditions and the branch of complete glaciation were found to be stable while the intermediate branch is unstable. In a second paper, North (1975b) took the Legendre approach a step further: All latitude dependent quantities were expressed in terms of Legendre polynomials allowing him to easily consider the effects of changing details of his diffusive heat transport. The constant diffusion coefficient, D, employed in his previous paper was shown to be equivalent to Budyko's representation of heat flux when using the two-mode model. In Section 3.2 we will consider how a diffusion coefficient dependent on the global average temperature can lead to polar amplification of a climate change in an EBM.

An intriguing feature of the EBMs' solution structure is the occurrence of the so-called Small Ice Cap Instability (SICI). In the diffusive versions of the EBMs, a narrow range of solar insolation values (close to that of present day) exists for which both an ice-free climate and a present-day-like climate are steady state solutions, while ice caps of smaller size than about 20° from the pole are unstable (e.g, North, 1975a). This behavior is also encountered in two-dimensional (vertically averaged only), seasonally resolved EBMs (North et al., 1983; Mengel et al., 1988; Lin and North, 1990), and has been proposed as a mechanism for initiation of the Greenland and Antarctic ice sheets (e.g, North and Crowley, 1985). North (1984) studied the phenomenon in mathematical detail and was able to account for its existence and non-existence in the different types of EBMs employing different representations of the horizontal energy transport. The SICI essentially owes to a typical length scale in the models which is proportional to the square root of the ratio between the diffusion constant, D, and the radiative damping, B. This is the typical distance a temperature anomaly performing a random walk will propagate before it is damped out radiatively. This length scale is for typical parameter settings about 20° and implies that a temperature anomaly at the pole will influence temperatures down to about 70°. If a small polar ice cap is introduced, it effectively corresponds to a heat sink, and if this heat sink (ice cap) is large enough to depress temperatures within its radius of influence below the freezing point, the ice cap will grow to that size. If not, the temperature anomaly will be damped out and removed. This effect will

[9]See Appendix C. North argues that retaining only the first two terms in the Legendre expansion suffices to yield 2% accuracy in the mean annual heating function.

be touched upon briefly in Section 2.2.

In the opposite end of the range of possible EBM steady states lies the deep frozen climate, the so-called *Snowball Earth*. There is geological evidence that the Earth at least once between 750–580 Ma has realized this state and stayed in it for millions of years (Hoffman et al., 1998). With an EBM incorporating the effects of variable CO_2-concentration, Caldeira and Kasting (1992) estimated that a partial CO_2 pressure of about 0.12 bar is necessary to melt back the ice once the snowball Earth is attained. According to the theory, the deep freeze shuts down the hydrologic cycle and thus inhibits the previously discussed removal of atmospheric CO_2 through silicate weathering, allowing CO_2 levels to increase. With current volcanic outgassing rates, the estimated duration of such an event would be about 4 million years. Whether the Earth actually froze over completely or it still had a band of open ocean along the Equator ("slushball Earth") remains a matter of debate (Hyde et al., 2000). EBMs and some atmospheric GCMs coupled to mixed-layer ocean models readily enter the snowball state with near-present CO_2 levels and appropriately reduced solar constant (e.g, Jenkins and Smith, 1999; Baum and Crowley, 2003). In other studies (e.g, Hyde et al., 2000), the advance of the ice-line is halted before the equator, and especially inclusion of a fully coupled ocean component seems to exclude the full glaciation (Poulsen et al., 2001). Recently, Pierrehumbert (2004) used a GCM to estimate the CO_2 levels necessary for deglaciation. He found that effects such as decreased lapse rates and lowered summer troposphere heights weaken the greenhouse effect enough for his model to be far from deglaciation even at a partial CO_2 pressure of 0.2 bar. This makes the question of how the Earth came back from the deep freeze a more difficult one than previously anticipated (Hoffman et al., 1998), and may lend support to the near-snowball solution from which deglaciation occurs at much lower CO_2 levels (Crowley and Hyde, 2001). Pierrehumbert stresses, however, that his results do not necessarily rule out the snowball state; many feedbacks not included in the model (such as those involving CO_2 clouds) may become important at the very cold temperatures and high CO_2 levels.

The details of these Late Proterozoic cold spells are not just interesting as a testing ground for climate modelers; they may have exerted massive selective pressure on the evolution of life and can thus help to explain the so-called Cambrian explosion of multi-cellular animal life that took place in the aftermath of the last deglaciation (Hoffman and Schrag, 2000).

1.4 General circulation models

Whereas the governing equations were averaged in some way to yield the simplified models, the unaveraged equations are the basis of general circulation models (GCMs). Hence, equations for velocity, temperature, pressure and humidity are integrated forward in time numerically and these solutions and derived fields define the model climate. The GCMs have evolved from numerical weather prediction models and the two disciplines have a lot in common. Basically the same equations are solved using the same techniques, but there are differences. Whereas

a weather prediction model focuses on the finer details of the flow and runs are short, a GCM experiment is more focused on the longer-term statistics and conservation of energy, mass, moisture and momentum suddenly become issues (McGuffie and Henderson-Sellers, 2001).

A basic characteristic of a GCM is its underlying grid. For the governing equations to be solved numerically, the continuous fields must be represented by a finite amount of numbers. The earliest and perhaps most intuitive approach is to cover the globe with a latitude-longitude grid (in several vertical layers) and represent the three-dimensional field by its grid-point values. An alternative approach, which is widely used today, is to represent the fields by a truncated series of spherical harmonics (again in several vertical layers). Spherical harmonics are a natural choice for problems such as these with spherical geometry, and, for example, circumvent a number of problems that the finite difference grid has at the poles. The efficiency of such *spectral models* is improved by the so-called transform method by which non-linear terms are calculated on a physical grid (grid space) and then transformed back to the spectral grid. A product term, for example, requires $\mathcal{O}(M^2)$ operations (where M is the number of Fourier coefficients) if it is performed in spectral space. With the transform method, the fast Fourier transform is used when going to and from grid space (requiring $\mathcal{O}(M \log M)$ operations) where the product is calculated (requiring $\mathcal{O}(M)$ operations). In total, the method thus reduces the number of operations from $\mathcal{O}(M^2)$ to $\mathcal{O}(M \log M)$ (Durran, 1999).

Atmospheric processes take place on a wide range of temporal and spatial scales. Some, like the jets and the meridional overturning, have almost global scale, while others, like convection, cloud formation and boundary layer turbulence, are localized and of small scale. Modern GCMs typically have a horizontal resolution of about 250 km and about 20 layers in the vertical, while time-steps are about 15-30 minutes. The truncation of both the finite difference grid and the spherical harmonics thus implies that processes smaller than some scale are unresolved. Unfortunately, these unresolved, *sub-grid scale*, processes have a non-negligible influence on the resolved scale fields and this influence must somehow be included or *parameterized*. A parameterization is a way of using the state of the resolved scale fields to include the statistical effects on them by a process taking place on the unresolved scales. Processes routinely parameterized in GCMs include longwave and shortwave radiation transfer, cloud processes, convection, surface energy exchange, atmospheric boundary layer processes, vertical and horizontal diffusion processes and vertically propagating gravity waves (Hack, 1992, IPCC, 2001).

The first GCM experiments are probably those reported in two companion papers by Smagorinsky et al. (1965) and Manabe et al. (1965). Prior to that, model integrations had been performed, but typically only with two levels in the vertical and very limited spatial domains (e.g, Phillips, 1956; Smagorinsky, 1963). In the 1965 models, the primitive equations were integrated for the whole northern hemisphere on a grid with 9 vertical levels and a horizontal resolution ranging from about 320 km at the equator to 640 km at the pole.

Radiative transfer and convective adjustment was done as in the RCM study of Manabe and Strickler (1964), described earlier. Smagorinsky et al. (1965) excluded the effects of condensation (apart from the convective adjustment of the lapse rate), while Manabe et al. (1965) included both convective and non-convective condensation and thus treated the water vapor mixing ratio as a prognostic variable. As lower boundary condition the former had a land surface with vanishing heat capacity such that the surface temperature adjusted to balance upward and downward fluxes. The latter had a wet surface of zero heat capacity to ensure a supply of moisture to the atmosphere. To limit the degrees of freedom and permit comparability between the studies, both used a climatological distribution of water vapor in the radiation calculations. The models were able to simulate important aspects of the observed general circulation; the vertical structure as well as jets, cells and waves were well captured and the model including the hydrologic cycle was able to simulate the hemispheric average precipitation quite accurately. There were, however, considerable discrepancies, for example, the strength of the mid-latitude jet was too strong and ratios between various forms of energy (such as eddy kinetic energy and zonal kinetic energy) were far off. The moist model also had problems specific to the hydrologic cycle, for example, the tropical moist region and the subtropical dry regions were exaggerated.

Since then, many different GCMs have developed and parameterizations, boundary conditions, numerical techniques and resolutions have improved. A part of this world-wide development effort is inter-comparison projects, in which certain aspects of the simulated GCM climates are compared to determine the level of certainty and uncertainty in the modeled processes and projections (Cess et al., 1990, 1991, 1996; Colman, 2003, IPCC, 2001). Treatment of clouds, both their formation and their interaction with long- and shortwave radiation, is recognized as the main reason for uncertainty in the state-of-the-art atmospheric GCMs (IPCC, 2001). In fact, the available GCMs disagree not only on the strength, but also on the sign of cloud feedbacks.

Whereas the GCMs have been developed concurrently with the simpler models discussed before (RCMs and EBMs), a relatively new class of models have developed within the last decade. In Earth Models of Intermediate Complexity (EMICs), detail is generally sacrificed for the sake of computational efficiency and of including many components of the climate system (Claussen et al., 2002). Many different models are considered EMICs, but common to all of them is that they try to include the whole climate system; atmospheres may be represented by coarse resolution GCMs, two-dimensional statistical-dynamical models or even EBMs and oceans may likewise be represented by very different model types. Some include carbon and vegetation dynamics and some include two- or three-dimensional ice cap models. The different model types are often thought of as members of a climate model *hierarchy*, but Claussen et al. (2002) propose that the word *spectrum* is a better choice. GCMs (and coupled atmosphere-ocean GCMs, AO-GCMs) do include more detail and are the closest to reality, but depending on the question one wants answered, EBMs, RCMs or EMICs could also be the right models

to employ.

1.4.1 The Community Climate Model Ver. 3

The GCM used here is the National Center for Atmospheric Research's Community Climate Model ver. 3 (Kiehl et al., 1998a). The CCM3 is the fourth generation of the atmospheric GCMs developed at NCAR. The model, being a community model, is very well documented, the code is well commented and freely available on the web and it is rather easily installed across various computer architectures. It is written in Fortran 77.

The first generation of CCMs, CCM0, was released in 1983 and was followed by the second generation (CCM1) in 1987, which included a number of changes to the formulation and model climate. The third generation (CCM2), which was released in 1992, had undergone major changes from its predecessor, both in terms of parameterizations of clouds, radiation, moist convection and the planetary boundary layer and in terms of implementation and portability. The easily accessed model available today can be seen as a result of this revision. The CCM3 was released in 1996 and included important changes to the physical parameterizations as well as some minor changes to the dynamical core. Some of the changes were made to address some of the systematic errors in the CCM2, while others were made to make it suitable for coupling to ocean, land and sea ice components under the Climate System Model framework (CSM1).

The CCM employs the spectral transform method whereby horizontal derivatives and linear operations are calculated with the fields represented by spherical harmonics (wavenumber space), and nonlinear calculations are performed with the fields represented on a physical grid (grid space)(Durran, 1999). The horizontal resolution is for such a model normally reported in terms of its spectral truncation, and the standard resolution of the CCM3 is T42. This means that it employs a triangular (T) truncation, such that its maximum zonal and meridional wave numbers are the same and equal 42. This corresponds roughly to a grid space resolution of $2.8^\circ \times 2.8^\circ$. It has 18 levels in the vertical and these follow a so-called hybrid-σ grid[10]. In the lowermost layers, this grid employs σ-coordinates (pressure normalized by surface pressure) to make the coordinates terrain following. Up through the atmosphere, a gradual transition is made toward the pure pressure coordinates in the topmost layers.

The forward integration in time is based on a time-splitting approach. First, fields are updated according to the so-called tendency physics, such as clouds, radiation, surface exchange (of momentum, energy and moisture), vertical diffusion and gravity wave drag. Second, the fields are transformed back and forth between grid space and wavenumber space to update according to the dynamical tendencies (including horizontal diffusion). Finally, the fields are updated by the adjustment physics, namely mass flux convection, large scale stable condensa-

[10]We will in many parts of the thesis use a horizontal resolution of T21 (see discussion in the following subsection) but 18 vertical levels are always used.

tion and dry convective adjustment. After this final adjustment, the time-stepping is complete and a new loop can begin. The user does not see the spectral part of the code; all input and output operations are performed on the physical grid.

We cannot describe all the parameterizations in the CCM3, and the interested reader is referred to Kiehl et al. (1996) which gives a thorough account of all physical and numerical aspects of the model formulation. However, since we will be focusing on some of the specifics of the cloud parameterization in Chapter 4, this will be introduced shortly here. The clouds in the CCM3 are diagnostic (as opposed to prognostic in many newer GCMs) and depend on relative humidity, vertical velocity, atmospheric stability and convective mass flux. The total convective cloud amount is diagnosed from the strength of the parameterized moist convective activity and this total amount is distributed evenly among the convective layers. Frontal and tropical low clouds are diagnosed based on vertical velocity and relative humidity, while low-level stratus is diagnosed from the inversion strength and relative humidity. Finally, middle and upper level clouds are calculated from the relative humidity and static stability of the column. Once the presence of a cloud is determined, the cloud liquid water path is calculated from the absolute humidity profile. The fraction of cloud water in the form of ice and effective radii of ice and liquid droplets are calculated from the temperature and pressure at the cloud's level. These quantities are then used to determine the cloud's optical parameters, and finally, the collective effect of several cloudy layers is determined using an assumption of random overlap (see Chapter 4).

The CCM3 includes seasonal and diurnal cycles and model components for land surfaces and sea ice. A 15 yr control run was performed at NCAR with sea surface temperatures specified as the observed monthly mean values from 1979 to 1993. The results of this run are reported in a series of papers in the Journal of Climate from June 1998 (Kiehl et al., 1998a,b; Hack et al., 1998; Hurrell et al., 1998). Amplitude and position of the main features of the upper-tropospheric circulation are realistically reproduced by the model. Observed patterns of sea surface pressure and mid-latitude storm tracks are also well represented. Compared to Earth Radiation Budget Experiment (ERBE) measurements, the model's top-of-atmosphere budget is very good both in annual and seasonal means. At the surface, the shortwave flux is too large over oceans and this is attributed to an underestimate of the shortwave cloud absorption. Other model biases are associated with the tropical deep convection in the Pacific and summertime convection over land areas. Marine stratus and stratocumulus clouds are not very well represented in the model either. The zonally averaged moisture field is, although somewhat too dry, in reasonable agreement with observations. In spite of the mentioned (and other) biases, the implied oceanic heat transport (calculated from surface imbalances) compares favorably with that of the uncoupled ocean component of the CSM1. In fact, CSM1 was one of the earlier coupled AO-GCMs to sustain a stable climate without flux-corrections[11].

[11] Flux corrections are artificially inserted fluxes at the atmosphere-ocean interface designed to stabilize a

After the Climate System Model (CSM) project was started, it was decided to change the nomenclature. Hence, the atmosphere component was called Community Atmosphere Model (CAM) and the successor of the CCM3 was released in 2002 under the name CAM2.0 (Kiehl and Gent, 2004). This model had undergone major changes since the CAM3, both in terms of software engineering and in terms of science. It was written in Fortran 90 and many subroutines had been updated to exploit the added functionality of this language. The order of the calculations within a time-step had been re-organized to accommodate for more efficient parallelism. On the science side, changes were, for example, made to the cloud water scheme: a prognostic cloud water scheme replaced the diagnostic one of the CCM3, while the cloud fraction was still diagnosed as in CCM3. The cloud overlap assumption was changed to one of maximum-random overlap, which means that adjacent cloud layers are assumed to be maximally overlapped while they are randomly overlapped if there is a gap between them. This model still had some serious biases (such as low tropical tropopause temperatures and errors in the structure of the Inter-Tropical Convergence Zone (ITCZ)) and already in 2004 the CAM3 was released. In this model, changes have been made to the parameterizations of moist processes as well as radiation and aerosols (Collins et al., 2005), and this has improved the simulations significantly. For example, tropical tropopause temperatures, surface insolation and clear-sky surface radiation in polar regions are more realistic. There are, of course, still biases and model development continues at NCAR.

When my PhD-work was started in 2002, the CAM2 had just been released so it seemed obvious to use that model. However, this release did not include the option of running in slab ocean (mixed-layer) mode. This, combined with the fact that the model was so new that its reliability had yet to be established, caused me to choose the not-quite-state-of-the-art CCM3.

1.4.2 The simplified setup

As the inquiries in this thesis are concerned with zonal average large-scale mechanisms in the atmosphere-surface system, a variety of simplifications have been made to the standard distribution of the CCM3. These have been made to ease both the execution of the experiments and the interpretation of the results. When the setup is increasingly simplified, the model will naturally have less and less direct resemblance with the actual climate system. It is our belief that the mechanisms that are left in the model are the most fundamental ones and therefore also the ones most generally applicable over wider ranges of climate states and configurations. In a sense, the simplified model can be viewed as an intermediate one between the near-realistic GCMs and the simpler EBMs. An interplay between models from all parts of the spectrum helps us advance our understanding of the system.

coupled model run.

Our main simplifications are the removal of continents and the seasonal cycle. This leads to a model with complete zonal symmetry[12] and complete symmetry between the hemispheres.

Lower boundary

We have removed the continents such that the lower boundary is an all-ocean surface. Such a configuration is known as an *aquaplanet*. Sea surface temperatures (SSTs) can either be prescribed by the user (fixed-SST mode) or can be calculated interactively based on the energy fluxes in and out of the surface. The latter is done using a so-called slab ocean or mixed-layer model. The idea is simple; the current state of the surface temperature field and of the overlying atmosphere yields a certain set of surface fluxes, which are calculated by the atmospheric part of the model. These fluxes are then used to update the surface temperature field at the next time step according to

$$\rho_w c_w H \frac{\partial T_S}{\partial t} = F_{SW} - F_{LW} - F_{SH} - F_{LH} + q, \tag{1.9}$$

in each grid-point. Here, F_{SW} and F_{LW} are the net downward shortwave and net upward longwave fluxes at the surface, respectively, while F_{SH} and F_{LH} are the upward fluxes of sensible and latent heat. The term q owes to a specified oceanic heat flux (see discussion later). The mixed-layer model has depth H (set to 50 m over the entire globe throughout the thesis) and the gain or loss of heat is assumed to be distributed throughout the column instantaneously. Hence, T_S is not only the SST, it is actually the temperature of the whole mixed-layer. The fluxes on the right hand side of eqn. (1.9) have units of Wm^{-2} and one m^2 has a heat capacity of $\rho_w c_w H$, where ρ_w and c_w are the density and specific heat capacity of sea water, respectively.

In Sections 3.1 and 3.2 we add a so-called *ghost forcing* (Hansen et al., 1997) to the mixed-layer to see how the climate system responds to a forcing directly on the surface budget. This is done by simply adding an extra term to the right hand side of eqn. (1.9). As the forcing is inserted directly into the tendency equation for the mixed-layer temperature, it has no direct physical counterpart such as greenhouse gas or insolation changes.

In many of our experiments we wish to examine how the atmosphere responds to some surface temperature perturbation. In those cases, we run the model in fixed-SST mode, whereby the above update of surface temperature is by-passed and the temperature is simply specified by the user. Most often, a zonally symmetric profile of surface temperatures is taken from an earlier equilibrium run with the mixed-layer model (with or without a perturbation added). This will be described in more detail whenever it is done.

In all but one section (2.2), we have excluded the effects of sea ice. This is done by simply by-passing the sea ice part of the code and thus treating sub-freezing grid-points as open

[12] Zonal symmetry = symmetry along latitude circles.

water. To further suppress any surface albedo feedbacks, we have also by-passed the albedo calculation when running the model without sea ice. In that case, we simply specify the albedo at a globally uniform value which depends on the specific experiment. It is used to tune the model to reach a present-day-like meridional temperature profile when run in mixed-layer mode. The standard choice is 0.11 when T21 horizontal resolution is employed – in case of a different choice, this will be discussed.

Specified oceanic heat transport

A heat flux to the mixed layer from below (a *q-flux*) is included as a simple parameterization of the ocean circulation. If oceanic heat transports are neglected, the model (when run with sea ice) is unable to render a climate remotely similar to that presently observed. When no heat is added to the lowest ice-layer the sea ice thickness and extent grows unrealistically large giving climates with sea ice edges at mid-latitudes (30° to 40°) and ice thicknesses of tens of meters.

This is an expected feature of mixed-layer configurations since in the real world a substantial amount heat is transported polewards by the oceans (e.g, Trenberth and Caron, 2001). A common approach to this problem is to use a q-flux which is determined as minus the surface budget in a specified SST run (e.g., Rind and Chandler, 1991; Rind et al., 1995, 1997). Some investigators choose to use q-fluxes that vary over the seasons in correspondence with the SSTs used to determine them (Watterson et al., 1997; Hewitt et al., 2001; Nazarenko et al., 2001), while others use the annually averaged values (Cohen-Solal and Le Treut, 1997, 1999). A different approach is taken by Pollard and Thompson (1994) who use a zonally symmetric distribution and introduce a number of additional fluxes to limit sea ice in specific regions such as the Norwegian Sea. Poulsen et al. (2001) compare various representations of ocean heat transport in modeling of the Neoproterozoic snowball Earth and conclude that vertical mixing at the sea ice margin is crucial to halting the sea ice at mid-latitudes. This mixing results in sharp spikes immediately equatorward of the sea ice edge and depends on a number of specific oceanographic conditions, rendering it difficult to parameterize in a mixed-layer model.

We have chosen to design a smooth q-flux to avoid possible effects of these spikes determining the position of the sea ice edge. Moreover, a smooth q-flux will not introduce arbitrary spikes in the surface fluxes that the atmosphere will need to maintain to keep the system in equilibrium. According to eqn. (1.9), any flux inserted through the term q must in equilibrium be balanced by the remaining terms on the right hand side.

A polynomial-shape heat flux was devised having a maximum at 20° latitude and zero transport at the equator and at the poles. This is shown in Figure 1.1(a), where the solid line has a maximum transport of 1 PW (=10^{15} W). Minus the derivative (i.e., the convergence) of this transport yields the amount of energy deposited in each grid-point and is shown in panel (b) of the figure. This is the q-flux inserted into the model, and since its antiderivative

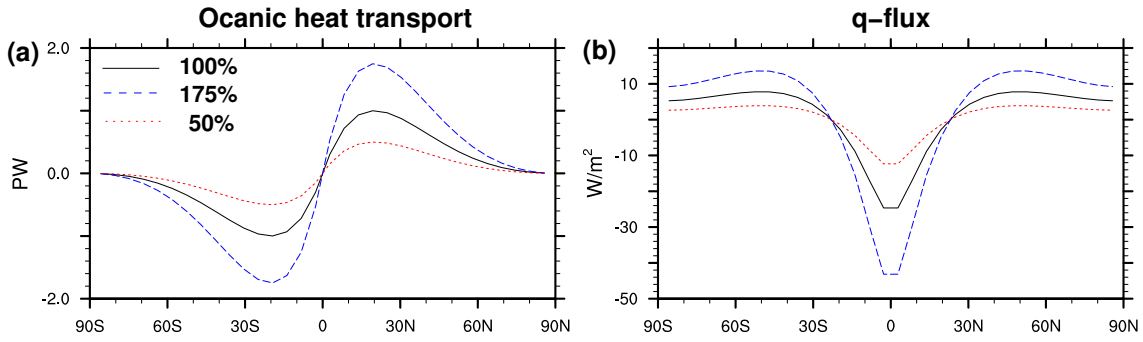

Figure 1.1: (a) Meridional oceanic heat transport as implied by (b) the q-flux (or meridional heat flux convergence) used in the model. Black line is called strength 100 (1 PW transport), while the red and blue lines are strengths 50 and 175, respectively.

vanishes at both the equator and the poles, it averages to zero over each hemisphere. The magnitude of the q-flux can then be varied by simply scaling the solid line. The fluxes obtained by multiplying it by 1.75 and 0.5, for example, are shown by the dashed and dotted lines. When the model is run without sea ice, the standard choice for the q-flux is the weak one shown by the latter.

Solar insolation

The model is run without the seasonal cycle in the solar insolation. A common way of obtaining this is to use perpetual equinox conditions. The problem with this is that, at equinox, the poles receive 0Wm^{-2} while on annual average they receive about 180Wm^{-2}.

To get the annual average insolation at each latitude each day, we have employed "modified equinox conditions" (Alexeev, 2003) as follows. The cosine of the zenith angle was sampled in every grid point each day at 00:00 GMT for a year. The average of these samples gives a zenith angle pattern describing the annual average insolation at 00:00 GMT. Shifting it 15° to the west gives the annual average insolation one hour later and so forth. The pattern is thus shifted from east to west with a periodicity of 24 hours thus forcing the model with an annually averaged diurnal cycle.

Resolution

Choosing the appropriate resolution for a GCM experiment will always become a trade-off between accuracy and computational cost. Investigators must first analyze the experiment and the questions to which they seek answers. They must determine which degree of detail is necessary to answer these questions and how long they are prepared to wait for the answers given the hardware available to them.

Since the time of the very first GCMs, developers have been performing experiments in

which resolution has been increased and the output checked for improvements or convergence (Manabe et al., 1970). This exercise is an important one for understanding the strengths and limitations of the particular combination of suites of dynamics and parameterizations employed in a model and will continue to be an integral part of model development. The tests are performed both for the present-day climate (e.g., Williamson et al., 1995), cold climates such as the Last Glacial Maximum (e.g., Dong and Valdes, 2000) and future warming scenarios (e.g., Senior, 1995). Alternative types of experiments are also performed in which the dynamical core is coupled to a simplified set of parameterizations or in which dynamics and parameterizations are employed at different resolutions (e.g., Williamson, 1999; Pope and Stratton, 2002).

If a general conclusion is to be drawn from this line of investigations, it is that, for spectral models, the major changes are seen when going from low resolution (e.g., T21 or R15[13]) to medium resolution (T42), while slighter changes are seen when proceeding (to T63, T106 or higher). This holds for many statistics of the simulated climate but not for all – as Williamson et al. (1995) put it: *resolution in itself is not a panacea.* In the CCM2, scrutinized by those authors, the T42 version generally agreed better with observations than the low-resolution versions, but it was stressed that this was not always the case. Moreover, some of the problems with the T42 simulation were not remedied by increasing resolution to T63 or T106.

All of the above mentioned resolutions are, of course, much coarser than the turbulent dissipative scales. The effect of the smaller scales on the resolved scales must be parameterized and as seen in Straus and Ditlevsen (1999) the wave number regime 20-40 includes important upscale energy transfer and downscale enstrophy transfer. These transfers are resolved at T42 resolution while they must be parameterized at T21, implying a greater fidelity of the representation of the synoptic-scale eddies in the former.

Throughout the present thesis, however, we are generally concerned with zonally averaged large-scale mechanisms and transports (which are reasonably well represented at T21 resolution), and our questions require either very long runs (Section 3.1), many parallel runs for exploring parameter spaces (Sections 2.1 and 2.2) or memory-consuming re-sampling runs (Chapter 4). For these purposes, T21 was deemed the most practical resolution. In Section 3.2, where greater focus was placed on the details of the transports and surface budgets, T42 resolution was employed.

1.5 Outline

The simplified configuration of our model, as described above, has a number of similarities with the EBMs. In Chapter 2 we look closer at this relationship; in particular, we test the validity of the linear Budyko-Sellers parameterization of the outgoing longwave radiation

[13]R stands for rhomboidal (rather than triangular) truncation. R15 and T21 have similar degrees of freedom with the rhomboidal truncation having its resolution concentrated in mid-latitudes (Durran, 1999).

(Section 2.1). We also study the existence of multiple equilibria allowed in the model due to inclusion of sea ice effects in such a zonally symmetric configuration (Section 2.2).

Chapter 3 is the central chapter focusing on the polar amplification of surface warming. First, we consider the model's dynamics in terms of its linear sensitivity operator (Section 3.1). Secondly, we perform EBM and GCM experiments through which the mechanisms leading to polar amplification (without albedo feedbacks) are explored (Section 3.2). Finally, we take a closer look at the dependence of the meridional heat transport on surface temperature to determine whether increases in this quantity can explain certain outstanding features of the geologic record (Section 3.3).

As corollaries to Sections 3.2 and 3.3, we find that, in our model, clouds tend to strengthen the polar amplification and that their variability has a cooling effect. In Chapter 4, we focus on these cloud effects.

A conclusion is given in Chapter 5, while Appendices A, B and C describe the symbols and abbreviations used throughout the thesis, the calculation of implied transports and Legendre polynomials, respectively. Finally, a list of references is given.

> A great deal has been written on the influence of the absorption of the atmosphere upon the climate (Arrhenius, 1896).

As true as this statement may have been in 1896, when Prof. Svante Arrhenius performed his seminal study of the influence of atmospheric CO_2 change on climate, it is even more so today. With the present thesis, one further contribution has been added to the bulk of literature pertaining to the field of climate change.

Chapter 2

EBMs and the simplified GCM

Before proceeding in Chapter 3 with our study of the polar amplification issue we first devote the present chapter to an investigation of the relationship between our simplified GCM configuration and the much more simple energy balance models. The validity of one of the EBMs' most central parameterizations, namely the linear relationship between surface temperature and outgoing longwave radiation (OLR), is scrutinized in Section 2.1 based on Langen and Alexeev (2005b). In addition hereto, we investigate the phase space and solution structure of our simplified GCM when a simple thermodynamic representation of sea ice is included. This is done in Section 2.2 which is based on the work of Langen and Alexeev (2004). As it turns out, the model displays a variety of multiple equilibria reminiscent of that encountered in EBMs.

2.1 The Budyko-Sellers OLR parameterization

As we discussed in Section 1.3, energy balance climate models have been used with great success in idealized studies of climate stability and sensitivity (e.g., Budyko, 1969; Sellers, 1969; North, 1975b) and have provided us with a tool to recognize the potential richness of the solution structure of the climate system (North, 1990). After the initial introduction in their simple form EBMs have been used more widely in two-dimensional versions (latitude-longitude, e.g., North et al., 1983) and as upper boundary conditions in a hierarchy of ocean modeling experiments (e.g., Nakamura et al., 1994; Marotzke and Stone, 1995; Lohmann et al., 1996). In this manner EBMs are still used for both research and teaching purposes.

The principal strengths of EBMs are their low computational cost and their tractability to analytical solutions (North, 1975a), both features that rely on simple parameterizations of the energy fluxes in the climate system. One such parameterization is the commonly used linear relationship,

$$F_{LW,TOA} = A + BT_S, \tag{2.1}$$

between the outgoing longwave radiation (OLR), $F_{LW,TOA}$, and the sea surface temperature, T_S. This is an empirical relationship linking the top of the atmosphere OLR to the local temperature at the surface and we will in the present section focus on the non-local effects that the atmospheric circulation has on this relationship and on the problems they pose.

By neglecting variations in the fractional cloud coverage Budyko (1969) was first to employ eqn. (2.1). Sellers (1969) used a more complicated form of the dependence which, however, is linear to within 1% in the interesting range of temperatures (North, 1975a). The value of the parameter A is of rather little importance for the stability and sensitivity of a given climate model. In fact, A is often used to tune the temperature to match a certain target profile (e.g., Warren and Schneider, 1979). Conversely, the parameter B has major influence on the behavior of EBMs and numerous studies have focused on determining the optimum value (e.g., Warren and Schneider, 1979; Graves et al., 1993). Despite the many efforts, there still exists quite a wide range of possible values: Marani (1999) sums up previous estimates to lie between about 1.5 $\mathrm{Wm^{-2}K^{-1}}$ and 2.3 $\mathrm{Wm^{-2}K^{-1}}$. The round-number value of 2 $\mathrm{Wm^{-2}K^{-1}}$ is often chosen when EBMs are used for qualitative rather than quantitative purposes (e.g., Alexeev et al., 2005, and Section 3.2).

One reason for the ambiguities in the determination of B is the inability of eqn. (2.1) to deal sufficiently with the effects of tropical convection. While the range of tropical temperature variations is rather limited, observations show large variations in OLR from one tropical region to another (Bess et al., 1989). Low values of OLR are seen in regions with high-level cloudiness and cold cloud tops associated with convective activity, while high values are found mainly over deserts characterized by subsidence and clear skies. Such a difference in regimes has led researchers to construct parameterizations for clear and cloudy skies separately, both in modeling studies (Thompson and Warren, 1982; Gutzler and Stone, 1986) and in observational studies (Graves et al., 1993; Raval et al., 1994). Thompson and Warren included the vertical mean relative humidity along with surface temperature as a predictor of OLR and devised a parameterization from curve fitting the output of a detailed radiative model. These predictors were observationally confirmed by Raval et al. to yield good results; they argue that the moisture field, which has large influence on the OLR, is most directly represented by the column-integrated precipitable water, but since this field is so tightly coupled to the temperature field, use of relative humidity provides more independent information. In a GCM study, Gutzler and Stone conclude that inclusion of a measure of the atmospheric lapse rate as a co-predictor with surface temperature is useful when considering results from climate change experiments. Both relative humidity and lapse rate are influenced by the large scale circulation (such as the Hadley cell) and thus provide information about the non-local conditions which in the present section will be argued to have dominant influence at low latitudes. This was also found by Allan et al. (1999) who explained the occurrence of low-latitude regions with OLR and surface temperature being anti-correlated in terms of seasonal shifts of the Hadley cell and interannual variations in the Walker circulation.

As will be done in the following, Short et al. (1984) worked in terms of spherical harmonics in their appraisal of eqn. (2.1): Using one year of Nimbus-6 data they performed a spherical harmonic expansion of the time varying temperature and OLR fields. Variances and covariances calculated in terms of these expansions were concluded to be dominated by the largest space and time scales. Higher order contributions to the OLR variability which are not nearly as pronounced in the temperature variability were attributed largely to cloud variability in tropical convection regions. Eqn. (2.1) was found to hold quite well in mid to high latitudes and this explains its success in modeling even the seasonal cycle in EBMs: It works where it has to, i.e., in the large low heat capacity continental interiors at mid and high latitudes.

The error made when neglecting the very cold cloud tops in the linear relationship of eqn. (2.1) is by Short et al. argued to be countered by a similar error in the albedo (where the effect of the high tropical clouds is also neglected), such that the net effect is a reasonable representation. According to Pierrehumbert (2004), however, the atmosphere (humidity, vertical stratification etc.) changes drastically in cold extremes such as Snowball Earth scenarios. This may cause a breakdown of the above fortuitous cancellation of errors and exemplifies the potential hazards of extending linear relationships tuned to present day conditions into vastly different climate regimes. On the same note, Warren and Schneider (1979) speculate that the high value of $B \approx 3$ $\mathrm{Wm}^{-2}\mathrm{K}^{-1}$ found over Antarctica may imply that a glacial world is subject to stability conditions unlike those of today. As proposed by Short et al. it may also simply be due to a combination of high altitudes and low surface temperatures.

Due to the nature of the available observations, the present day latitudinal variations and seasonal cycle are commonly used to determine parameterizations of the OLR (e.g., Short et al., 1984; Raval et al., 1994). However, Neeman et al. (1987) demonstrated, by comparing their variable-cloud-top-temperature and fixed-cloud-top-altitude parameterizations of the OLR, that successfully reproducing the present-day seasonal cycle is not sufficient for climate change studies. The two parameterizations yield similar seasonal cycles but imply a factor of 2 different sensitivities to solar constant changes. Similarly, the improvement in the parameterization that Gutzler and Stone (1986) gained from inclusion of lapse rate as a co-predictor was present only in climate change scenarios, and not in present day runs. We speculate that the re-organizations of the large scale circulation that render the lapse rate useful as a predictor are not captured by present day variations. The perturbations introduced in the present study consist of zonally symmetric spherical harmonics and thus span the zonally symmetric parts of both present day climate variations and climate change scenarios.

First, we describe the experiments and the two different GCMs employed therein. Next, the results are presented and discussed before a conclusion is offered.

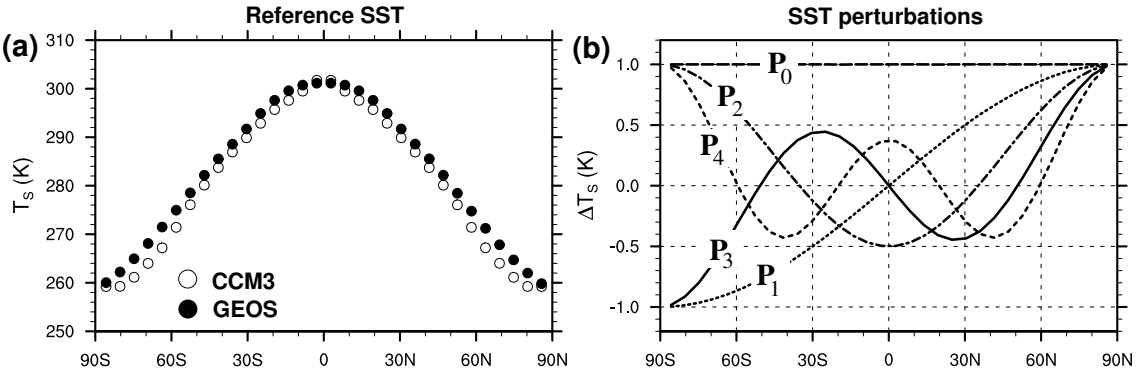

Figure 2.1: (a) Reference SST profiles for the two models. These are results of 20 yr runs with mixed-layer ocean models. (b) In the following experiments, SSTs were fixed at these reference profiles with Legendre polynomial perturbations added. The five first are shown.

2.1.1 Experimental configuration

The model runs necessary for this study were already performed with the Goddard Space Flight Center GEOS model by Vladimir Alexeev for a different publication (i.e., Alexeev, 2003). However, we wished to redo the runs with the more modern CCM3 including clouds and the results of both models are thus presented throughout the following. Both models are run with aquaplanet boundary conditions and without the seasonal cycle (employing "modified equinox" conditions). The GEOS model is run at 4°x5° horizontal resolution with 20 layers in the vertical and the clouds removed from the radiation code (as described by Alexeev, 2003), while the CCM3 is run at T21 horizontal resolution with 18 levels in the vertical and the full physics package included. Our modifications to the standard distribution of the model are as described previously; specifically, we exclude all effects of sea ice, i.e., the surface albedo is uniform and fixed and subfreezing grid-points are treated as open water. The solar constant and CO_2 concentration are set to 1367 Wm^{-2} and 355 ppm, respectively.

Before the experiments were started, both models were run with 50 m mixed layer oceans such that the SSTs were allowed to equilibrate. The surface albedo was tuned in both models to yield SST profiles similar to present-day zonally averaged SSTs. The models were then run for 20 years in their respective equilibria and the SSTs were averaged over this period and symmetrized zonally and about the equator. The resulting SST profiles are termed the reference profiles and are plotted in Figure 2.1(a).

The actual experiment consists of a set of 17 fixed SST runs with both models: A reference run where the SST is fixed at the reference profile and 16 perturbation runs where the SST profiles are perturbed using the 16 first zonally symmetric spherical harmonics, i.e., zonally symmetric perturbations where the meridional structure is given by the 16 first Legendre

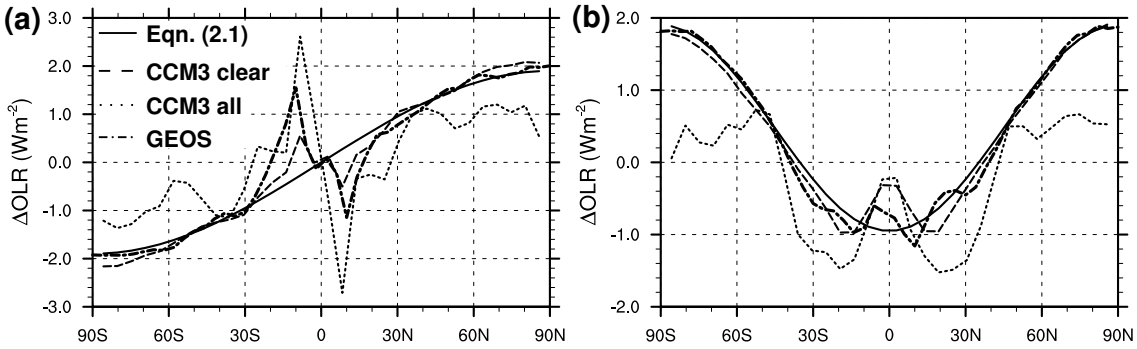

Figure 2.2: OLR changes in the first (a) and second (b) order perturbation experiments. Shown are the CCM3 clear-sky, CCM3 all-sky and GEOS model changes. The solid line is what the change would be if eqn. (2.1) holds exactly. The CCM3 all-sky case (including effects of clouds) clearly deviates the most from this linear prediction.

polynomials in $\sin\phi$:

$$P_0(\phi) = 1, \quad P_1(\phi) = \sin\phi, \quad P_2(\phi) = \frac{1}{2}(3\sin^2\phi - 1), \quad ...$$

The first five perturbations are illustrated in Figure 2.1(b) and Appendix C provides a short review of the properties of Legendre polynomials.

While our truncated series naturally omits the smallest scale features, the zonally symmetric spherical harmonics span all possible zonally symmetric perturbations. Apart from this mathematical property (which any basis possesses) the spherical harmonics are appealing since they are readily envisaged and can partially be related to physical processes and fields: The lowest even-order harmonics describe the typical large-scale patterns in climate change experiments such as global warming and polar amplification. The first asymmetric harmonics describe both the seasonal cycle and possible hemispheric asymmetries in climate changes. Intermediate scales (of either parity) are needed when effects of continents are to be addressed, and the highest wave numbers can be related to more localized features such as, for example, glaciers or oceanic upwelling areas.

All plots in the following are averaged zonally and over 20 years of fixed SST perturbation runs.

2.1.2 Results

In Figure 2.2 we have plotted the result of the first and second order polynomial perturbation experiments. The solid lines show the specified SST increases multiplied by 1.9 $\mathrm{Wm^{-2}K^{-1}}$ and thus represent (the shape of) the changes in OLR one should see if eqn. (2.1) holds. The value $B = 1.9$ $\mathrm{Wm^{-2}K^{-1}}$ was chosen simply to facilitate the comparison and actually agrees quite well with the optimum value of 1.93 $\mathrm{Wm^{-2}K^{-1}}$ arrived at by Short et al. (1984).

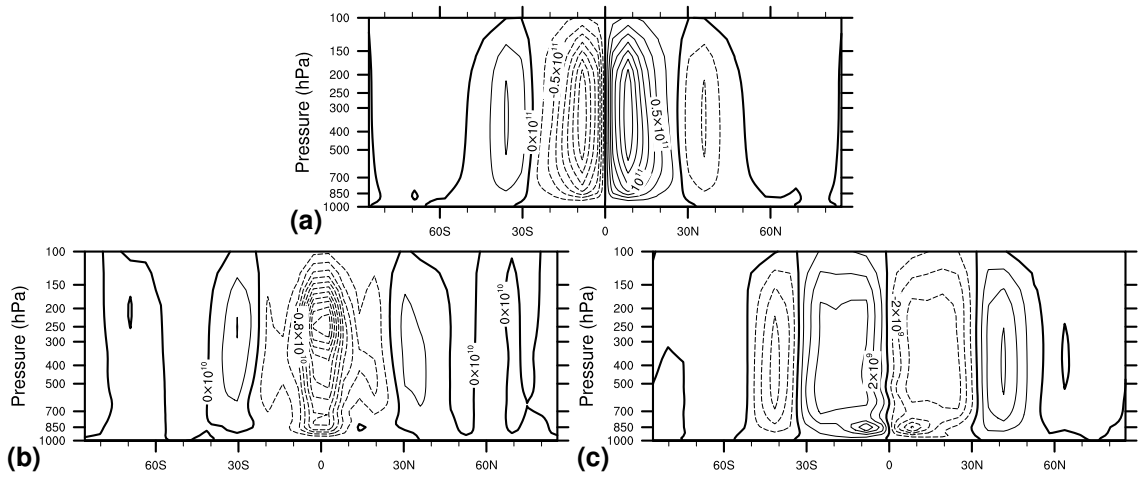

Figure 2.3: Zonal mean meridional stream function (kg/s) in the CCM3 model. (a) Stream function in reference climate and changes when going to first (b) and second (c) order polynomial perturbation. Under the first order perturbation (asymmetric) the ITCZ shifts to the warmer hemisphere, and under the second order perturbation (symmetric) the Hadley circulation weakens.

The dotted lines show the changes in all-sky OLR while the dashed lines show changes in clear-sky OLR, both for the CCM3 model. The former is the actual change while the latter is a diagnostic calculated internally in the code using the real temperature and moisture field but neglecting effects of clouds. The dash-dotted lines show OLR changes in the GEOS model which has clouds removed from the code implying that the changes correspond most directly to the CCM3 clear-sky changes. In general, there is a fairly good correspondence between the actual and expected change in OLR. This is especially true at high latitudes in the clear-sky cases (dashed and dash-dotted), while with clouds there is generally an underestimation of the amplitude of the change poleward of $\sim 50°$. This has to do with the very large cloud cover in the reference case (not shown) which, in fact, tends to shield the OLR change: Much of the OLR comes from the cloud tops such that when the surface temperature changes without the clouds changing significantly, the OLR effect from the surface is damped.

In both the clear and all-sky cases the asymmetric perturbation yields a change in the OLR of the opposite sign in the off-equatorial region. In the symmetric case this region shows an overestimation of the change while the equatorial region shows and underestimation of the change. These are features that clearly demonstrate the failure of eqn. (2.1) in low latitudes. The problem is that a local relationship like eqn. (2.1) cannot adequately model the changes in dynamics that follow from the perturbations. Figure 2.3 demonstrates these changes in the CCM3: Panel (a) shows the zonally averaged meridional stream function in the reference case where the Hadley cells clearly stand out. Panels (b) and (c) show the changes in the stream function in the first and second order perturbations, respectively. The former is characterized by a large negative region centered over the equator; this is the footprint of a shift of the

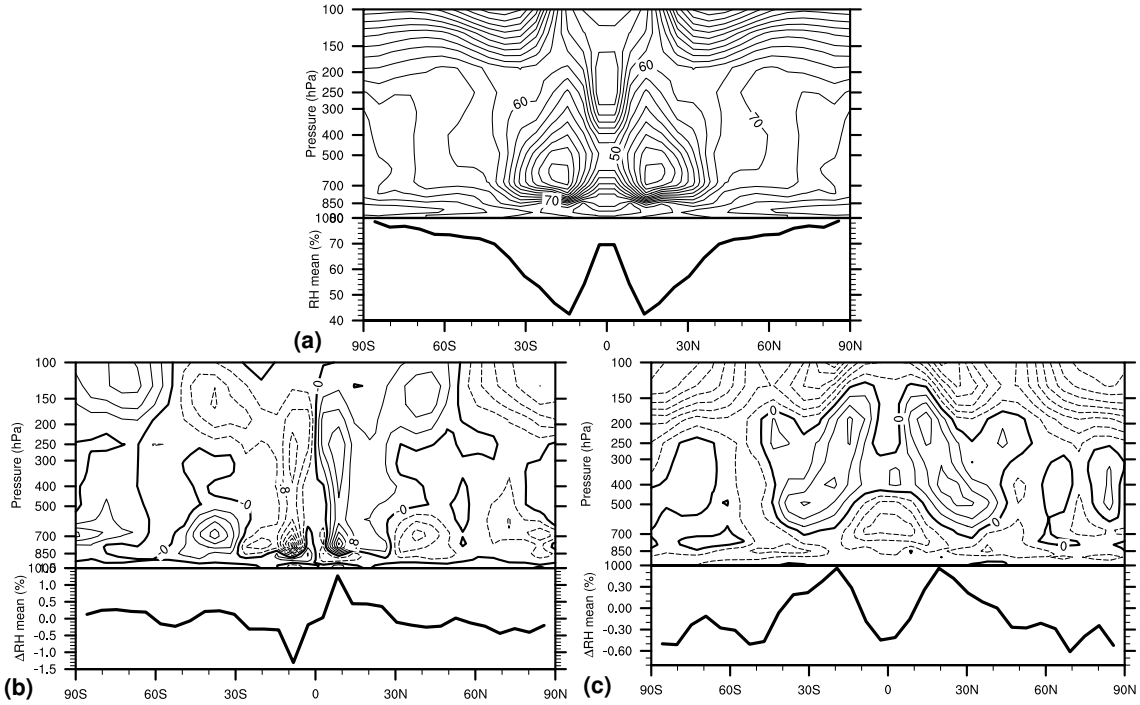

Figure 2.4: Relative humidity (%) in the CCM3. (a) Reference climate with height-mean attached, and change when going to first (b) and second (c) order polynomial perturbations. The stream function changes shown in Figure 2.3 lead to characteristic changes in the RH field.

ITCZ (and the whole Hadley cell structure) into the Northern (warm) hemisphere. Panel (c) shows a weakening of the circulation due to the decrease in meridional temperature gradient accompanying the perturbation. The importance of these changes for the OLR is due to the fact that the tropical moisture field is controlled mainly by the dynamics rather than the local temperature structure. Figure 2.4(a) shows the zonally averaged relative humidity (RH) field where the ascending branch of the tropical circulation is seen to be characterized by high values and the descending branch by low values. In panel (b), showing the changes associated with the asymmetric perturbation, we see a northward shift of the RH field while in panel (c), corresponding to the symmetric perturbation, a moistening of the descending branch and a drying of the ascending branch are seen. The small line-plots attached to the 2D plots show the height-mean relative humidity,

$$\widehat{RH} = \frac{1}{H}\int_0^H RH(z)dz, \tag{2.2}$$

which, as mentioned in the introduction, was shown by Thompson and Warren (1982) and Raval et al. (1994) to be an efficient co-predictor of OLR. The value of $H = 12$ km was found by Thompson and Warren to work well and is employed here. Raval et al. put forth that the success of this definition of $\widehat{RH}$ rather than the more intuitive pressure-weighted average may stem from its preferential weighting of the upper-tropospheric moisture field. The reference profile (panel (a)) of this number reiterates the influence of the circulation on the moisture field. The changes compare very well with the discrepancies in Figure 2.2: In panel (a), the downward spikes in the OLR in the Northern hemisphere are positioned exactly in the same place as the upward (moist) spike in Figure 2.4(b) and vice-versa for the Southern hemisphere. In panel (b) of Figure 2.2, the overestimation of the off-equatorial OLR decrease coincides with the moistening seen in Figure 2.4(c) due to the decreased strength of the Hadley cell. Likewise, the underestimation of the decrease over the equator coincides with the drying.

Determining the linear sensitivity parameter, B

A value of the sensitivity parameter, B, has been determined for each of the perturbation experiments by performing area-weighted linear regressions of the changes in OLR with the changes in SST. In the zero-order case, of course, the regression fails since all points have the same SST change, and here we have simply taken the area-weighted ratio of the OLR change to the SST change. For all perturbations, in both the clear-sky and all-sky cases, the above regression was performed using the whole globe, the tropics (30°S-30°N) and the extra-tropics (poleward of 30°S and 30°N), respectively. The result is shown in Figure 2.5 where panel (a) displays the all-sky case, panel (b) the clear-sky case and panel (c) the results from the GEOS model. The solid lines are for the whole globe, the dashed lines are for the tropics and the dotted lines are for the extra-tropics.

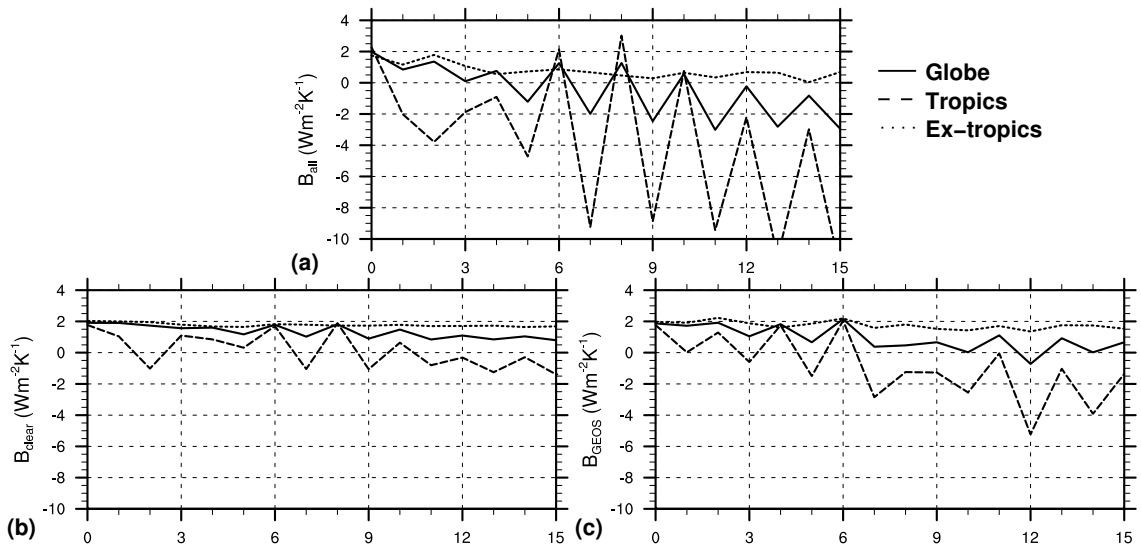

Figure 2.5: Estimates of the sensitivity parameter, B, as function of the polynomial order in the perturbation. (a) CCM3 all-sky. Solid: based on whole globe, dashed: tropics, dotted: extra-tropics. (b) and (c) as in (a) but for CCM3 clear-sky and GEOS model, respectively.

In the all-sky case (panel (a)) we see large variations in the estimate for B, especially at low latitudes; a result that seems rather discouraging for EBMs' ability to model the all-sky tropics. The high-latitude estimate is reasonable for large scale perturbations but as higher wave numbers are approached the above mentioned high-latitude cloud shielding effect tends to dominate and the sensitivity tends to zero. At higher wave numbers, the asymmetric perturbations yield highly negative estimates for B. This is a consequence of the effect that was discussed above for the first asymmetric perturbation: The entire meridional circulation changes position and the resulting changes in the relative humidity field and especially the cloud field yield OLR changes with no connection to the local temperature change.

Considering still the CCM3, the high-latitude estimate of the sensitivity is rather consistent in the clear-sky case (panel (b)): It does not vary much with wave number and its value is close to the canonical value of ~ 2 Wm^{-2}K^{-1}. This is not the case at low latitudes where we already at wave number 2 see that the large underestimation of the OLR change in the ITCZ (Figure 2.2(b)) causes the slope of the regression line to become negative. It is important to stress that this negative value does not imply that a local rule holds in the tropics saying that the OLR decreases with increasing SST. It simply reflects the complete breakdown of any local relationship in the tropical region. Going towards higher wave numbers, the odd order perturbations tend to cause more problems for the low-latitude estimate than do the even order perturbations. This seems to imply that when considering small scale perturbations in the CCM3, the strength of the meridional circulation is less sensitive than its position – the effect of shifting the Hadley cell is more pronounced than the effect of changing its strength.

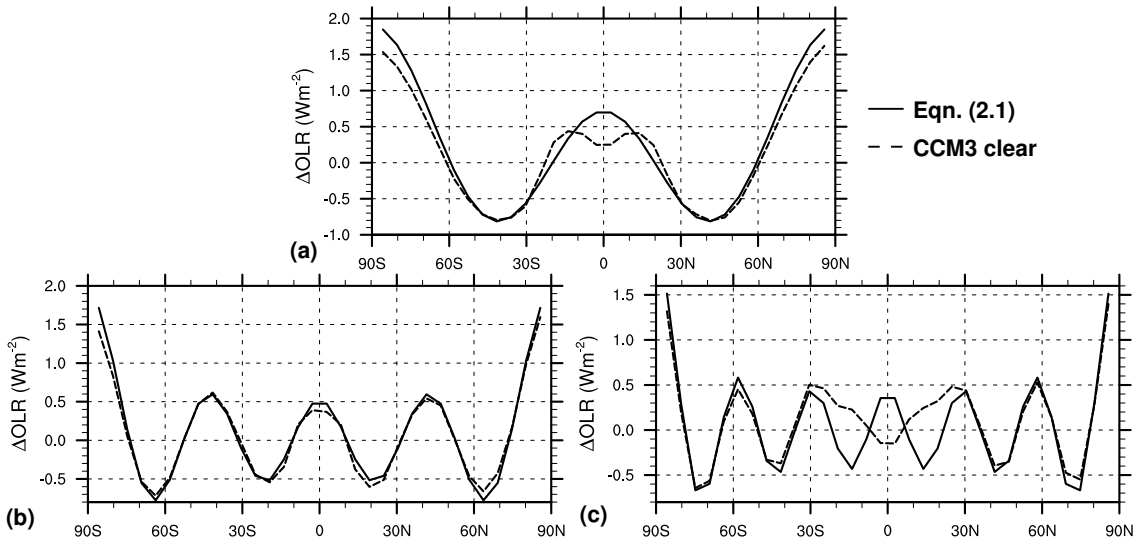

Figure 2.6: As in Figure 2.2 but for fourth (a), eighth (b) and twelfth (c) order perturbations. Solid: SST change multiplied by $1.9 Wm^{-2}K^{-1}$, dashed: CCM3 clear-sky. While deviations from the linear prediction are seen in (a) and (c), the intermediate wavenumber perturbation (b) yields a convincing match.

The global estimate of B stays positive throughout the range of wave numbers but influenced by the tropical failure of the parameterization the value tends away from 2 $\mathrm{Wm^{-2}K^{-1}}$ at higher wave numbers. An interesting exception is the value at wave numbers 6 and 8 where all three regions (globe, tropics, extra-tropics) yield almost perfect results. The reason for this is illustrated in Figure 2.6 where results from wave numbers 4, 8 and 12 are shown. As in Figure 2.2 the solid lines are the temperature increases multiplied by 1.9 $\mathrm{Wm^{-2}K^{-1}}$ and the dashed lines are the actual clear-sky OLR changes. The cartoon displayed by the three panels demonstrates how the intermediate wave number 8 (applies also to 6, not shown) matches the horizontal scale of the tropical circulation such that a change in the strength and the accompanying changes in the moisture field has the same meridional structure as the applied perturbation. At smaller and larger scales the overturning strength changes without the resulting OLR changes resembling the perturbation.

In the GEOS model (Figure 2.5(c)) the estimates look, as expected, more like the CCM3 clear-sky estimates than the all-sky estimates: The high-latitude value stays reasonably close to 2 $\mathrm{Wm^{-2}K^{-1}}$ throughout the considered range of experiments. For large scales, the low-latitude estimate alternates between positive values for even perturbations and negative values for odd ones, indicating again that shifting the Hadley cell has more impact on the OLR than changing its strength. At intermediate wave numbers (4 and 6) we again see the low-latitude estimate being close to 2 $\mathrm{Wm^{-2}K^{-1}}$. As opposed to the clear-sky CCM3 case where it was due to the perturbation having the same structure as the change in the circulation, the result is now simply a fortuitous cancellation of errors: Both structure and amplitude of the

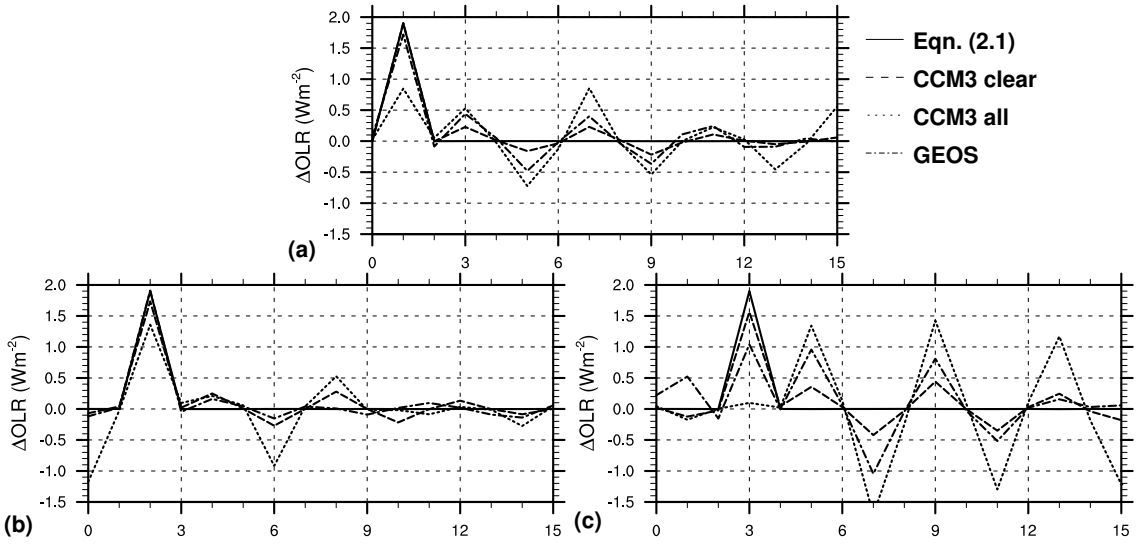

Figure 2.7: Same is in Figure 2.2 but in wave number space. (a) first order perturbation, (b) second and (c) third. The OLR changes have simply been projected onto the Legendre polynomial basis and in case of a perfect match with eqn. (2.1) they would only have power on the perturbed wave number.

OLR change are quite different from the perturbation. At higher wave-numbers there is a reversal of the behavior with even orders giving more negative estimates than odd orders, such that for smaller-scale perturbations, the strength change effect seems to dominate over the shifting effect. In neither case, however, does the low-latitude OLR change have any reasonable correspondence to the perturbation.

Results in wave number space

A different way of displaying our results is to make plots corresponding to Figure 2.2 in the basis of Legendre polynomials. Figure 2.7 shows the results of the first, second and third order perturbations. The solid lines are again the SST increases multiplied by 1.9 $\mathrm{Wm}^{-2}\mathrm{K}^{-1}$ while the dashed lines and dotted lines are the changes in OLR for the CCM3 clear-sky and all-sky cases, respectively. The dash-dotted lines are the GEOS model OLR changes. In panel (a), showing the first asymmetric perturbation, the dashed line falls quite closely on top of the solid line reflecting the good match between the calculated change and the CCM3 clear-sky OLR change in Figure 2.2(a). The dash-dotted line (GEOS) reflects how the larger error in the tropics places more power on the higher wave-numbers. The dotted line (CCM3 all-sky) shows how the cloud shielding effect reduces the power in wave number 1 and how the shifts in the low-latitude cloud field place significant amounts of power on higher wave numbers. A similar picture emerges in panel (b) (wave number 2) where the cloud shielding effect, however, works in the same direction in both hemispheres and places power on the zeroth wave number. The circulation changes associated with the large scale symmetric perturbation leads to no

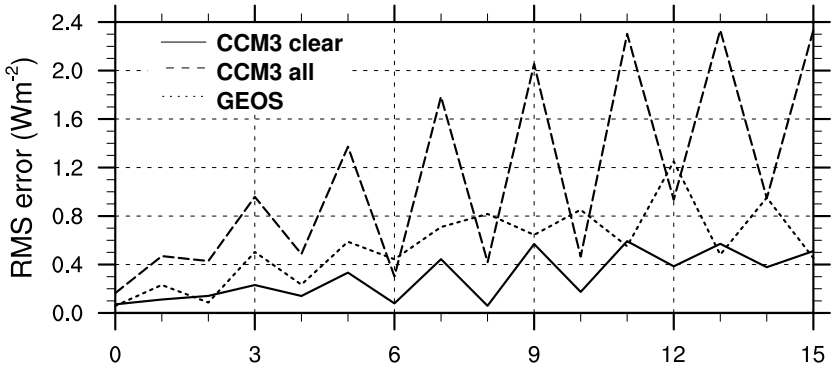

Figure 2.8: Root mean square distance between actual and expected wave number space representations of OLR change as function of perturbation order. Solid: CCM3 clear-sky, dashed: CCM3 all-sky, dotted: GEOS model. An RMS error of 0 implies a perfect match with the linear prediction.

significant error in the GEOS model and the dash-dotted line is even better than the dashed one corresponding to the CCM3 clear-sky case. In panel (c) the CCM3 all-sky OLR change is seen to have practically no resemblance with the temperature perturbation: There is no power on the perturbed wave number while it is distributed among all the higher odd-order wave numbers. The CCM3 clear-sky and GEOS curves are more well-behaved although the fits have deteriorated as compared to the two previous perturbations.

The root-mean-square (rms) distance between the solid curve and the dashed, dotted and dash-dotted curves, respectively, can be used as a measure of how well eqn. (2.1) performs at a given wave number. In Figure 2.8 we have plotted this difference for the CCM3 clear-sky (solid) and all-sky (dashed) cases and for the GEOS model (dotted) as a function of wave number. A feature common to all three cases is the deterioration of the relationship with decreasing horizontal scale. An exception to this is the good fit in the CCM3 at intermediate even wave numbers where the horizontal structure of the perturbation, as mentioned, matches the changes induced in the circulation.

It is also apparent how the symmetric perturbations in general yield better results than the asymmetric ones which, as we have seen, induce a shift in the position of the ITCZ. There are two exceptions to this: 1) In the CCM3 clear-sky case, the first asymmetric perturbation gives as good a fit as the two first symmetric ones. The changes in strength are at the largest scales as important as the shift of the circulation. As intermediate scales are approached the asymmetric shifts in the ITCZ tend to decrease the projection of the OLR change onto the perturbation giving worse fits while the symmetric perturbations tend to give even better fits. At the smallest scales the asymmetric fits no longer deteriorate but the symmetric perturbations no longer match the circulation changes and the errors become nearly as large as those for the asymmetric perturbations. 2) For the GEOS model we see that, at the smallest scales, the asymmetric perturbations tend to give smaller errors than the symmetric ones. Here the

changes in the strength of the circulation associated with the symmetric perturbations are relatively large tending to reverse the sign of the OLR change and placing most of the power on the neighboring even order wave numbers.

2.1.3 Conclusions

In two different GCMs we have performed a series of Legendre polynomial perturbations of the surface temperature and analyzed the response in the OLR. For clear-skies the OLR response follows rather closely a linear relationship as eqn. (2.1) at high latitudes. Due to large high-latitude cloudiness in the CCM3 reference climate the all-sky OLR response is damped leading to a worse agreement with eqn. (2.1) at high latitudes. At low latitudes the higher moisture content of the atmosphere becomes important as does the meridional circulation which to large extent sets the structure of the low-latitude moisture field. As discussed by e.g. Allan et al. (1999), the seasonal shifts in convective regimes lead to off-equatorial areas displaying negative correlations between SST and OLR. This is also observed in our study where the asymmetric perturbations yield a shift in the Hadley cell and associated shifts in the relative humidity field which, in turn, lead to spikes in the OLR directed in the opposite direction of the local temperature change. Associated with symmetric perturbations is another effect on the meridional circulation which is not captured by the seasonal cycle: Changes in the meridional temperature gradient lead to strengthening (or weakening) of the Hadley cell which leads to moistening (drying) in the ascending branch and drying (moistening) in the descending branch. These moisture changes were also seen to have large impact on the OLR. An interesting effect was seen in the CCM3 where symmetric perturbations of intermediate wave numbers (6 and 8) led to circulation changes of comparable meridional structures such that the OLR changes were very well represented by eqn. (2.1). Since this effect was absent in the GEOS model, it is unclear whether such a match-up would be seen in reality.

The role of cloud radiative feedbacks in climate sensitivity and stability is still much debated, especially when it comes to tropical dynamics. In terms of the OLR parameterization it has been put forth (e.g., Short et al., 1984; Graves et al., 1993) that due to the cancellation of the longwave and shortwave effects of clouds, we should be on safe ground if we ignore the clouds in the parameterizations of both fluxes. Thus, we have in the present section presented both all-sky and clear-sky results from the CCM3. A large part of the disagreement in the all-sky case is, as mentioned, due to the rather excessive cloudiness in the CCM3 reference climate. We speculate that, with a decreased reference cloudiness, the all-sky case would behave more like the clear-sky case and thus, at least at mid and high latitudes, yield better agreement with eqn. (2.1).

The CCM3 all-sky OLR is not very well represented by eqn. (2.1) while its clear-sky OLR is reasonably represented (Figure 2.8). The results for the GEOS model, which, in fact, is a clear-sky model, lie between these two. With large, symmetric perturbations the GEOS model

and the CCM3 clear-sky results are equally good but at intermediate and small scales the CCM3's clear-sky response is closer to the linear relationship.

In general, large-scale, symmetric perturbations produce OLR responses better in accordance with eqn. (2.1) than do small-scale, asymmetric perturbations. This seems to imply that the Budyko-Sellers parameterization is best suited for the simplest annually averaged EBM studies of large-scale effects and that discrepancies are more liable to occur in experiments including the seasonal cycle (asymmetries), two dimensions and continents (smaller scales). A feature common to all perturbations, however, is that they yield good clear-sky results at high latitudes where the focus of EBM studies (of for example the ice-albedo feedback) typically lies.

Had we included continents, seasons and longitudinally varying perturbations, changes in strength and position of monsoonal and other circulations would have led to problems similar to those encountered in the simplified setup. However, according to Short et al. (1984) the asymmetric part of the fields only accounts for a small part of the variance in the annual mean, and we may expect the results of our zonally symmetric experiments to account for the dominant part of annual mean quantities in climate change experiments.

Tropical circulation and dynamics are so important for even the clear-sky OLR that a local relation with SST is insufficient. One could, of course, include some representation of the moisture field but one would then be left with the task of determining that in an EBM. The solution that we will propose is to use the matrix that one gets when combining the full set of 16 plots corresponding to the three shown in Figure 2.7. The i'th plot gives the OLR response in all wave numbers arising from a temperature perturbation in the i'th wave number. In vector notation, the OLR field can thus be calculated as

$$\mathbf{F}'_{LW,TOA} = [\mathbf{B}_1|\mathbf{B}_2|\cdots|\mathbf{B}_N]\,\mathbf{T}'_S,$$

where the columns of the $\mathbf{B}$-matrix are the vectors represented by the plots in Figure 2.7. $\mathbf{F}'_{LW,TOA}$ is the OLR perturbation and $\mathbf{T}'_S$ the SST perturbation, both given in the N-dimensional basis of Legendre polynomials. A requirement for this parameterization to hold is that the OLR response is linear with respect to the different combinations of the Legendre polynomial SST perturbations. We have not yet checked this systematically but in all our preliminary runs it has, in fact, been the case. This is encouraging for the possibility of running EBMs in Legendre space (as has often been done (e.g., North, 1975a)) and in this manner including the non-local effects seen in the present section while still using a linear and inexpensive parameterization.

2.2 Multiple equilibria

Paleoclimatic proxies indicate that the climate experienced greatly different states in the past (Zachos et al., 2001; Johnsen et al., 1995; Petit et al., 1999). This diversity is usually attributed to changes in the forcing or variability of the ocean-atmosphere system on timescales ranging from years and decades (e.g., the 11-year solar cycle and El Niño) to thousands and millions of years (oceanic thermohaline circulation, Milankovitch forcing and plate tectonics). A variety of model studies have found that multiple equilibria exist both in very simple and more comprehensive models of the climate system. Among the factors responsible for multiple equilibria in the simple models are feedbacks related to changes in the oceanic overturning, ice-albedo effects and radiative-convective properties of the atmosphere (Stommel, 1961; Budyko, 1969; Sellers, 1969; Thorndike, 1992; Rennó, 1997; Ide et al., 2001). Within a more complex framework of coupled OA-GCMs or Earth Models of Intermediate Complexity, multiple equilibria are typically related to changes in the thermohaline circulation (Manabe and Stouffer, 1988; Ganopolski and Rahmstorf, 2001; Saravanan and McWilliams, 1995, and many others).

The principle mechanism leading to multiple equilibria in EBMs is the ice-albedo feedback, and in this section we study the effects of including a thermodynamic sea ice model in our configuration. As before, all asymmetries in the forcing are excluded while the full complexity of the GCM itself is retained. With the zonally symmetric configuration, the lack of seasonality and the full non-linearity of the ice-albedo feedback included, our model has a number of similarities with the EBMs. There are important differences, though: Due to the full physical treatment of atmospheric circulation and thermodynamic processes, dynamic-radiative changes such as those discussed in the previous section are included. The simplified configuration allows us to study the "fine structure" of the annual mean equilibrium climate, which in our case exhibits multiple stationary states under the same external forcing.

2.2.1 Methodology

The experimental configuration consists of the CCM3 with our aquaplanet upper mixed-layer ocean boundary condition. As in the previous section the experiments were carried out with 18 vertical levels and T21 horizontal resolution. Seasonality is excluded by employing the modified equinox solar forcing (as described in Section 1.4.2). The solar constant is set to 1367 Wm^{-2} and the CO_2 concentration is 355 ppm.

As an addition relative to the previous section we here include a simple sea ice model. Since it is purely thermodynamic, sea ice dynamics are not modeled. The sea ice is represented by four ice layers and one snow layer. Each layer is characterized by a temperature and a thickness and they are coupled by the heat equation. Sea ice forms with a minimum thickness of 0.25 m when the SST drops to $T_f = -1.9°\mathrm{C}$ and is assumed to cover the entire grid box such that less than unity ice concentrations are not modeled.

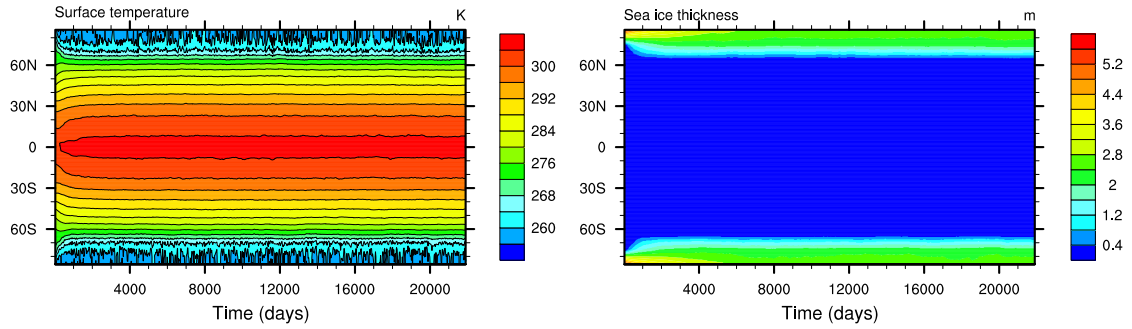

Figure 2.9: Temporal development of zonally averaged SST and sea ice thickness in a run started with a small ice cover and q-flux strength 175.

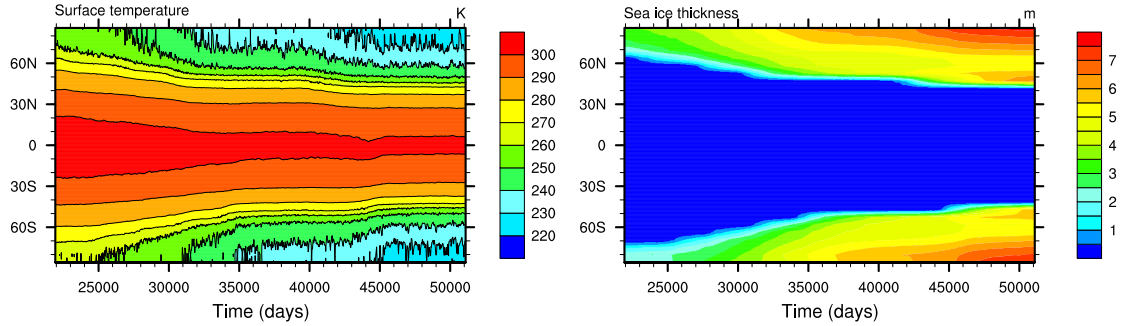

Figure 2.10: As in Figure 2.9 but with q-flux strength 160.

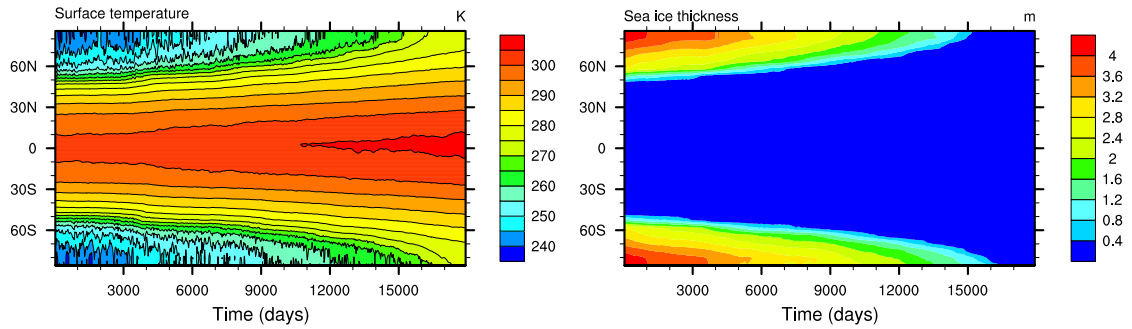

Figure 2.11: As in Figure 2.9 but started from the icy state and with q-flux strength 220.

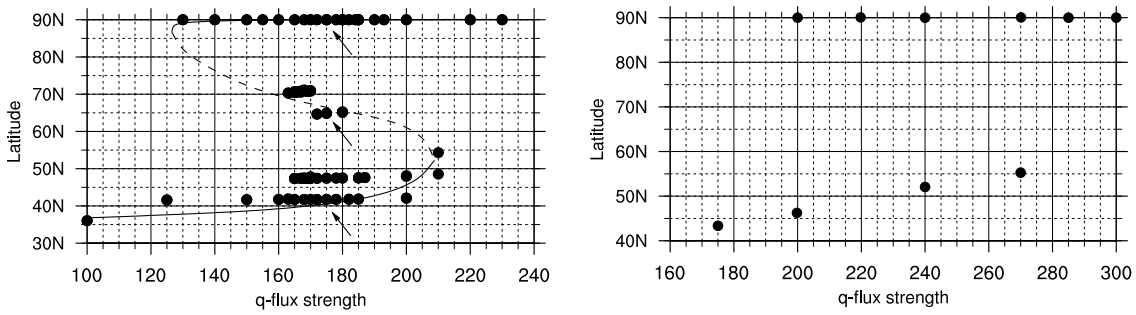

(a) (b)

Figure 2.12: (a) The position of the sea ice margin as a function of the q-flux strength. The three arrows point to the 175-equilibria discussed in the text. The curved line has been drawn by hand and illustrates a possible interpretation of the branches of the bifurcation diagram (solid is stable and dashed is maybe unstable, see text). (b) As in panel (a) but with T42 resolution.

To assess how the equilibrium climate changes when the q-flux is varied, we again used the simple smooth q-flux as shown in Section 1.4.2. The magnitude of the q-flux was varied by simply scaling the solid line in Figure 1.1(b). In the test phase of our simplified configuration we started the model with various q-fluxes (strengths between 0 and 300 in units of percent of the solid curve in Figure 1.1) with present-day-like initial conditions. We obtained icy climates for the weak fluxes and ice-free climates for the strong fluxes. Figures 2.9-2.11 show examples of this.

In Figure 2.9 we started from an initial state with sea ice poleward of about 75° and a q-flux strength of 175 (corresponding to a peak meridional oceanic heat transport of 1.75 PW). The model rapidly settles into an equilibrium with sea ice poleward of 65° in both hemispheres. Figure 2.10 shows the result of starting a run from this climate with the q-flux reduced to strength 160. The resulting equilibrium is one with a massive sea ice cover. In Figure 2.11 is shown a run starting from this cold equilibrium with the q-flux increased to strength 220. After about 40 years of integration the sea ice has completely melted away.

To determine the position and structure of the transition, we used the equilibria from these runs as initial conditions for intermediate strengths. Continuing in this way – using equilibria from previous strengths as initial conditions for new ones – we were able to produce the bifurcation diagram of Figure 2.12(a). It shows the position of the ice edge as a function of the q-flux strength. This position was calculated by averaging the sea ice thickness zonally and over as many years as possible (depending on how long the model has run and how long it has been in equilibrium), typically about 10 years. The sea ice edge is then defined as the latitude where the thickness reaches 0.25 m interpolated between the model's grid latitudes.

At strength 100, the climate equilibrates with a sea ice margin at about 35° while at

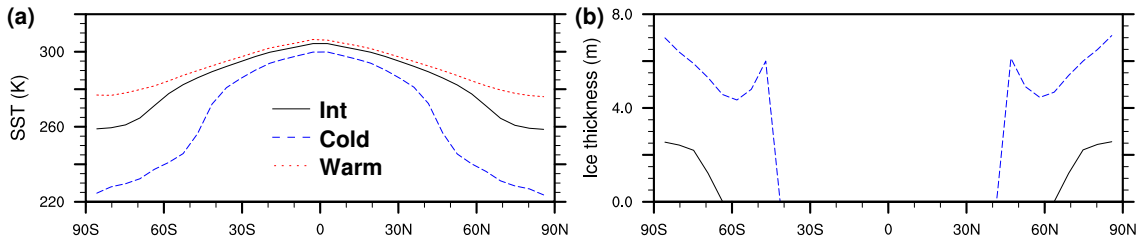

Figure 2.13: (a) Zonally averaged surface temperature and (b) sea ice thickness for intermediate (black), cold (blue) and warm (red) climates realized with q-flux strength 175.

strength 220 the planet is completely ice-free. Between these extremes a rather complicated structure of bi- and tri-modal solutions is seen. When started from completely ice-covered initial conditions the model also realizes the "snowball Earth" for the whole range of q-fluxes but this is neither depicted in the figure or dealt with here, since the large negative q-fluxes at the equator cause the ice thickness there to increase to $\mathcal{O}(100\text{m})$ – entirely inconsistent with sustaining such an oceanic heat flux convergence.

2.2.2 Three equilibria

In a range of q-flux strengths, more equilibria are possible: At strength 175, for example, four equilibria seem to exist; one with sea ice lines at 42° in both hemispheres, one at 47°, one at 65° and one ice-free (sea ice lines at 90°). These positions of the ice edge are seen to hold over an interval of q-flux strengths producing a number of horizontal lines in the figure. These lines correspond closely to the grid latitudes of the model resolution with, for example, the 42° and 47° lines being two neighboring grid latitudes. Although the ice margin has been interpolated between the grid latitudes it seems to lock itself along these latitudes reflecting a very low degree of variability of the sea ice margin both spatially and temporally once equilibrium is reached. Since they are separated by only a single grid latitude we consider the two lines at 42° and 47° to reflect the same equilibrium. This, however, does not hold for the 65°- and 90°-climates which are also seen at strength 175: We have, in total, a very cold and icy state ($\sim$ 45°, hereinafter referred to as the *cold* climate), a present-day-like state ($\sim$ 65°, *int* climate) and a warm ice-free state (90°, *warm* climate) reflecting completely different climates realized under the same external forcing. The meridional profiles of SST and sea ice thickness are illustrated in Figure 2.13 for the three equilibria.

Although the runs started in the intermediate equilibrium at 65° have stayed there for at least 100 years (the length of the runs in this state), the state may be only marginally stable or even unstable. As we shall see in the following, asymmetric states exist but not with combinations of the intermediate state. Moreover, when resolution is increased or seasonality or a continent is included, the intermediate state is not recovered. This has led us to sketch

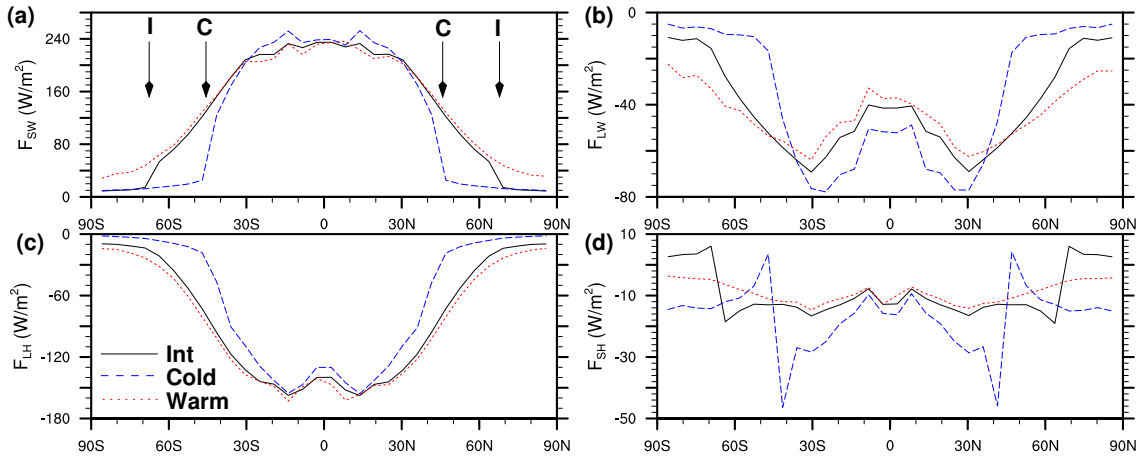

Figure 2.14: Surface budget components for the intermediate (black), cold (blue) and warm (red) climates. (a) Shortwave (SW), (b) longwave (LW), (c) latent heat (LH) and (d) sensible heat (SH). All fluxes are taken positive downwards. The arrows marked "I" and "C" in panel (a) mark the ice-line position in the intermediate and cold climates, respectively. Note the different scales on the plots.

a so-called operating curve (e.g, North, 1990) on top of Figure 2.12(a). This curve looks much like the ones obtained with EBMs and suggests that unstable states exist in the whole intermediate range (dashed curve). Possibly, the intermediate state that we do find is somehow stabilized by the rather low resolution; when the system is started in or very close to this state, the transition away from the (unstable) equilibrium is impeded by the large jump that must be made at all longitudes.

Figure 2.14 provides details about the surface budgets of the three equilibria realized at strength 175. The panels (a)-(d) show zonal and 10 yr means of the individual components: the net SW, net LW, latent heat and sensible heat, respectively. As expected from observations of present-day conditions, the latent heat loss is the dominant term balancing the SW heating. While this also holds in the cold and warm climates, the relative importance of the LW radiation increases with latitude in all cases. In the cold climate, a large decrease in the SW heating is seen in the band ($\sim 40°$ to $65°$) of sea ice advance and conversely, an increase is seen in the warm climate in the band of retreat. This is a clear signal of the sea ice albedo effect on the SW and the changes are seen to be balanced mainly by changes in the latent and LW cooling that are comparable in magnitude. In the cold climate, the modest solar heating over the broad ice-covered area is balanced to a large degree by the sensible heat loss. This flux plays only a minor role in the two warmer climates.

The changes in the SW are obviously heavily influenced by the changes in surface albedo accompanying the changes in sea ice extent. However, the cloud cover also plays a role as demonstrated in Figure 2.15 where the radiation differences between the climates are com-

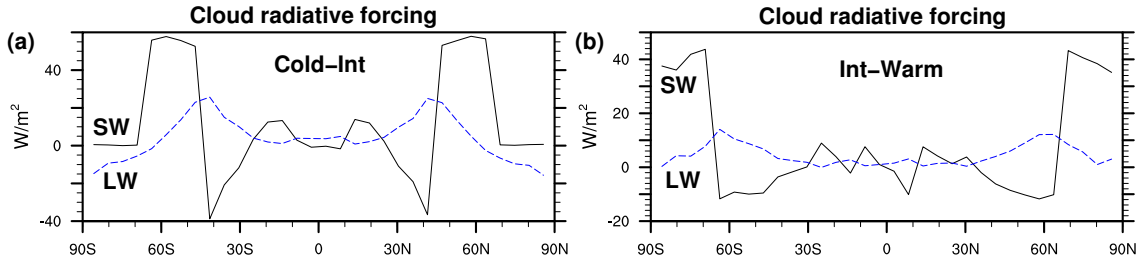

Figure 2.15: Change in cloud radiative forcing when going from int to cold (a) and warm to int (b) climates. Black line is SW and blue line is LW. Positive values over areas where ice has retreated indicate (as discussed in the text) that the actual change in SW is less than would have been the case without clouds.

pared to their clear-sky counterparts. The surface cloud radiative forcing[1] is the difference between the all-sky and clear-sky radiative fluxes (as discussed in Section 2.1)

$$\begin{aligned} \mathrm{CRF} &= (F_{SW} - F_{LW}) - (F_{SW,clr} - F_{LW,clr}) \\ &= (F_{SW} - F_{SW,clr}) - (F_{LW} - F_{LW,clr}) \\ &= \mathrm{CRF}_{SW} + \mathrm{CRF}_{LW}, \end{aligned}$$

which defines the short- and longwave CRFs (note that both are defined as positive when clouds have a warming effect). Figure 2.15 gives the changes in these quantities when going from a colder state to the next warmer state. An interpretation of the curves becomes clearer if the CRF change is rewritten as

$$\begin{aligned} \mathrm{CRF}_{SW,cold} - \mathrm{CRF}_{SW,int} &= (F_{SW} - F_{SW,clr})_{cold} - (F_{SW} - F_{SW,clr})_{int} \\ &= (F_{SW,cold} - F_{SW,int}) - (F_{SW,cold} - F_{SW,int})_{clr}, \end{aligned}$$

such that we are comparing the actual change to what it would have been in the absence of clouds. In panel (a), the positive values of the solid line in the ice-advance band demonstrate how the decrease in SW in the cold climate compared to the intermediate climate is much smaller than it would have been without clouds. Likewise, the increase in the SW when going to the warm climate is also smaller than it would have been without clouds. It turns out, that it is the *existence* of clouds that shields the ice-albedo feedback and dampens its impact and that the *change* in clouds (not shown) plays a smaller role. The figure does not show anything about the sign of the cloud feedback; it only demonstrates that the clouds always dampen the effect of surface albedo change. The figure also demonstrates that the effects of clouds play a much larger role for SW budget changes than for LW budget changes when such large differences in ice cover are involved.

[1] See a further treatment of the cloud radiative forcing (CRF) concept in Chapter 4.

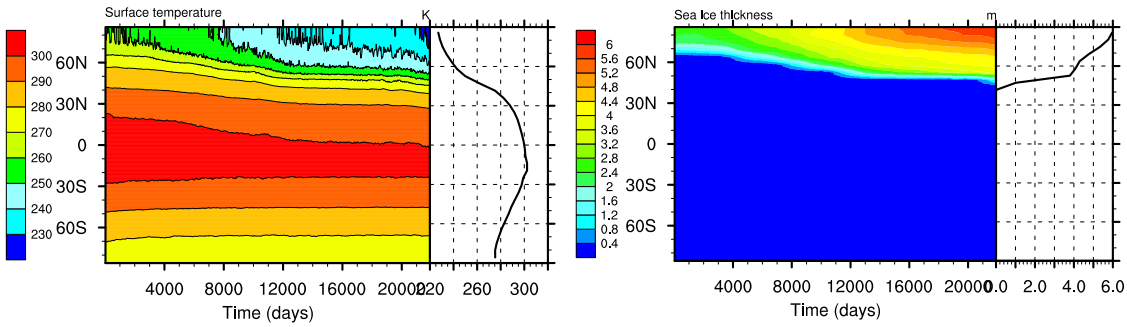

Figure 2.16: As in Figure 2.9 but started from intermediate and warm state in the two hemispheres, respectively. The q-flux strength is again 175. The attached line-plots show the time-average over the last part of the integration.

The equilibria discussed this far have all had a symmetric sea ice cover between the hemispheres. This is, however, not necessary for the climate to be in equilibrium: At a wide range of strengths (at least 140-200) runs started with initial asymmetries, such that one hemisphere resembles the warm climate and the other the cold climate (warm/cold), stay there indicating that this is a stable solution. At strength 175 we also started warm/int and int/cold runs but they jumped to the warm/cold and cold/cold states, respectively. This is demonstrated in Figure 2.16 showing the run started from the warm/int initial state. The fact that the intermediate climate is absent from the asymmetric combinations, and the rather narrow range in which the int climate is possible in Figure 2.12(a), suggests, as discussed, that the int climate is unstable.

2.2.3 Effects of resolution, annual cycle and continents

Since the multiple equilibrium feature has not been encountered when both continents and seasons are included we have repeated the above experiment without some of our simplifying changes. We have thus tested the robustness of the result to resolution, seasonality and continentality.

Figure 2.12(b) displays the bifurcation diagram obtained when the horizontal resolution is changed to T42 while the aquaplanet and modified equinox conditions are retained. The multiple equilibria still stand out as a very robust feature; between q-flux strength 200 and 270, the cold and warm equilibria encountered before still exist. The intermediate climate has not been encountered, but this does, however, not necessarily imply that it does not exist for some small q-flux interval. Due to the higher computational cost of running at T42 resolution we have, as is evident from the figure, not performed as detailed a search of the phase space. Most likely, what we speculated may have been an unstable branch of the operating curve (Figure 2.12(a)) does not have points that are "artificially stabilized" by the resolution in the T42 case.

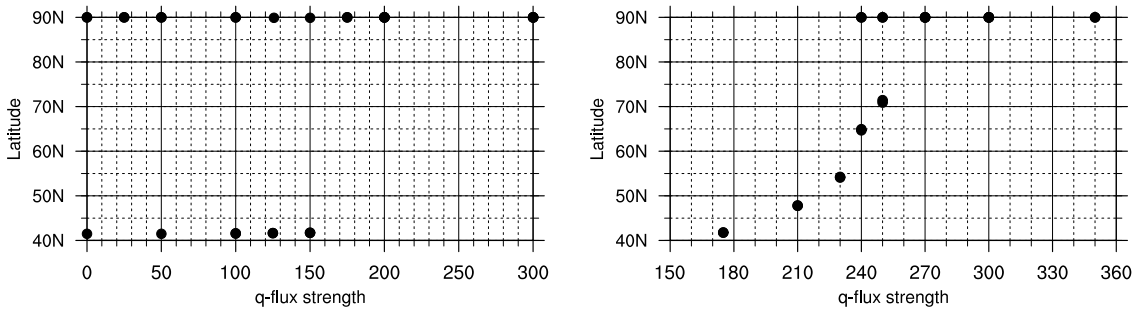

(a) (b)

Figure 2.17: As in Figure 2.12 but with (a) seasons and (b) a simple continent included. Note how inclusion of the continent yields a more gradual retreat of the ice-line with increasing q-flux, and that the multiple equilibria now only exist in a very narrow range.

More generally, the multiple equilibrium feature seems not specific to the rather coarse resolution employed but rather to the simplified boundary conditions. It is interesting to note how the finer resolution allows the sea ice line to crawl polewards more gradually when the poleward oceanic energy transport increases. At the coarser resolution a shift in the sea ice line required larger changes in the transport than is the case at T42 resolution.

In Figure 2.17(a) we show the result of including a present-day-like annual cycle[2] while keeping the aquaplanet and T21 resolution. The cold and warm equilibria co-exist over a wide range of q-fluxes, but as in the T42 case we do not see the intermediate climate. In the warm climate, the thermal inertia of the 50 m mixed-layer allows the ice-free state to survive through the winter, and in the cold climate, the thick sea ice cover allows it to survive the summer. The zonal symmetry also plays a large role: should one grid point in the warm (cold) climate become ice-covered (ice-free), then the zonal circulation will advect warm (cold) air over it and reverse the tendency.

This zonal symmetry is broken when a continent is included. We have inserted a continent stretching from pole to pole and from longitude 0 to 60°E (see Figure 2.18). The resulting bifurcation diagram (Figure 2.17(b)) shows how the broken zonal symmetry reduces the robustness of the multiple equilibrium feature. In a narrow region (strength 240–250[3]) we have a present day-like climate and an (almost) ice-free state. The present day-like climate appears not to correspond to the intermediate climate, but is rather a continuation of the cold climate. The zonal asymmetry has allowed for standing waves and thus for sea ice advance (or retreat)

[2]In fact, the seasonal cycle is not completely as for present day. The obliquity is set to 23.4°, but we have set the eccentricity to zero to ensure symmetry between the hemispheres.

[3]Strength 240 with only 5/6 of the world covered by ocean corresponds to a strength of 200 in the aquaplanet case.

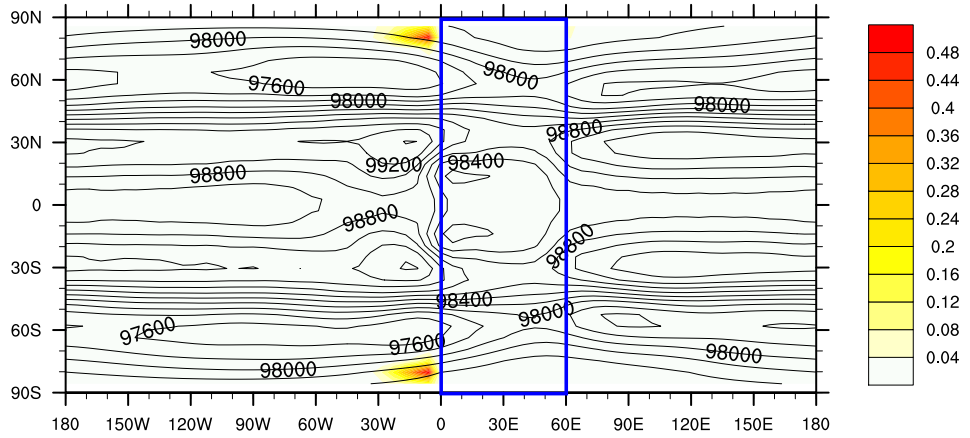

Figure 2.18: A 300 month average of sea level pressure (black contours, hPa) and sea ice thickness (color fill, m) in the warm equilibrium at q-flux strength 240 in the simple continent experiment. The blue rectangle shows the outline of the continent. Advection of cold air produces a thin ice cover off the western coast of the continent.

in only parts of a latitude band at a time. This has lead to the gradual poleward migration of the cold climate sea ice line with increasing oceanic heat transport.

Figure 2.18 shows the warm climate solution at q-flux strength 240. The black contours show the time-average sea level pressure while the colored contours show the very slight sea ice cover. It is evident from the figure how the land/ocean contrast in orographic and thermodynamic (no poleward heat transport under land surface) forcing has set up a standing wave pattern. This pattern supports an advection of cold continental air off the western shores and thus leads to occasional sea ice cover in this area. Such a stationary ice cover is disqualified in the aquaplanet setup due to the previously mentioned zonal advection of warm air tending to melt it away. This slight ice cover is the reason for the small overlap between the two climatic regimes, since it can serve as the seed for a larger ice cover when the oceanic heat transport is reduced. Without the continent, this seed is absent and much larger reductions in heat transport are required for a destabilization of the warm climate. The very narrow overlap between the states makes this configuration quite interesting in a hysteresis context, since only small changes back and forth in the strength of the oceanic heat transport will force the system to jump between the states.

2.2.4 Conclusions

To study the "fine structure" of the annual mean climate we have coupled an AGCM to an upper mixed layer ocean. We have removed seasonality, continentality and all zonal and hemispheric asymmetries in the forcing of the model. A smooth q-flux was inserted at the bottom of the mixed layer to crudely represent the oceanic heat flux convergence. The amplitude of

this flux was varied and the resulting equilibria were studied.

The snowball Earth, the ice-free planet and a very icy climate (sea ice margin at $\sim 45°$) are possible over a wide range of q-flux strengths and in a more narrow region another seemingly stable solution (with present-day-like ice coverage) exists. Asymmetric solutions consisting of a warm and a cold hemisphere also emerge. Whenever one encounters such multi-modal solutions it is tempting to identify them with the multi-modality in paleoclimatic proxies, but in the current case great caution should be observed since these results probably are specific to the simplified model configuration. However, since the combination of an AGCM with an upper mixed layer ocean and a flux-correction is so widely used it is important to be aware this type of behavior.

The solution space arrived at in this section resembles quite well that seen in the classic Budyko-Sellers type energy balance models (EBMs). Analyzing this type of models Chýlek and Coakley (1975) and North (1975a) found not only the snowball Earth and the present-day-like climate but also the ice-free climate (for some values of the solar insolation in North's Figure 1) and the low-latitude ice climate. North demonstrates, however, that the latter climate is an unstable solution. This is certainly not the case in our model and either the climates we find are not identical to North's or they are stabilized by feedbacks due to the added physics in our model compared to the EBMs. In their AGCM/mixed layer model Hyde et al. (2000) also find a solution with sea ice extending to very low latitudes (25°). They argue that this state is stabilized relative to the EBM case by a decrease in low-latitude cloud cover yielding sufficient decreases in albedo to keep the tropics ice-free. The same may be the case in our model where a decrease in the amount of especially low clouds is seen at low latitudes and is reflected in increases in the SW (dashed line in Figure 2.14(a) and solid line in Figure 2.15(a)).

The lack of a smooth transition from the icy states to the ice-free state is reminiscent of the small ice cap instability (SICI) phenomenon discussed by North (1984), Lee and North (1995) and others. Lee and North conclude, by comparing AGCM and EBM experiments, that noise of certain amplitudes and spectral characteristics is needed to eliminate SICI. Possibly the longer timescales associated with our aquaplanet (as opposed to their *all-land planet*) weakens the amplitude (and changes the spectral slope) of the surface temperature fluctuations such as to maintain the instability.

Our results are unlike any other obtained with the CCM coupled to a slab ocean (e.g., Shellito et al., 2003). We believe it to be the first report of multiple equilibria in an AGCM explicitly resolving the dynamics and physics while coupled to a slab ocean with sea ice. It thus begins to close the gap between AGCM results and those of more simple models. When we increased the resolution, we lost the intermediate state and one could ask if we would loose further states if resolution is increased again. We believe, however, that the warm and cold states are such robust features across our different configurations that they are not merely an effect of resolution (as the intermediate climate seems to be). Our experiments with changed configurations suggest that the multiple equilibria arise because we have omitted the

continentality; the increased variability and especially the broken zonal symmetry associated therewith tends to destabilize certain solutions. The multiple equilibria rely heavily on the sharp non-linearity associated with the abrupt change in albedo between the icy and ice-free latitudes. In fact, North (1990) writes that "One has to question the sharpness of the discontinuity in the real world where, after all, what we mean is that zonal and annual averages are to be taken". We have found that when our configuration is zonally symmetric, zonal and annual averages still provide the necessary discontinuity to support the rich solution structure.

Chapter 3

Polar amplification and atmospheric energy transports

As discussed in Section 1.2, polar amplification has been seen in GCMs where sea ice effects have been eliminated. The mechanisms behind this are the focus of this chapter and we therefore employ the ice-free configuration of the model. Possible catastrophic transitions associated with the multiple equilibria encountered in the previous chapter are thus avoided.

We also discussed how polar amplification might be exploited to use observations of the current Arctic to identify early signs of global warming. A caveat to this approach is that, when studying the time rate-of-change during the transient of a response (as the Earth may by undergoing now), it may not be possible to identify the polar amplification (Polyakov et al., 2002). In areas of deep convection, for example, the enormous heat capacity of the deep ocean can keep the surface temperatures far from the final equilibrium pattern (Manabe et al., 1991). Here, the global warming is studied as a stationary response to a forcing, and the term *polar amplification* will designate the pattern of greater warming at high latitudes compared to the rest of the globe in this stationary sense.

Before proceeding to the actual study of polar amplification, we will in Section 3.1 look closer at the linear dynamics of our simplified model. In Section 3.2 the mechanisms behind the polar amplification are studied in detail, while Section 3.3 looks closer at the dependence of poleward heat transport on surface temperatures.

3.1 Linear analysis of the zonal mean dynamics

This section presents two different ways of extracting an operator that describes the linear dynamics of the zonal average SST field in our model. It is based in part on the work presented in Langen and Alexeev (2005a). We employ the aquaplanet and modified equinox configuration with a 50 m mixed-layer and T21 horizontal resolution.

Firstly, we will describe the idea behind the method and introduce the notation used

throughout the section. This subsection follows rather closely the derivations of Alexeev (2003). Next, the two different methods for extracting the operator will be described and the accuracy of the methods will be assessed through a comparison with a simple climate warming experiment.

3.1.1 Climate and linear algebra

With our 50 m mixed-layer depth the typical time-scale for atmospheric response is significantly shorter than that for the ocean, and the atmospheric time-scale can be regarded as an instant in terms of the longer oceanic time-scales. Since the atmosphere is chiefly heated from below, the atmospheric state averaged over the short atmospheric time-scales will be given by the state of the ocean. Even in a situation where the ocean is not in equilibrium with its surface fluxes (for example, because its approach to equilibrium is slow), the atmosphere will spin up to match this state such that (on the short time average) the fluxes in and out of the bottom and top of the atmosphere balance. The atmosphere can thus be regarded as being in quasi-equilibrium with the SSTs and we will assume that to a given state of the SST field corresponds a given mean state of the atmosphere and a given set of surface fluxes. The time evolution of the SSTs, $\mathbf{x}_S$, can thus be determined as a function of the SSTs as

$$\rho_w c_w H \frac{\partial \mathbf{x}_S}{\partial t} = \mathbf{b}_{Srf}(\mathbf{x}_S, \mathbf{\Lambda}), \tag{3.1}$$

where ρ_w and c_w are the density and heat capacity of seawater, respectively, and H is the mixed-layer depth. While $\mathbf{b}_{Srf}$ denotes the surface heat fluxes, $\mathbf{\Lambda}$ is a collection of parameters, such as the CO_2 concentration and the solar constant, external to the system, in the sense that they are not influenced by the state of the system. The quantities $\mathbf{x}_S$ and $\mathbf{b}_{Srf}$ should be thought of as averages over the short time-scales (say, 50–100 days) that allow us to regard the atmosphere as being determined by the state of the SSTs. $\mathbf{b}_{Srf}$ will thus depend only on the SSTs and the external parameters. The SST field consists, in principle, of all the points on the ocean surface (2 dimensions), but due to the zonally symmetric setup we will in the following use $\mathbf{x}_S$ and $\mathbf{b}_{Srf}$ as zonal averages of the corresponding 2D fields.

The dynamical system described by eqn. (3.1) is stable. With sea ice effects excluded, the system evolves from any initial state towards the equilibrium shown in Figure 2.1(a) (open circles). After an initial transient the system eventually fluctuates around this state. Letting $\langle\cdot\rangle$ denote a time-average on the long oceanic time-scale and performing this operation on eqn. (3.1), we get

$$\rho_w c_w H \frac{\partial \langle \mathbf{x}_S \rangle}{\partial t} = \langle \mathbf{b}_{Srf}(\mathbf{x}_S, \mathbf{\Lambda}) \rangle = \mathbf{0}, \tag{3.2}$$

since the system otherwise would drift away from the equilibrium. In general, $\langle \mathbf{b}_{Srf}(\mathbf{x}_S, \mathbf{\Lambda}) \rangle$ does not necessarily equal $\mathbf{b}_{Srf}(\langle \mathbf{x}_S \rangle, \mathbf{\Lambda})$, but the fluctuations are small and an approximate

equality holds (to within 0.1 Wm^{-2}). Considering a perturbation, $\mathbf{x}'_S = \mathbf{x}_S - \langle \mathbf{x}_S \rangle$, away from the equilibrium, eqn. (3.1) linearizes to

$$\rho_w c_w H \frac{\partial \mathbf{x}'_S}{\partial t} = \mathbf{b}_{Srf}(\langle \mathbf{x}_S \rangle + \mathbf{x}'_S, \mathbf{\Lambda}) \simeq \boldsymbol{\mathcal{R}}(\langle \mathbf{x}_S \rangle)\mathbf{x}'_S, \tag{3.3}$$

where $\boldsymbol{\mathcal{R}}$ is the Jacobian of the surface budget with respect to the SSTs evaluated in the equilibrium:

$$\boldsymbol{\mathcal{R}}(\langle \mathbf{x}_S \rangle) = \left. \frac{D\mathbf{b}_{Srf}(\mathbf{x}_S, \mathbf{\Lambda})}{D\mathbf{x}_S} \right|_{\mathbf{x}_S = \langle \mathbf{x}_S \rangle}. \tag{3.4}$$

The linear stability of the system can now be characterized through the eigenspectrum of $\boldsymbol{\mathcal{R}}$. If the matrix $(\rho_w c_w H)^{-1}\boldsymbol{\mathcal{R}}$ has a complete set of eigenvectors, the time evolution of the perturbation is given by

$$\mathbf{x}'_S(t) = c_1 \mathbf{v}_1 e^{\lambda_1 t} + \ldots + c_N \mathbf{v}_N e^{\lambda_N t}, \tag{3.5}$$

where the λ's are the eigenvalues and the c's give the initial perturbation in the basis of the eigenvectors. If the real parts of all the eigenvalues are negative, all the terms in the expansion will decay exponentially (with an e-folding time of $-1/Re\lambda$).

Apart from providing us with information about the system's *stability* to internal perturbations, $\boldsymbol{\mathcal{R}}$ can also be used to determine the system's *sensitivity* to changes in the external factors; for example, how much will the SSTs change as a consequence of a doubling of the atmospheric CO_2 concentration? Let us assume that it is changed to $\Lambda + \delta\Lambda$ (dropping vector notation for Λ, the other components of $\mathbf{\Lambda}$ are implicitly held fixed). Eqn. (3.1) now becomes

$$\rho_w c_w H \frac{\partial \mathbf{x}_S}{\partial t} = \mathbf{b}_{Srf}(\mathbf{x}_S, \Lambda + \delta\Lambda), \tag{3.6}$$

and after a while the system will settle into a new equilibrium, $\mathbf{x}^*_S$, in which

$$\begin{aligned} \mathbf{0} = \rho_w c_w H \frac{\partial \langle \mathbf{x}^*_S \rangle}{\partial t} &= \langle \mathbf{b}_{Srf}(\mathbf{x}^*_S, \Lambda + \delta\Lambda) \rangle \\ &= \langle \mathbf{b}_{Srf}(\langle \mathbf{x}_S \rangle + \Delta\mathbf{x}_S, \Lambda + \delta\Lambda) \rangle. \end{aligned} \tag{3.7}$$

The new surface budget can also be expanded to first order:

$$\langle \mathbf{b}_{Srf}(\langle \mathbf{x}_S \rangle + \Delta\mathbf{x}_S, \Lambda + \delta\Lambda) \rangle \simeq \langle \mathbf{b}_{Srf}(\langle \mathbf{x}_S \rangle, \Lambda) \rangle + \boldsymbol{\mathcal{R}}\Delta\mathbf{x}_S + \frac{\partial \mathbf{b}_{Srf}}{\partial \Lambda}\delta\Lambda, \tag{3.8}$$

where $\Delta\mathbf{x}_S = \mathbf{x}^*_S - \langle \mathbf{x}_S \rangle$ is the temperature change and we define

$$\delta\mathbf{b}_{Srf} = \frac{\partial \mathbf{b}_{Srf}}{\partial \Lambda}\delta\Lambda \tag{3.9}$$

as the change in the surface budget resulting from the change in the CO_2. If we can determine $\boldsymbol{\mathcal{R}}$ and $\delta\mathbf{b}_{Srf}$, we can thus calculate the temperature change as

$$\Delta\mathbf{x}_S = -\boldsymbol{\mathcal{R}}^{-1}\delta\mathbf{b}_{Srf}, \tag{3.10}$$

since both sides of eqn. (3.8) vanish.

Now assume that we are in the ideal case where the $N\times N$-matrix $\boldsymbol{\mathcal{R}}$ is known and that it has a complete set of orthonormal eigenvectors, $\{\boldsymbol{\phi}_i, i = 1,\dots,N\}$, and that the eigenvalues, $\{\lambda_i, i = 1,\dots,N\}$, are real and negative. The forcing can then be expanded in the basis of the eigenvectors:

$$\delta\mathbf{b}_{Srf} = \sum_i b_i\boldsymbol{\phi}_i, \quad b_i = (\delta\mathbf{b}_{Srf}, \boldsymbol{\phi}_i),$$

where $(,)$ denotes the scalar product. Eqn. (3.10) now re-writes to

$$\Delta\mathbf{x}_S = \sum_i \frac{b_i}{\lambda_i}\boldsymbol{\phi}_i. \tag{3.11}$$

Assume further that there exists an eigenvalue, λ_k, whose absolute value is significantly smaller than the other eigenvalues, such that the e-folding time, $-1/\lambda_k$, is significantly longer. The eigenvector corresponding to this eigenvalue will be termed *the least stable mode*; all eigendirections are stable but for a decaying perturbation, the trajectory towards equilibrium will be along this vector after the contributions from the other modes have decayed. If such an eigenvalue exists and all the b's are of the same magnitude, eqn. (3.11) can be approximated by

$$\Delta\mathbf{x}_S \simeq \frac{b_k}{\lambda_k}\boldsymbol{\phi}_k. \tag{3.12}$$

Calculating $\Delta\mathbf{x}_S$ from this approximation is unlikely to be easier than just using eqn. (3.10), but it shows that the shape of the final temperature change is dominated by the shape of the least stable mode. The long sequence of conditions on $\boldsymbol{\mathcal{R}}$ leading to this conclusion is naturally not always met, but it nevertheless turns out that the least stable mode often gives an indication of the shape of the temperature change. These calculations and the significance of least stable mode are treated thoroughly by Alexeev (2003).

3.1.2 Evaluation of the Jacobian

We have seen how the Jacobian of the surface budget with respect to the surface temperatures plays a central role for both the stability to internal perturbations and the sensitivity to external forcing. In this section we will describe two different methods of evaluating it. We will refer to the schematic cartoon in Figure 3.1 illustrating the methods and experiments by

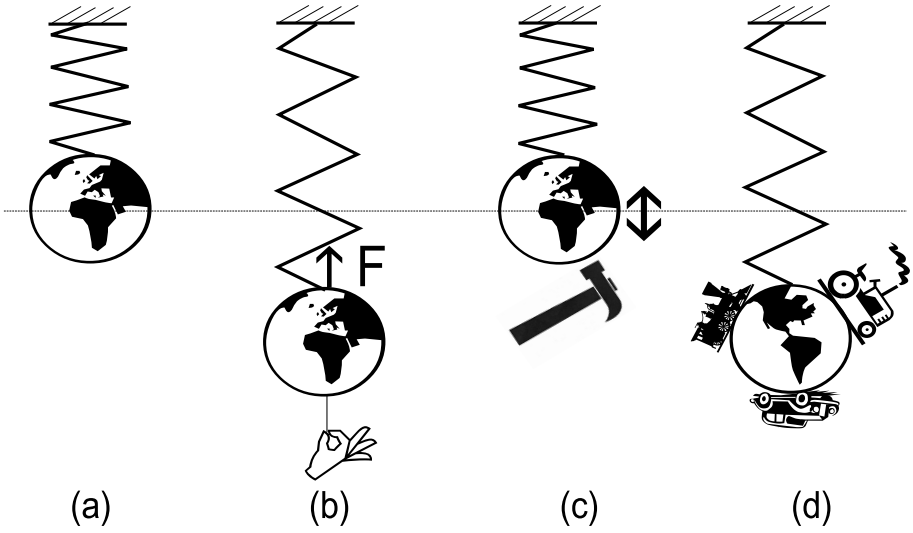

Figure 3.1: Cartoon illustrating symbolically the experiments we perform. (a) The equilibrium state. (b) The perturbation method. (c) The FDT method. (d) External climate forcing. Further explanations are found in the text.

representing the climate system with a mass hanging from a spring. In panel (a) the system is at rest, in equilibrium with the "high-dimensional" spring.

The perturbation method

The method described in this subsection is the one used and described by Alexeev (2003, hereinafter A03). The idea is quite simple: perturb the SSTs, fix the system in the perturbed state and record the response of the surface budget. Figure 3.1(b) illustrates how we pull the system away from its equilibrium (panel a) and measure the restoring force. The challenge is to determine which perturbations and how many to use. At the T21 horizontal resolution used in this study we have 32 grid points from pole to pole and the Jacobian is in principle a 32×32-matrix and the task could seem somewhat insurmountable. However, we choose here to work in terms of the zonally symmetric spherical harmonics and simply re-use the runs performed in Section 2.1 where we scrutinized the Budyko-Sellers OLR parameterization. In fact, the analysis is much like the one used there, but rather than the response in OLR we simply project the response in the surface budget,

$$\delta b_{Srf} = \delta(F_{\mathrm{SW}} - F_{\mathrm{LW}} - F_{\mathrm{SH}} - F_{\mathrm{LH}}),$$

onto the basis vectors and thereby evaluate the Jacobian. The four terms are, as usual, the net downwelling shortwave, net upwelling longwave, sensible and latent heat fluxes at the surface, respectively.

Exploiting the zonal and inter-hemispheric symmetry of the problem we use the 7 lowest

order symmetric (even) Legendre polynomials (see Appendix C),

$$\{P_0, P_2, P_4, \ldots, P_{12}\},$$

as our basis and the Jacobian thus becomes a 7×7-matrix. We have thus chosen a 7-dimensional subspace in the 32-dimensional phase space in which we expect the bulk of the system's dynamics to be included. We perturb the SST along the 7 basis vectors in turn, measure the restoring tendency and represent it in terms of the low-order basis. This method will in the following be termed the *perturbation method.*

The FDT method

This method of evaluating the Jacobian is based on a version of the fluctuation-dissipation theorem (FDT). The FDT relates a dynamical system's sensitivity to external perturbations to the fluctuation statistics of the undisturbed system. It essentially states that the dissipation of fluctuations is the same whether the fluctuation is natural or arises due to an external perturbation. While its earliest application in a climate context must be ascribed to Leith (1975), the idea goes back a century to Einstein's considerations of Brownian motion. For example, North et al. (1993) write:

> Perhaps the earliest application was in a study of Brownian motion by Einstein (1905). Later, the idea was applied to the study of voltage fluctuations across a resistor (Nyquist, 1928) and then for systems governed by a Langevin equation (Callen and Green, 1952). The extension to fully nonlinear systems in thermal equilibrium was developed by Kraichnan (1959).

Leith (1975) gives a proof of the FDT under the conditions that the dynamical system, $\dot{\mathbf{x}} = \mathbf{Q}(\mathbf{x})$, satisfies the Liouville relation and has a Gaussian equilibrium probability distribution. Consider (in tensor notation), a situation where we add an infinitesimal forcing, $\delta f_i(t)$ to the system leading to a perturbed evolution equation,

$$\dot{x}_i'(t) = Q_i(\mathbf{x}'(t)) + \delta f_i(t). \tag{3.13}$$

We introduce the the impulse-response tensor, $\hat{g}_{ij}(t, t')$, which gives the response in x_i at time t to a forcing f_j at an earlier time t'. The time evolution of the perturbation is thus calculated as

$$\delta x_i(t) = x_i'(t) - x_i(t) = \sum_j \int_{-\infty}^{t} \hat{g}_{ij}(t, t')\delta f_j(t')dt'. \tag{3.14}$$

If we return to matrix notation, the FDT states that the mean response matrix, $\mathbf{g}(t-t') = \langle \hat{\mathbf{g}}(t,t') \rangle$, of the system is given by

$$\mathbf{g}(\tau) = \mathbf{U}(\tau)[\mathbf{U}(0)]^{-1}, \tag{3.15}$$

where $\mathbf{U}(\tau)$ is the lag-τ auto-covariance matrix. In other words, the response matrix equals, on average, the linear regression prediction matrix. If a constant external forcing, $\delta\mathbf{f}$, is switched on at time $t = 0$, then the infinite-time response equals

$$\Delta\mathbf{x} = \mathbf{A}\delta\mathbf{f}, \quad \text{where} \quad \mathbf{A} = \int_0^\infty \mathbf{g}(t)dt, \tag{3.16}$$

and the FDT may thus be used to calculate the response to an external forcing from the fluctuation statistics of the unforced system.

Leith's (1975) proof of the FDT only holds for Gaussian statistics (which is not satisfied for the climate system (Leith, 1978)), but the theory has been generalized by von Storch (2004) to hold for those variables of the (generally non-Gaussian) system that have normal marginal distributions. There have been some fruitful applications of the theorem both to turbulence models (Bell, 1980) and general circulation models (North et al., 1993; Cionni et al., 2004). North et al. (1993) analyzed the sensitivity of global mean temperature in several versions of an all-land configuration of the NCAR CCM0. They concluded that the integral of the lagged auto-covariance function compared reasonably with the actual development of the system after a step-function forcing. This lends some support to the validity of the FDT in their model. Cionni et al. (2004) used the Whole Atmosphere-CCM in a specified surface temperature configuration and perturbed both the atmospheric CO_2 content and the solar constant. With step function increases in the CO_2 content they confirmed the reasonable validity of the FDT for the global mean temperature of three layers separately: at the surface, at 500 hPa and at 13 hPa. With CO_2 (solar constant) perturbations, the results improved when the covariance between the temperature and the top-of-atmosphere longwave (shortwave) flux was considered.

In both of these studies, global averages were considered and this may, as North et al. (1993) point out, reduce the validity of the analysis since interactions with higher-order modes are neglected. The evolution of the global mean temperature may, for example, be influenced by the equator-to-pole gradient. Here we consider the dynamics in the basis of the 7 lowest order symmetric Legendre polynomials and thus include the interactions with higher-order modes.

We wish to estimate $\Delta\mathbf{x}_S$ and $\boldsymbol{\mathcal{R}}$ using the FDT and to this end we consider a discrete-time version of equation (3.1),

$$\mathbf{x}_{t+\tau} - \mathbf{x}_t = \mathbf{B}_\tau(\mathbf{x}_t, \Lambda), \tag{3.17}$$

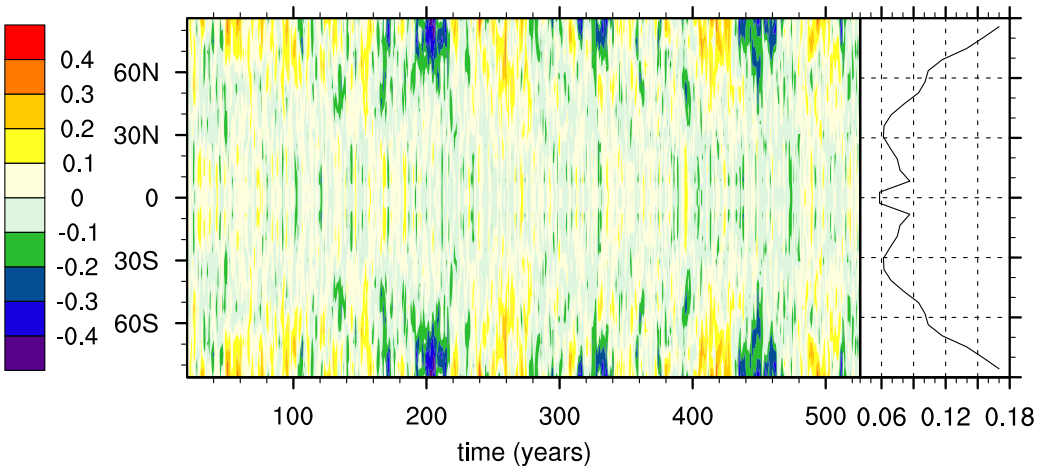

Figure 3.2: Time evolution of the inter-hemispherically symmetric component of the zonal average SST anomalies calculated as deviations from the equilibrium mean-state shown in Figure 2.1(a)(open circles). Attached is the standard deviation over the 500 year integration. Units in both panels are K.

where, in general, $\mathbf{B}_\tau$ is a non-linear function. If we change Λ, we add the forcing $(\tau\delta\mathbf{b}_{Srf})/(\rho_w c_w H)$ to the right hand side. We can evaluate the linear regression prediction matrix with a chosen lag-τ, $\mathbf{S}_\tau = \mathbf{U}(\tau)[\mathbf{U}(0)]^{-1}$, from a long unforced model run, and invoke the FDT to set $\mathbf{g}(\tau) = \mathbf{S}_\tau$. Approximating $\mathbf{S}_{n\tau}$ with $\mathbf{S}_\tau^n$ in our discrete-time formulation, the integral in equation (3.16) is given by the sum

$$\mathbf{A} = \mathbf{I}\tau + \mathbf{S}_\tau\tau + \mathbf{S}_\tau^2\tau + \mathbf{S}_\tau^3\tau + \cdots \tag{3.18}$$

This geometric series equals $\tau(\mathbf{I} - \mathbf{S}_\tau)^{-1}$, and equation (3.16) gives us the climate response due to the change in Λ (e.g., CO_2-doubling)

$$\Delta\mathbf{x}_S = \frac{\tau}{\rho_w c_w H}(\mathbf{I} - \mathbf{S}_\tau)^{-1}\delta\mathbf{b}_{Srf}. \tag{3.19}$$

We thus relate the prediction matrix to the Jacobian as

$$\boldsymbol{\mathcal{R}} = \frac{\rho_w c_w H}{\tau}\left(\mathbf{S}_\tau - \mathbf{I}\right). \tag{3.20}$$

Figure 3.1(c) symbolizes how we examine the system without pulling it away from equilibrium or perturbing it. The hammer represents the small blows with which the weather hits the system. The fluctuations that arise as a result of these blows are observed and their statistics are used to derive information about the linear characteristics of the system. We are, however, not the ones holding the hammer: the system's internal dynamics are responsible for the fluctuations.

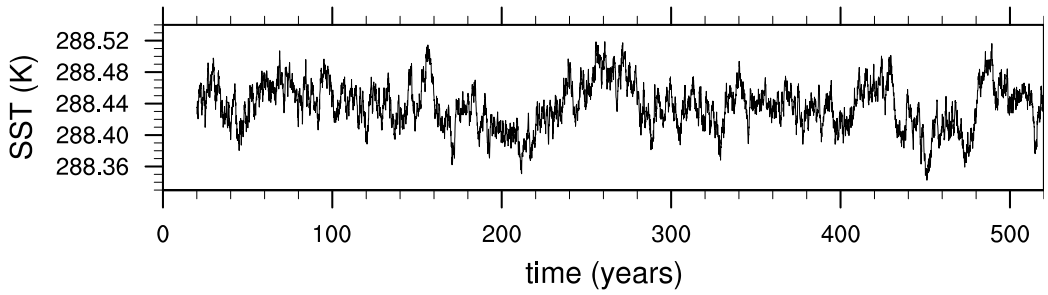

Figure 3.3: Time series of the global average temperature with standard deviation 0.03 K.

We can thus use this method to determine the Jacobian of the system exclusively by observing its internal variability – we need only collect enough data to determine the auto-covariance statistics with adequate precision. We ran the model in the usual 50 m mixed layer, aquaplanet, no-seasons and no-sea ice setup without forcing or perturbing it for 520 model years. Figure 3.2 shows the time evolution of the inter-hemispherically symmetric component of the zonal average SST anomalies. Typical anomalies are of the order of tenths of Kelvins with the largest fluctuations at high latitudes, which is also seen in the attached plot of the standard deviation. The time series of the global average SST is shown in Figure 3.3 and has a standard deviation of 0.03 K. This number is smaller than the typical fluctuations seen in Figure 3.2, which are the fluctuations used in the analysis, but the small number is interesting when compared to the global average temperature changes seen in the climate change experiments in subsection 3.1.3.

The first 20 years of our integration were excluded from the analysis as spin-up and years 20 through 520 were used to determine the auto-covariance matrices. Again, we chose to work in the basis of the 7 lowest order zonally symmetric even spherical harmonics such that the covariance matrices, the **S**-matrix and the Jacobian became 7×7-matrices. This method will in the following be termed the *FDT-method*.

The least stable mode

Figure 3.4(a) shows the least stable mode of the Jacobian as calculated using the two methods: the perturbation method (open circles) and the FDT-method (closed circles). The two vectors are remarkably similar, considering the widely different methods used to evaluate them. They are both rather constant at low latitudes and display a large increase toward the polar regions.

The e-folding time $(-1/\lambda_k)$ associated with these modes – of about 100 months – is approximately four times greater than the second largest e-folding time and we are thus in a situation where one mode may dominate the expansion in eqn. (3.11) and we could expect the least stable mode to give the shape of the temperature increase in a climate warming experiment. However, not all eigenvalues are real (the system has oscillatory modes)

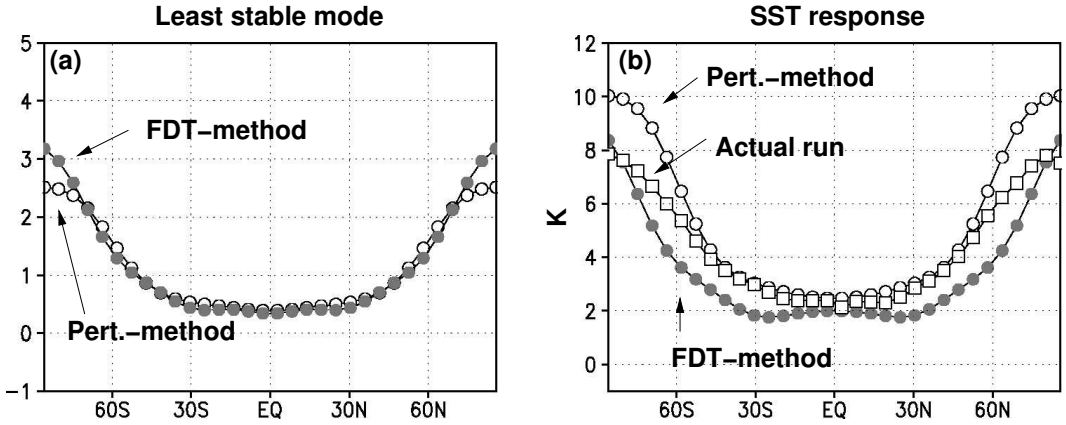

Figure 3.4: (a) The least stable mode of the Jacobian calculated using the perturbation method (open circles) and the FDT-method (closed circles). (b) The temperature increase resulting from a uniform 4 Wm^{-2} surface ghost forcing calculated from an actual model run (squares) and as linear estimates from the Jacobians derived using the perturbation method (open circles) and the FDT-method (closed circles).

so the analysis leading to eqs. (3.11) and (3.12) does not quite hold. Nevertheless, a glance at panel (b) of Figure 3.4 – showing the result of the forcing experiment discussed in the following subsection – reveals that the excitation of the least stable mode does, in fact, yield a resemblance between the modes and the temperature increase.

3.1.3 External climate forcing

Having calculated two approximations to the Jacobian, $\boldsymbol{\mathcal{R}}$, it is interesting to perform a climate change experiment to test the quality of our analysis. It will tell us how well the analyses can be used to predict the temperature increase accompanying an external climate forcing. The typical, in fact, almost canonical, climate forcing experiment is a doubling of the atmospheric CO_2 content. Figure 3.1(d) illustrates the external forcing by adding extra mass to the system.

Rather than actually doubling the CO_2 content in the model atmosphere, we will simplify matters somewhat. Doubling the CO_2 content in the code is not a problem, but if we wish to perform the linear analysis, eqn. (3.10) shows that we need to evaluate the $\delta\mathbf{b}_{Srf}$ arising due to this change. This is done by fixing the surface temperatures at equilibrium, doubling the CO_2 and recording the forcing on the surface budget. This will be done and discussed in Section 3.2 but here we will just approximate it with a uniform 4 Wm^{-2} ghost forcing (see Section 1.4.2). This is a widely accepted figure and in many models it actually holds quite well. In the present model (and the present setup) it holds well at low latitudes but at higher latitudes 2 Wm^{-2} is a better figure, so our experiment will probably exaggerate the high-latitude warming compared to a real CO_2 doubling.

Figure 3.4(b) shows the resulting temperature increase. The squares display the increase in

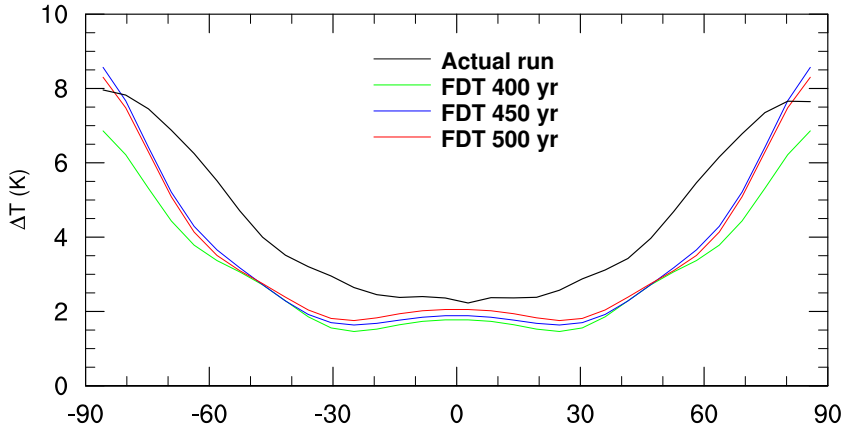

Figure 3.5: SST increases estimated using FDT Jacobians calculated from 400 years (green), 450 years (blue) and 500 years (red) of data. Convergence is seen around 450-500 years. The black line shows the temperature increase in the actual model run for reference.

the forcing experiment while the circles show the linear estimates performed using eqn. (3.10), a uniform 4 Wm^{-2} $\delta\mathbf{b}_{Srf}$-vector and the Jacobians evaluated using the perturbation method (open) and the FDT-method (closed). Firstly, we note that the temperature increase is quite well represented by the linear estimates and that it displays a close resemblance with the least stable modes. The perturbation method (open circles) performs well at low latitudes but overestimates the warming poleward of about 50° latitude. A possible explanation is that we in the perturbation method fix the SSTs while they display some variability in the mixed layer setup, especially at high latitudes. This lack of variability may affect the estimated high-latitude mean surface budget sensitivity. The shape of the FDT-method estimate (closed circles) does not resemble the actual response as well as that of the perturbation method, but the equatorial and polar increases of 2 and 8 K, respectively, are achieved almost perfectly. Moreover, it is interesting that a global mean temperature increase of 3.5 K may be estimated with such relatively good accuracy from the statistics of fluctuations whose global mean has a standard deviation of merely 0.03 K. Figure 3.5 shows the result of using only 400 years (green) and 450 years (blue) of data instead of the full 500 years (red). The curves converge when 450-500 years are used and we apparently need the full time series to obtain our best estimate.

3.1.4 Conclusions

We have demonstrated how linear analyses of the model climate can extract central information about its behavior under various perturbations and forcings. Following closely the derivations and analyses of Alexeev (2003) we introduced the basic assumptions and theory underlying the linear methods and we discussed the perturbation method of evaluating the Jacobian of the surface budget with respect to the SST field. Another method was also

introduced in which the fluctuation-dissipation theorem was exploited to derive the linear properties through observation of the model's unforced variability. We determined the eigenspectrum of the operator and compared the least stable modes obtained with the two methods. It was also shown that the response to a uniform 4 Wm^{-2} forcing resembled the shape of these least stable modes.

Although the purpose here was to assess the applicability of the FDT rather than to compete with the direct integration, it is tempting to ask: What would have been the easiest? The FDT-method cost us 500 years of integration while the perturbation method cost 8×20 years (one control and 7 perturbations), i.e., 160 years. The direct integration with the forcing cost about 30 years and it could thus seem that we had spent many hours (months) of computer time estimating a climate signal that could have been determined much cheaper and more accurately by just performing the experiment. This is, however, not the case, since by determining the Jacobian we have learned more about the system. For example, we can use it to estimate the response to an arbitrary forcing and the eigenspectrum provides information about the trajectory of an internal perturbation towards equilibrium. Moreover, we have seen that the polar amplification arises as an excitation of the least stable mode and thus couples to the system's dynamics rather than just the specific shape of the forcing.

An equally interesting property of the FDT-method is that we can extract this information without doing anything but running the model and observing its internal variability. From fluctuations, whose global mean have a standard deviation of 0.03 K, we could estimate temperature increases about 100 times greater in magnitude. The question then arises, whether one could determine the Jacobian of the real climate system (and hence its sensitivity) just by observing it. The answer is, that it should be possible in principle but there is a host of complicating factors. Zonal and hemispheric asymmetries due to the continents imply that we need to expand our basis to also include odd order and zonally asymmetric spherical harmonics. This would lead to a rapid increase in the dimensionality of the system and we would need even more observations to confidently determine the auto-covariance matrices – presently we have only about 130 years of data which is insufficient even in the zonally symmetric case. To complicate matters further, the analysis relies on a temporal constancy of the $\mathbf{S}$-operator – a condition we cannot expect to be fulfilled. The Jacobian depends (as discussed) on a collection of external parameters, Λ, such as CO_2, solar constant and volcanic activity which all have varied during the observational period.

A uniform forcing of the surface budget was found to lead to a far from uniform temperature response. The temperature signal seen here is the first example of polar amplification without ice-albedo feedbacks encountered in the present thesis. With all cryospheric effects on the SSTs eliminated, this result demonstrates that there are other aspects of climate dynamics that lead to polar amplification. These aspects are the key focus of the present thesis and will be treated thoroughly in the remainder thereof.

3.2 Polar amplification without albedo feedbacks

This section focuses on the physical mechanisms giving rise to the polar amplification encountered in the previous section and is based on the work presented by Alexeev, Langen and Bates (2005). We will consider the response in SST due to both the idealized 4 Wm^{-2} ghost forcing (see Section 1.4.2) and a doubling of atmospheric CO_2. To understand the responses we slice and dice the experiments in numerous ways: The ghost forcing is split up and only applied in certain zones, the forcing, $\delta\mathbf{b}_{Srf}$, due to the CO_2-doubling is evaluated, fixed SST-runs targeted at understanding the transient towards the new equilibrium are performed, and several different models, including EBMs and two different GCMs, are employed. All the experiments are carried out in the aquaplanet, no-seasons and no-sea ice configuration. Further specifics of the various model runs will we given later in the section.

We have found that when the model is run without sea ice, such that multiple equilibria are excluded, the equilibrium attained is independent of the specific procedure used when adding an external forcing to it. As discussed in Section 1.1, Alexeev (2003, hereafter, A03) and Shine et al. (2003) have found it particularly useful to first add the forcing, e.g. double the CO_2, while keeping the SST fixed at the unforced equilibrium. The atmosphere will spin up to match the change and will be in equilibrium (globally integrated surface and TOA budgets are equal) even though there are non-zero tendencies on the SSTs. In this manner the total radiative *and dynamical* surface forcing, $\delta\mathbf{b}_{Srf}$, due to the change may be evaluated. Knowing the Jacobian (as discussed in the previous chapter) or a scalar version thereof (for the global average surface budget and SST) the temperature response may thus be predicted. With the surface forcing recorded with the SSTs fixed, the model is switched over to interactive-SST mode (in our case mixed-layer mode), the surface temperature field equilibrates with the forcing and the sensitivity experiment is concluded.

Apart from providing the most reliable prediction of the SST response, this "fixed-SST strategy" also allows one to decompose the surface forcing into its various components. Applying the linear analysis of eqn. (3.10), the SST response resulting from these individual components may also be estimated. This was done by A03 and the longwave and latent heat flux components were found to play the dominant role in producing the response (Figure 9 in A03). The longwave forcing was centered mainly at high latitudes and gave a predominantly high-latitude response, while the latent heat forcing was centered almost exclusively at low latitudes but resulted in a near uniform global response. In total, this gave the polar amplified response as a result of comparable low- and high-latitude forcings, and this finding is the main motivation for the split-up of the ghost forcing used in this section (outlined in Table 3.1).

We propose here that the only possible way for our model climate to respond to a forcing with comparable magnitude at all latitudes is with the polar amplification pattern. If the surface budget sensitivity is the same at all latitudes[1], the low and high latitudes will initially

[1] This is, however, not the case. In fact, we will see later that differences in surface budget sensitivity tend

Experiment	Area		Forcing
Exp1	Global	90S to 90N	4 Wm^{-2}
Exp2	Tropics	30S to 30N	4 Wm^{-2}
Exp3	Extra-tropics	90S to 30S and 30N to 90N	4 Wm^{-2}

Table 3.1: Description of the three ghost forcing experiments performed with all models.

respond uniformly. The uniform temperature increase will strengthen the poleward atmospheric energy transport (heat and moisture) and, in turn, increase the upper tropospheric temperature and humidity at high latitudes. This results in a larger downwelling longwave flux at high-latitudes and increased warming. This polar amplified response tends to reduce the increased meridional heat transport – and perhaps even *counter* it – once equilibrium is approached, but the initial increase rules out the uniform or *equatorially amplified* response.

The basics of this idea are investigated in subsection 3.2.1 in an EBM where the ghost forcing experiments described in Table 3.1 are carried out. Subsequently, two different GCMs are used to test the robustness of the qualitative picture of the mechanism outlined above. Again, the three ghost forcing experiments are carried out and it is shown that the polar amplified response to the uniform forcing can be viewed as the sum of a local response to the high-latitude forcing and a global response to the low-latitude forcing. A number of fixed-SST experiments are conducted to demonstrate how the high-latitude surface budget feels a tropical SST change.

3.2.1 EBM experiments

The proposed mechanism for polar amplification is explored here in the simplest possible framework. We employ an EBM of the Budyko-Sellers type and effectively ask the question, *What is the simplest, physically plausible, addition we can make to the model and attain a non-ice albedo feedback-induced polar amplification?* Our starting point is a time-dependent energy balance equation written in terms of $x = \sin\phi$, where ϕ is latitude:

$$c\dot{T}(x) + D\frac{d}{dx}(1-x^2)\frac{d}{dx}T(x) = A + BT(x) - QS(x)(1-\alpha(x)), \tag{3.21}$$

where, as usual, T is the zonally averaged surface temperature, A and B give the linear parameterization of the outgoing longwave radiation at the TOA (as studied closer in Section 2.1), Q is a fourth of the solar constant, S is an annually averaged heating function and α is the latitude-dependent TOA albedo. The operator on the left hand side is the Laplacian in the coordinate x and D is a diffusion coefficient. S is expressed in terms of a two-mode Legendre expansion (see Appendix C) as $S(x) = 1 + S_2(3x^2-1)/2$, where $S_2 = -0.482$ yields

to strengthen the system's tendency to yield the polar amplification.

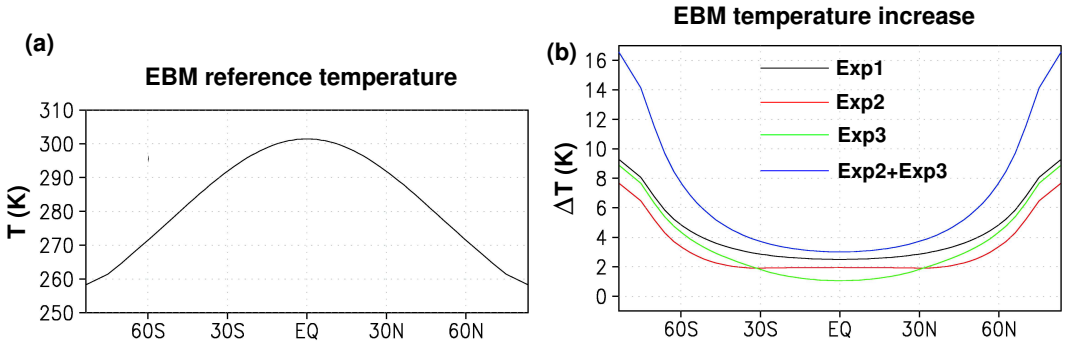

Figure 3.6: Results from the EBM experiments: (a) Equilibrium SST. (b) SST increase in Exp1 (black), Exp2 (red), Exp3 (green) and sum of responses in Exp2 and 3 (blue). With constant diffusion coefficient and active ice-albedo feedback the EBM produces a polar amplification in all three cases. Due to the non-linearity introduced by the ice-albedo feedback, the responses of Exp2 and 3 do not add up to that of Exp1.

a reasonable fit to the annually averaged heating function. The values $A = 205$ Wm^{-2}, $B = 2$ Wm^{-2}/K and $Q = 340$ Wm^{-2} were chosen and the temperature is measured in degrees Celsius. When the albedo is variable (it will in some of what follows be kept fixed), it takes on the value 0.3 where T is greater than -10°C and 0.6 where T is less than -10°C. This permits the model to include the ice-albedo feedback. The first term on the left hand side (giving the time dependence) was added simply to solve the energy balance equation through a forward integration in time. Since we are only interested in the equilibrium, the heat capacity, c, is chosen arbitrarily and merely controls the speed of convergence. With the above parameters the diffusion coefficient, D, is tuned and with a value of 0.445 the model has the present day-like temperature profile shown in Figure 3.6(a).

In this equilibrium the three ghost forcing experiments are performed by simply adding an extra forcing term on the right hand side of (3.21). The outcome is shown in Figure 3.6(b) for an active ice albedo-feedback: The black curve shows the equilibrium temperature increase in Exp1 while the red and green curves show the increases in Exp2 and Exp3, respectively. The blue curve shows the sum of the increases in Exp2 and Exp3. A number of features are evident: (i) All three experiments display a significant polar amplification, (ii) Exp3 yields a greater amplification than Exp2 and (iii) the result of Exp1 cannot be calculated as the sum of Exp2 and Exp3 as is the case for the forcings.

Attempting to reproduce the polar amplification without the ice albedo-feedback, we fix the surface albedo profile corresponding to the equilibrium found previously. The non-linearity of the albedo step function has now been eliminated from the energy balance equation rendering it linear in T. This is evident in Figure 3.7(a), which shows the result of repeating the three ghost forcing experiments. The warming in Exp1 equals the sum of the warmings in Exp2 and Exp3. There is no polar amplification in this case since B is constant with latitude leading to uniform increases in T. Uniform increases in T do not change the gradients and

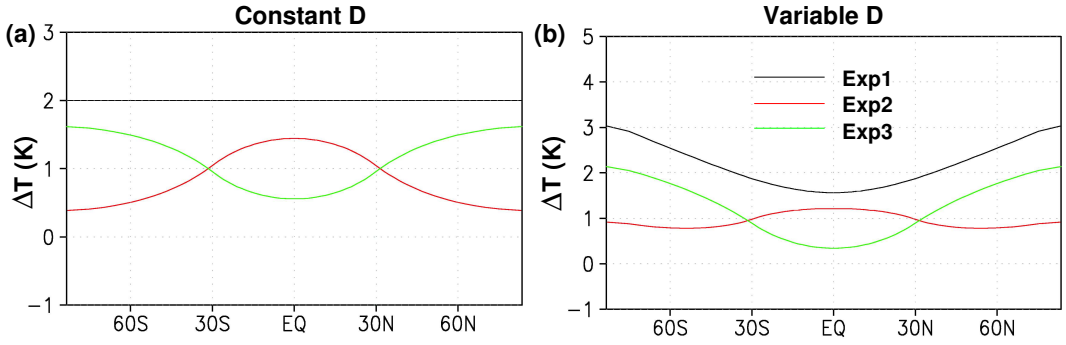

Figure 3.7: (a) As in Figure 3.6(b), for experiments with inactive ice-albedo feedback and constant diffusion coefficient. The sum of increases in Exp2 and 3 is not plotted, since it coincides exactly with the increase in Exp1. (b) As in (a), but for the experiments with global SST dependent diffusion coefficient. Clearly, the variable diffusion coefficient yields a polar amplification of the response.

the meridional heat transports thus remain unchanged. Since the albedo is unchanged, the value of the uniform increase can be calculated as 4 Wm^{-2}/B=2 K.

Exp2 and Exp3 both show amplified local warming and the global averaged warmings are in both cases 4 $\mathrm{Wm}^{-2}/B/2$=1 K, since again the albedo is unchanged and the meridional transports only redistribute the heat (we divide by 2 since only half of the Earth's area is being forced in Exp2 and Exp3). Since their sum equals 2 K everywhere, the two curves are each others' mirror images about the line T=1 K. In fact, the local warmings, i.e., the tropical average warming in Exp2 and the extra-tropical average in Exp3, are equal and the same holds for the non-local warmings. This stems from the linearity of the energy balance equation: The temperature perturbations set up changes in transport out of the forced area which are the same in both experiments. The symmetric way in which the tropics and extra-tropics are treated hence excludes the polar amplification.

This symmetry is not present in the GCMs which, as seen previously for the CCM3, do display polar amplification. One effect which is not modeled by the EBM is the increase in latent heat transport by a warmer atmosphere. In simple terms, a warmer atmosphere holds more moisture and with unchanged temperature gradient and eddy activity more heat will be transported polewards. This is demonstrated in Figure 3.8 showing the change in heat transport resulting from a 1 K globally uniform increase in SST[2]. The black curve shows the total heat transport change as implied by the TOA and surface heat budgets while the red curve is the latent heat contribution implied by the surface freshwater budget (see Appendix B for an account of how the implied energy transports are calculated). The large peaks in the red curve in the tropics are due to a strengthened Hadley circulation. This increases the equatorward latent heat transport at low latitudes which is largely compensated

[2]Results are shown here for the CCM3 but heat transport changes will be discussed further for both models later.

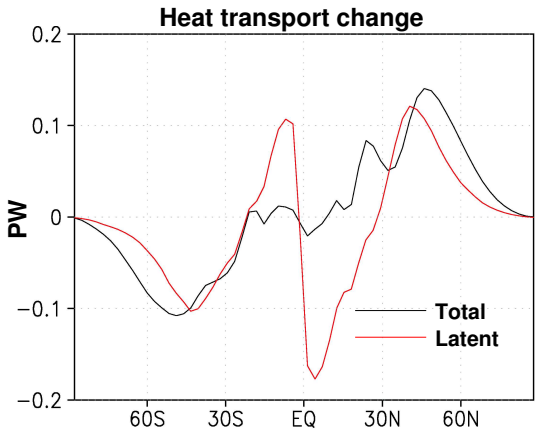

Figure 3.8: Increase in the meridional heat transport (black) and the latent contribution thereto (red) in a uniform 1 K SST increase experiment. This figure shows results for the CCM3 but changes in heat fluxes are shown for both models in Figure 3.14. The two curves are inferred from the TOA−surface heat budget and the surface freshwater budget ($P - E$), respectively (see Appendix B). The uniform warming is seen to yield an increase in the meridional heat transport at mid-latitudes, chiefly due to the latent heat contribution.

by a similar increase in the poleward dry static energy transport in the upper branch of the Hadley cell. The increase in the mid-latitude heat transport, which we are interested in when studying tropical-extra-tropical interactions, is seen to come about chiefly due to the latent heat transport change.

This effect can crudely be included in our EBM by letting the diffusion coefficient be given as

$$\begin{aligned} D(T_m) &= D_{ref} + \left.\frac{\partial D}{\partial T_m}\right|_{ref} (T_m - T_{ref}) \\ &= D_{ref} \cdot [1 + r \cdot (T_m - T_{ref})], \end{aligned} \tag{3.22}$$

where $D_{ref} = 0.445$ and $T_{ref} = 15$ C represent the diffusion coefficient and global mean temperature in the above equilibrium. T_m is the global mean temperature and r is the derivative of the heat transport with respect to T_m (normalized by D_{ref}). An illustrative value of 3%/K is chosen for this parameter in consistency with the increase seen in Figure 3.8. It is still an estimate in a crude parameterization, but while the magnitudes in the following naturally depend on the chosen value, the mechanism remains qualitatively invariant.

With this variable diffusion coefficient the above symmetry between low- and high latitudes is broken. While earlier an increase of temperature in a zone led only to an anomalous transport out of this zone, a temperature increase now leads to increased poleward transport in addition to the change in transport associated with the gradient changes. This leads to polar amplification of the warming as seen in Figure 3.7(b). Even though the above symmetry is broken, the linearity of the energy balance equation still holds and the response in Exp1

equals the sum of the responses in Exp2 and Exp3. The polar amplification arises as a result of a pronounced local response to the extra-tropical forcing and an essentially uniform global response to the tropical forcing.

We have found that with a fixed diffusion coefficient leaving meridional transports dependent only on the temperature gradient no polar amplification of the warming signal is seen unless the ice-albedo feedback is included. However, letting the diffusion coefficient increase with global mean temperature to crudely include effects of a warmer and moister atmosphere, polar amplification is seen without the ice-albedo feedback. As long as the ice-albedo feedback is excluded, the system responds linearly to the various ghost forcings such that the response in Exp1 equals the sum of those in Exp2 and Exp3.

The following, more general statement, is an EBM counterpart of the mechanism hypothesized earlier: *Polar amplification will always be seen in an EBM if (i) the sensitivity, B, of the TOA budget to SST perturbations is fixed at a uniform value, and (ii) the diffusion coefficient in the heat transport parameterization increases with SST, thus mimicking the increase in meridional latent heat transport.* If we apply an external forcing uniformly to such a system, the imbalance at the surface will produce an initially uniform temperature increase. This strengthens the meridional heat transport and the extra heat input to the extra-tropics will be larger than what can be lost to space, since the TOA sensitivity is uniform as is the initial SST increase. This implies a larger local SST increase at high latitudes which allows the TOA to release more energy from the system. In turn, this reduces the energy transport from the tropics and the system can eventually equilibrate. Hence, the only way an EBM with the above mentioned properties can respond to the 4 Wm^{-2} forcing is the pattern with higher SST increases at high latitudes. The more sensitive the energy transport is to the increase in SST, the more pronounced the polar amplification.

3.2.2 GCM experiments

This section describes the GCM experiments we have performed to test the polar amplification mechanism described above. Both ghost forcing experiments and fixed SST experiments are performed to provide a full qualitative picture of the processes at play.

Model description

As in Section 2.1, we again use both the CCM3 and the GEOS models for this investigation. The two models have different representations of physics and dynamics and are used to demonstrate the robustness of the hypothesized mechanism. They are run at comparable horizontal and vertical resolutions, on aquaplanets and without the seasonal cycle; "modified equinox" conditions as described earlier are employed.

- The CCM3 is run at T42 horizontal resolution with 18 vertical levels. Our modifications to the standard distribution are as described earlier. Again, we exclude all effects of sea

ice by treating grid points where the SST drops below freezing as open water points. All effects of clouds are kept in the code and the solar constant and CO_2 concentration are set to the CCM3 default values of 1367 Wm^{-2} and 355 ppm, respectively.

- The Goddard Space Flight Center GEOS model is described in A03, and it is, as in Section 2.1, run by Vladimir A. Alexeev. The horizontal resolution is 4°x5° and there are 20 layers in the vertical. Clouds are ignored in the radiation code.

The mixed-layer model (of depth $H = 50$ m) is coupled to the atmosphere in both models through the surface heat budget, and the tendency equation for the surface temperature, T_S, is, as usual, given in each grid point by

$$\rho_w c_w H \frac{\partial T_S}{\partial t} = F_{SW} - F_{LW} - F_{SH} - F_{LH} \ (+G), \tag{3.23}$$

where ρ_w and c_w are the density and heat capacity of sea water, respectively, and F_{SW}, F_{LW}, F_{SH} and F_{LH}, designate the net downward shortwave, the net upward longwave and the sensible and latent heat fluxes. As described in subsection 1.4.2, the term G added in parenthesis on the right hand side demonstrates how the ghost forcing is inserted into the mixed-layer. As in previous experiments, the two models are run until they reach a quasi-steady state, the time average of which is then considered the equilibrium climate. The uniform surface albedo of the GEOS model was tuned to 0.225 to yield a present-day-like SST profile, and that of CCM3 was then tuned to 0.05 to give a similar profile. The equilibrium climates, shown in Figure 3.9(a), were then perturbed by doubling the CO_2 concentration in the physics package. The models were again run to equilibrium and the responses are displayed in Figure 3.9(b). For both models, a distinct polar amplification is found; we will return to the details of the figure in the following.

For completeness, we repeat in Figure 3.10(a) these polar amplification patterns along with those obtained when running the GEOS model *with* clouds (surface albedo tuned to 0.15) and CCM3 *without* clouds (surface albedo 0.18). To facilitate comparison of the actual polar amplification, panel (b) shows the same curves scaled by their tropical mean SST increase. Comparing the green and blue curves, the CCM3 is clearly seen to have its polar amplification strengthened by the clouds. This is less clear in the GEOS model; in panel (a), the red curve seems to be an upward shift of the black curve, but when the polar SST increase is considered relative to the low-latitude increase, there is a slight amplification. Clouds are thus seen to strengthen the polar amplification in both models but are not solely responsible for it. The cloud effects in CCM3 giving this strengthening of the amplification will be touched upon later in Chapter 4.

We have chosen the two very different model configurations described above (giving the two extremes in Figure 3.10(b)) to illustrate that the same mechanism is at play in both.

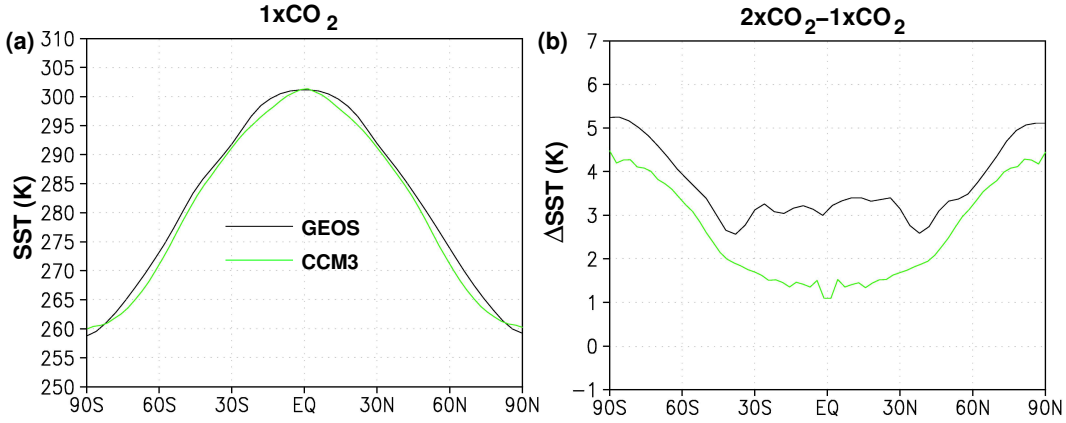

Figure 3.9: (a) Equilibrium $1xCO_2$ SSTs as function of latitude, GEOS (black) and CCM3 (green). (b) Difference between $2xCO_2$ and $1xCO_2$.

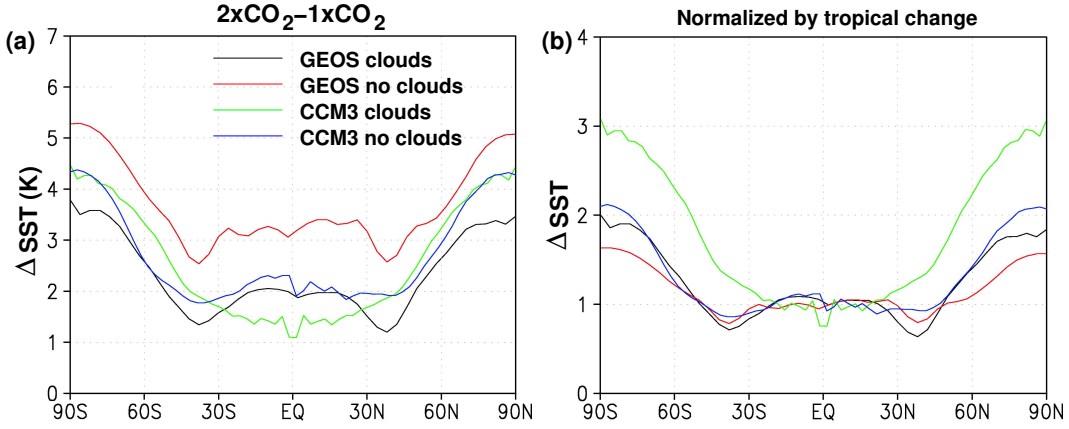

Figure 3.10: (a) SST change resulting from a doubling CO_2 in GEOS with clouds (black) and without clouds (red) and in the CCM3 with clouds (green) and without clouds (blue). The red and green curves are simply a repetition of Figure 3.9(b). (b) As in panel (a) but with changes normalized by their tropical mean value to ease comparison between the cases. For both models clouds are seen to strengthen the polar amplification.

		Exp2 Tropics only		Exp3 Ex-trops only		$2\times CO_2$	
		F	ΔT	F	ΔT	F	ΔT
GEOS	Equator	4	2	0	0.5	5	3.2
	Pole	0	2	4	3	4	5.2
CCM3	Equator	4	0.8	0	1	4	1.4
	Pole	0	0.8	4	5	2	4.2

Table 3.2: Round-number summary of forcings, F [Wm^{-2}], and responses, ΔT [K], in the ghost forcing (Exp2 and Exp3) and CO_2 doubling experiments.

$2\times CO_2$ forcing

As described earlier, the experiment was performed by first doubling the CO_2 while holding the SST fixed at the $1xCO_2$ equilibrium. The total dynamic-radiative surface forcing resulting from the change was recorded as the net surface imbalance (radiative and turbulent fluxes) and is shown in Figure 3.12(a). Both models have a maximum in the forcing at low latitudes and decreasing values at higher latitudes. As demonstrated in A03, the LW part of this forcing dominates at high latitudes since the low-latitude troposphere is already optically thick before the CO_2 change. This leads to a preference for warming of the high-latitude troposphere (surface temperatures are still fixed). Nevertheless, the surface feels a low-latitude maximum in the forcing (Figure 3.12(a)) which arises due to a large reduction in the latent cooling. When CO_2 is increased, the atmosphere warms and moistens leading to a decrease in the temperature and humidity difference between the surface and the lowest atmospheric layer. This, in addition to a weakening of surface winds resulting from the preferential high-latitude warming of the troposphere, decreases the evaporation rate.

The fifth column of Table 3.2 shows in round numbers typical near-equatorial and near-polar values of the forcing. The GEOS model in general has a larger forcing and a smaller meridional gradient and it is seen that the uniform 4 Wm^{-2} ghost forcing used in the following to mimic the CO_2 doubling is a better approximation in GEOS than in CCM3. The sixth column of the table gives for future reference the near-equatorial and near-polar temperature increases in the two models (Figure 3.9(b)).

Ghost forcing

Having completed the CO_2 doubling experiments and determined the surface forcing therein we turn to the ghost forcing experiments designed to help us understand the polar amplification. In Figure 3.11 we show the result of the three experiments (Table 3.1) with the two GCMs. The results are qualitatively similar to those obtained with the EBM: The tropical-only forcing (Exp2) gives a very non-local, almost uniform response, while the response to the

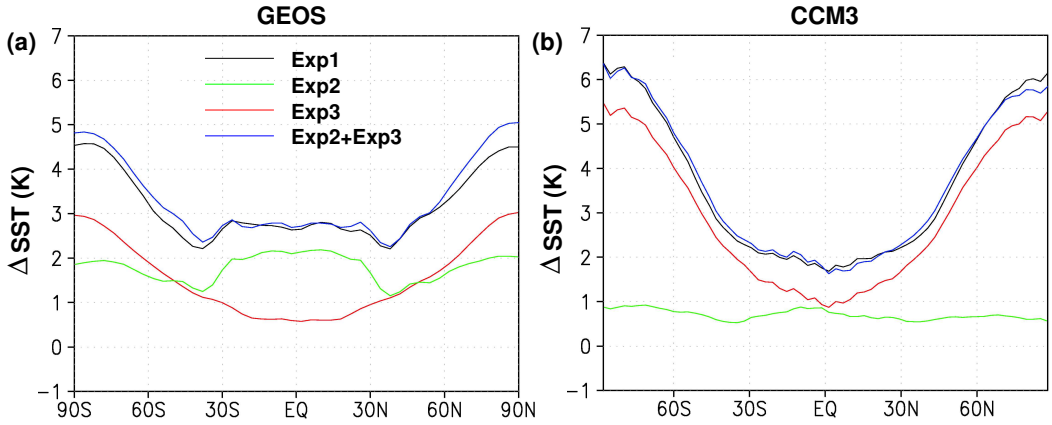

Figure 3.11: (a) Response of GEOS model to uniform 4 Wm^{-2} ghost forcing (black), to the tropical-only ghost forcing (green) and to the extra-tropical-only ghost forcing (red); sum of responses to the tropical-only and extra-tropical-only forcings (blue). (b) As in (a), but for CCM3. For both models, the sum of Exp2 and 3 yield the response in Exp1. The uniform forcing in Exp1 results in a polar amplified response which consists of a uniform response to the low-latitude forcing and a local response to the high-latitude forcing.

extra-tropical-only forcing (Exp3) is centered mainly at high-latitudes. Moreover, the sum of the responses in Exp2 and Exp3 almost coincides with the response obtained in Exp1 implying a linearity of our systems' SSTs with respect to the surface forcing.

This linearity turns out to be a very convenient feature allowing for a decomposition of the response to the uniform global surface forcing into the responses to the tropical and extra-tropical forcings. It will also be used in the following to provide a round-number account of the $2\times CO_2$ temperature response. For this purpose Table 3.2 summarizes the results of Exp2 and Exp3.

In the GEOS model, the local contribution to the warming at the poles amounts to 3 K, while the non-local response, with 2 K, is almost as important. The 6 K polar warming in the CCM3 results from a much larger local contribution of 5 K and a non-local contribution of about 1 K. The polar amplified response to the uniform ghost forcing can thus be explained as a superposition of a strong local response to the extra-tropical forcing and a remote response to the tropical-only forcing. Without the non-local response at high latitudes to the tropical forcing the pattern of the amplification would have been less pronounced. In fact, if there had not been a mechanism for communicating the tropical forcing to higher latitudes, the tropical response might have been considerably larger and the polar response significantly reduced.

Although there are qualitative features, such as linearity and global and local responses, in common between the two models, the responses differ on the quantitative level. This is not unexpected since we are, after all, dealing with two different GCMs. Both their dynamical formulations (one is spectral and the other is grid-point) and their physical parameterizations (of boundary layer processes, moist processes etc.) are different. It is not uncommon for two

	GEOS				CCM3			
	Equator		Pole		Equator		Pole	
	loc	rem	loc	rem	loc	rem	loc	rem
Sensitivity (K/Wm^{-2})	0.5	0.125	0.75	0.5	0.2	0.25	1.25	0.2
$\Delta T_{2\times CO_2}$ (K)	2.5	0.5	3	2.5	0.8	0.5	2.5	0.8
$\sum \Delta T_{2\times CO_2}$ (K)	3		5.5		1.3		3.3	

Table 3.3: First row: Local and remote sensitivity in near-equatorial and near-polar areas in the two models estimated from the Exp2 and Exp3 results summarized in Table 3.2. As an example, the equatorial sensitivities in the GEOS model are calculated as follows. "local": 2 K/ 4 Wm^{-2} =1/2 K/Wm^{-2} and "remote": 0.5 K/ 4 Wm^{-2} =1/8 K/Wm^{-2}. Second row: Local and remote contributions to temperature increase in the $2\times CO_2$ experiment. As an example, the equatorial contributions to the GEOS result are "local": 1/2 $K/Wm^{-2}\times 5Wm^{-2}$ =5/2 K and "remote": 1/8 $K/Wm^{-2}\times 4Wm^{-2}$ =4/8 K. Third row: sum of local and remote contributions.

different models to yield responses that differ by a factor of 2 to the same forcing. Moreover, with the idealized configurations employed here, we are obviously unable to make quantitative statements about the polar amplification and doubled CO_2 concentrations – we focus here on the qualitative features and mechanisms the models have in common.

Relating forcing and response

Given the linearity of the models' responses, the $2\times CO_2$ results shown in Figure 3.9(b) can roughly be inferred from Figures 3.11 and 3.12(a) and the summary in Table 3.2. Table 3.3 shows the local and remote sensitivities estimated from the numbers in Table 3.2. The "local" sensitivity is calculated from the temperature increase in the ghost forcing experiment where the area in question was forced and the "remote" sensitivity was calculated from the increase in the experiment where the opposite area was forced (see table caption for an example). In the second row, these sensitivities are multiplied by the $2\times CO_2$ forcing in Figure 3.12(a) (summarized in the fifth column of Table 3.2).

The sum of the local and remote contributions are given in the last line of Table 3.3 and give the linear estimates of the $2\times CO_2$ SST increases. These numbers should be compared to the actual values in the sixth column of Table 3.2. For the GEOS model, the estimates are remarkably accurate; the near-equatorial warming of 3.2 K is estimated as 3 K while the near-polar warming of 5.2 K is estimated as 5.5 K. The estimate for the CCM3 are of differing quality; the equatorial estimate of 1.3 K is very close to the actual 1.4 K warming while the polar warming of 4.2 K is only estimated as 3.3 K. The latter estimate is reasonable but not impressive and perhaps our two-point technique of estimating the warming suffers from the large meridional differences in the forcing.

With this technique we have decomposed the latitudinal differences in the $2\times CO_2$ warming into the local and remote responses. In the GEOS model the equatorial response consists of

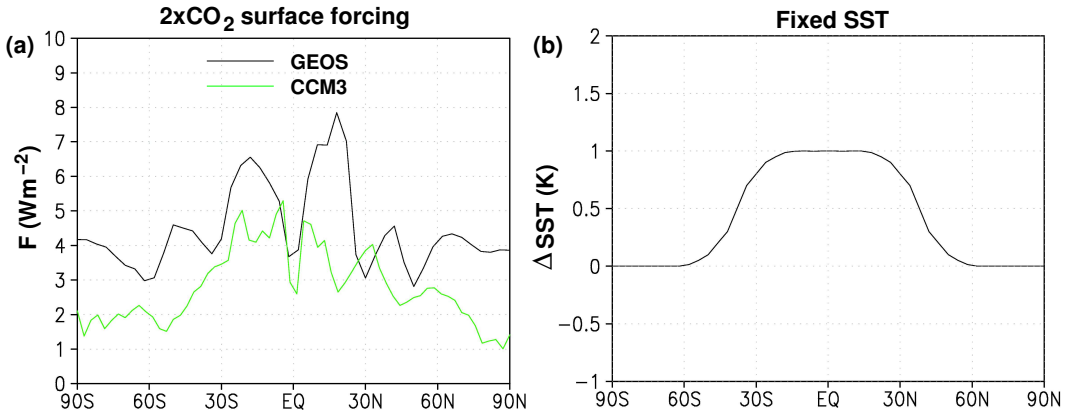

Figure 3.12: (a) Total dynamic-radiative surface forcing as a result of doubling the CO_2 concentration while keeping the SST fixed at the equilibrium value for GEOS (black) and CCM3 (green). The low-latitude maximum is due to a decrease in the latent cooling of the surface while the high-latitude forcing is due to an increase in the downward LW flux (individual components are not shown). (b) SST perturbation used in "tropical-only" fixed-SST perturbation experiment.

a primarily local contribution while the polar response is a result of almost equal local and remote contributions. To the degree that our analysis holds in the CCM3, the equatorial response also comes about due to comparable local and remote responses. The near-polar response is mainly due to the local forcing but the equatorial forcing contributes with almost 1 K and thus plays a part in producing the shape of the warming. As was concluded for the ghost forcing experiments, the $2\times CO_2$ polar amplification comes about due to a local response to the high-latitude forcing and a global response to the low-latitude forcing. The role of the latter contribution is most pronounced in the GEOS model.

The uniform 4 Wm^{-2} forcing results in global average SST increases of 2.8 K and 2.9 K in GEOS and CCM3, respectively. The global average sensitivity is thus approximately 0.7 $K/(Wm^{-2})$ in both models. On the other hand, the CO_2 doubling results in the rather different global average warmings of 3.3 K and 2.1 K. The surface forcings are, however, also quite different, namely 4.8 Wm^{-2} and 3.2 Wm^{-2}, and the sensitivities are here 0.7 $K/(Wm^{-2})$ and 0.65 $K/(Wm^{-2})$. The reduced sensitivity in CCM3 stems from the manner in which the 3.2 Wm^{-2} was imposed: It had most of its weight at low latitudes, while Figure 3.11(b) shows that adding heat to high latitudes much more efficiently increases the global average SST.

The remote response

In this subsection we will look into the reasons for the near-uniform global warming resulting from the tropical-only forcing in Exp2. We will do this by considering a fixed-SST experiment designed to mimic the conditions during the initial transient of the tropical forcing experiment.

Applying a tropical-only forcing will initially result in a temperature perturbation with a

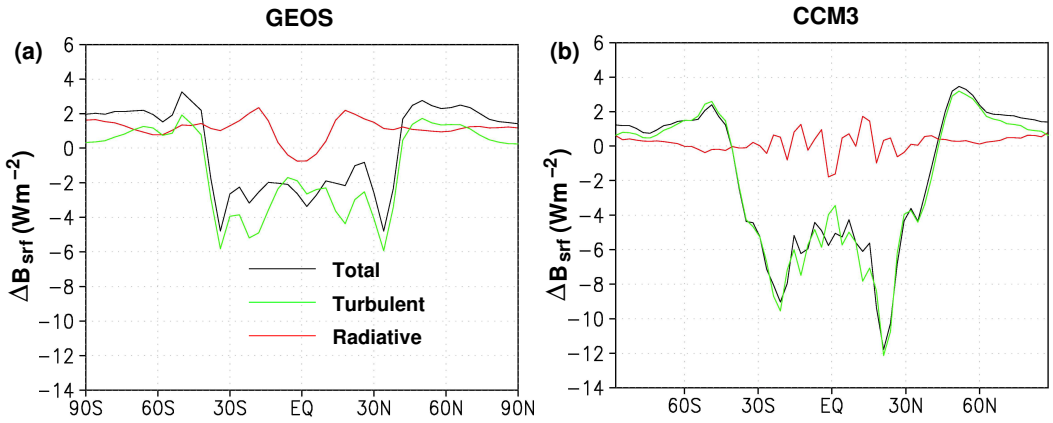

Figure 3.13: (a) Equilibrium response to the fixed "tropical-only" SST anomaly (Figure 3.12(b)) of the total surface budget of the GEOS model (black), turbulent fluxes (LH+SH, green), radiative fluxes (red). (b) as in (a), but for CCM3. In both models, the positive tropical SST anomaly leads to positive tendencies on the high-latitude surface budget.

shape roughly as shown in Figure 3.12(b). The change in the surface budget resulting from the perturbation is shown in Figure 3.13. A strong negative imbalance is seen in the tropics for both models tending to restore the tropical temperatures to their equilibrium value. At high latitudes, where the temperature field is unperturbed, there is, however, a positive imbalance (ca. 2 Wm^{-2} for GEOS and ca. 1.6 Wm^{-2} for CCM3). These would, if the SSTs were allowed to vary, tend to warm the high latitudes.

To determine how this high-latitude imbalance comes about, it is broken down into its radiative and turbulent components in Figure 3.13. For the GEOS model, the high-latitude warming is seen to be due mainly to a radiative forcing (in fact, mostly the longwave flux), while in CCM3 the radiative and turbulent fluxes both contribute. This can be understood by looking at the green curves in Figures 3.15 and 3.16, showing the temperature and specific humidity responses at 80N to the tropical temperature anomaly. In the GEOS model, the responses vanish at the very surface and the forcing must be radiative in origin. In CCM3, however, the lowest atmospheric layer displays increases in temperature and humidity which both inhibit the turbulent heat loss and thus augment the radiative tendency from the higher layers.

Fixed-SST experiments with a uniform 1 K increase and an extra-tropical 1 K increase (1 minus the curve in Figure 3.12(b)) were carried out in analogy to the tropical perturbation experiment. Figure 3.14(a) shows the equilibrium meridional atmospheric heat transport as implied by the TOA and surface energy budgets (see Appendix B for how this calculated). Panels (b) and (c) show the transport changes in the uniform (black), tropical (red) and extra-tropical (green) perturbation experiments for the two models, respectively. The changes in the transports are much like one would expect from the EBM picture outlined previously: When

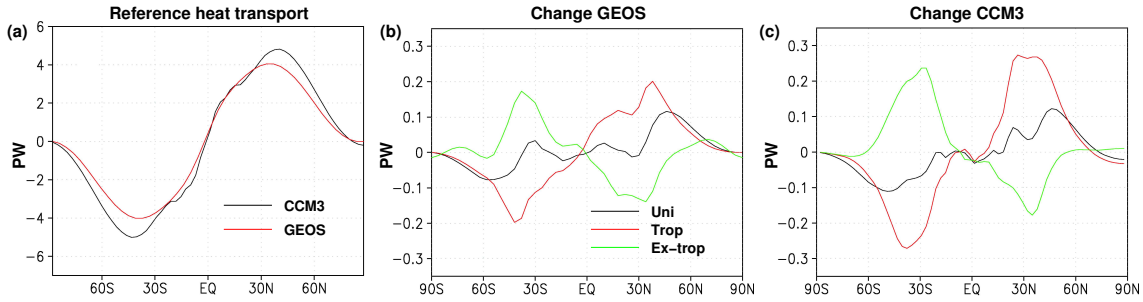

Figure 3.14: (a) Meridional atmospheric heat transport in the fixed reference SST run for GEOS (red) and CCM3 (black). (b) Change in heat transport in the fixed uniform (black), tropical (red) and extra-tropical (green) SST perturbation experiments for GEOS. (c) As in panel (b) but for CCM3.

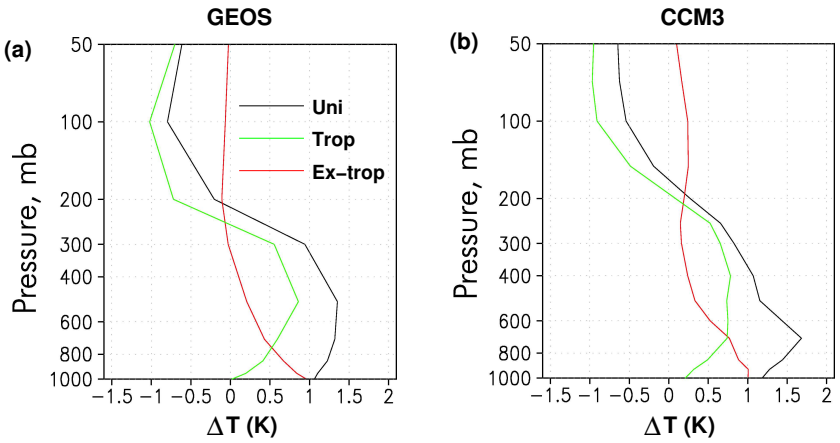

Figure 3.15: (a) Temperature response at 80N for GEOS in uniform 1 K SST perturbation experiment (black), tropical-only 1 K SST perturbation (green) and extra-tropical-only 1 K SST perturbation experiments (red). (b) as in (a), but for CCM3. The tropical SST anomaly has larger impact on the polar atmosphere above 750 hPa than does the high-latitude SST anomaly.

the temperature is increased uniformly, the gradients do not change but the atmosphere warms and transports more energy. When only the tropical SSTs are increased this effect is augmented by the effect of the increased gradient to lead to an even larger increase in transport. When only the extra-tropics are warmed the two effects compete and the net result turns out to be a decrease in the transport.

The changes in the temperature and specific humidity profiles at 80N resulting from these changes in SST and heat transport are shown in Figures 3.15 and 3.16. For both the temperature and humidity the changes look remarkably similar in the two models (apart from the differences in the lowest layers mentioned earlier). Comparing the green and red curves we conclude that the mid- to upper polar troposphere responds more strongly to a remote SST perturbation than one centered at high latitudes. The response to the extra-tropical

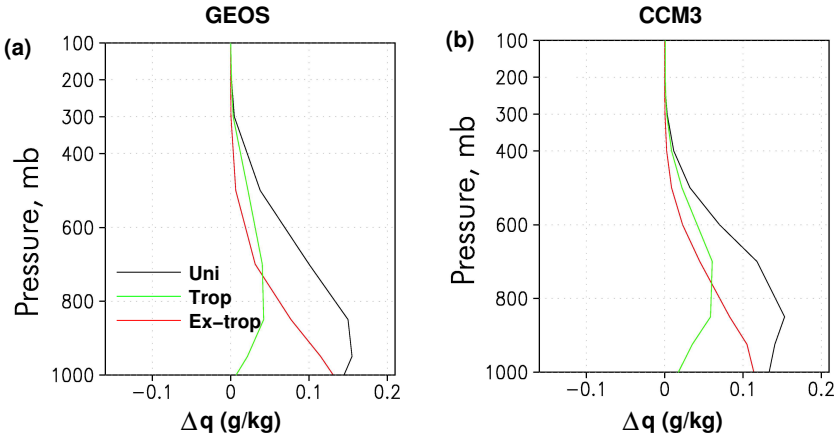

Figure 3.16: As in Figure 3.15, but for specific humidity. This figure and Figure 3.15 demonstrate the warming and moistening of the mid- to upper troposphere at high latitudes resulting from a tropical SST perturbation. This leads to the positive tendency on the polar surface budget seen in Figure 3.13.

perturbation produces a rather shallow response while the increased heat transport arising due to the tropical perturbation results in a deep tropospheric response in polar regions.

While the temperature increase arises due to the increased heat transport, it is unclear whether the moisture change is remote or local in origin. The meridional moisture transport has increased but due to the continuous recycling of moisture along the trajectories it is hardly discernible whether the extra moisture was imported to the high latitudes or if it was evaporated locally. More directly, the warmer polar atmosphere can, according to the Clausius-Clapeyron relation, hold more water vapor, and the free tropospheric water vapor feedback (as studied by e.g. Schneider et al., 1999) thus plays a part in producing the polar amplification by enhancing the longwave effect on the surface.

As was the case in the tropical perturbation experiment, the surface budget response to the extra-tropical SST perturbation (not shown) displays a local cooling tendency, albeit with a significantly smaller magnitude. Hartmann (1994) has demonstrated that the non-linearity of the Clausius-Clapeyron relationship renders the latent cooling more sensitive to perturbations in the warm tropics. This difference in sensitivities further contributes to forming the polar amplification pattern, since the tropics simply need to warm less than the extra-tropics to counter a given forcing. This topic has been studied in detail by Bates (2003).

Off-line radiation diagnostics

We have found that the changes in meridional energy transports warm and moisten the high-latitude mid- to upper troposphere. Here we use the off-line single-column radiation code of the CCM to determine the relative impacts on the high-latitude surface budget of this warming and moistening. First, the radiation code was run with the equilibrium profiles of

ΔF (Wm^{-2})	Ref	T	q	T and q	Cld	Lwp	Cld and Lwp	All
SW	0.0	0.018	-0.082	-0.065	-0.199	-0.303	-0.504	-0.567
LW	0.0	0.495	0.161	0.655	0.217	0.409	0.619	1.273
Net	0.0	0.511	0.078	0.589	0.016	0.105	0.114	0.705

Table 3.4: Changes in SW and LW components at 80N (in Wm^{-2}) for different perturbation profiles in 1D local diagnostic runs. All fluxes are positive downwards. "Ref" is the reference case while, for example, "T" means that the temperature profile from the perturbation experiment is used while all other profiles are taken from the equilibrium run. "T and q" means that perturbation profiles are used for both temperature and moisture. "All" means that all of the profiles are taken from the perturbation experiment.

temperature and moisture recorded at 80N in the reference run. The equilibrium profiles were then perturbed by the anomalies obtained in the "tropical-only" SST perturbation experiment.

With the perturbed profiles obtained with the GEOS model we performed three different experiments: We ran the single column model (i) with perturbed temperature and moisture fields, (ii) with perturbed temperature and unperturbed moisture and (iii) with perturbed moisture and unperturbed temperature. The anomalies in the radiative fluxes obtained in the latter two experiments add up linearly to the anomaly of ca. 1.5 Wm^{-2}, obtained in the former experiment. The temperature perturbation contributes with ca. 1.1 Wm^{-2} while the moisture perturbation contributes with the remaining 0.4 Wm^{-2}.

In the CCM3, where clouds have been included in all the experiments we have performed, profiles of cloudiness and cloud liquid water path were also collected and used along with temperature and moisture. The results are presented in Table 3.4 and are again linear with respect to the various perturbations, i.e., the sum "T"+"q" matches closely "T and q". The same applies for the cloud variables and the sum "T and q"+"Cld and Lwp" is almost "All". This linearity permits us to determine the relative importance of the various perturbations.

As for the GEOS model, it is found that the temperature perturbation dominates over the moisture perturbation in producing the surface forcing. It also dominates over the cloud effects. In fact, the relative influences of temperature, moisture and clouds are given roughly by the ratio 5:1:1 (compare with 3:1 for temperature and moisture in GEOS). The two different cloud variables clearly yield significant responses, but their combined SW and LW effects tend to cancel. Taking this cancellation into account, it is concluded that the bulk of the forcing stems from the LW effect due to the temperature perturbation, and even when clouds are included in the model, the LW forcing due to the tropical SST anomaly is produced in the same qualitative manner.

3.2.3 Conclusions

In Section 3.1 we encountered a polar amplified response to a uniform surface forcing in our system with all albedo feedbacks excluded. The pattern was identified as a feature of the linearized dynamics of the system and following the study of A03 it was attributed to an excitation of the least stable mode of the system's linearized operator. Here we have taken a more physical process based approach to diagnosing the reasons for this no-albedo feedback polar amplification.

In a series of EBM experiments we demonstrated that an increase in meridional heat transport resulting from a uniform or equatorially amplified temperature change disqualifies these patterns as possible end results in a climate change experiment. We found that when a crude representation of the increase in atmospheric heat transport in a warmer atmosphere was introduced, an amplification was seen even with equal low- and high-latitude sensitivities of the outgoing longwave radiation ($B = 2$ Wm^{-2}/K). A uniform forcing initially increases the temperature uniformly leading to an increased meridional heat transport. This initial increase in heat transport causes the extra-tropics to warm more than the tropics under the uniform forcing.

This idea was tested further in both the CCM3 and GEOS GCMs run in aquaplanet, no-seasons and no-sea ice mode. The implementations of both dynamics and physical parameterizations differ between the models and in one we included effects of clouds while in the other we did not. Figure 3.10 showed that clouds play a significant role in determining both the magnitude and shape of the warming due to an increase in atmospheric CO_2. The role of clouds will be considered closer in Chapter 4, but in these experiments they seem to enhance the polar amplification without being a prerequisite for it. In the detailed studies of the GCMs, one was run with and the other without clouds. Although the inter-model differences led to quantitative differences in the responses, the mechanisms responsible for the polar amplification pattern was concluded to be common to both models.

Three ghost forcing experiments allowed us to decompose the polar amplified response to a CO_2 doubling into local and remote components. We found that the responses to tropical and extra-tropical forcings add up linearly to the response from a uniform global forcing. It was concluded that, in both models, the polar amplification arises as a superposition of an essentially uniform response to the tropical forcing and a more local and higher amplitude response to the extra-tropical forcing.

The uniformity of the response to the tropical forcing comes about for several reasons. Firstly, our fixed-SST experiments showed that a uniform or equatorially amplified response leads to an increase in the poleward heat transport which warms and moistens the high-latitude atmosphere. These changes are amplified by the free tropospheric water vapor feedback and lead to a longwave heating of the high-latitude surface. This has also been seen in studies by Schneider et al. (1997, 1999) and Rodgers et al. (2003). The increase in heat

transport is encountered during a uniform or equatorially amplified temperature perturbation and thus excludes the possibility of the final response having such shapes (as concluded from the EBM experiments). When equilibrium is reached, however, the polar amplification will have decreased meridional temperature gradients enough to weaken, and perhaps even counter, the increase in transport. Hence, a straightforward comparison of the $1xCO_2$ and $2xCO_2$ equilibria and the various fluxes therein might not have provided us with the reasons for the exclusion of uniform or equatorially amplified responses.

The experiments with fixed SST perturbations also demonstrated differences in the sensitivity of the high- and low-latitude surface budgets to temperature perturbations. At low latitudes the SST needs to change less to counter an imposed forcing than is the case at higher latitudes. This effect strengthens the tendency for the heat transport mechanism to amplify the high-latitude warming. The strong stratification of the high-latitude troposphere tends to confine the temperature change in, for example, a $2xCO_2$ experiment to the very lowest atmospheric layers (e.g., Manabe et al., 1991, 1992). After ice-albedo feedbacks, this has been put forth to be the most important reason for the polar amplification (e.g., Hansen et al., 1997), but our tropical SST perturbation experiments suggest that such a local cause-and-effect relationship between the forcing and the response in lapse rate is insufficient: Through the large-scale circulation the high-latitude troposphere feels the tropical SST and produces a longwave forcing on the high-latitude SST which changes and, in turn, affects the local lapse rate.

3.3 Poleward energy transport in warm climates

In the previous section we showed the increase in poleward heat transport with global mean temperature to play a key role for the polar amplification. In the present-day-like climates studied there, this increase seems to be a rather robust result and the question of whether it generalizes to other types of climate states that Earth has encountered (or may encounter) arises.

Of particular interest in this respect is perhaps the very warmest periods during the early Cenozoic. The record of benthic foraminiferal $\delta^{18}O$ from oceanic sediment cores indicates that events such as the Late Paleocene Thermal Maximum ($\sim$55 Ma) and the Early Eocene Climatic Optimum ($\sim$51 Ma) exhibit extreme warmth and very shallow equator-to-pole temperature gradients (e.g., Zachos et al., 1994, 2001; Huber and Sloan, 1999, and references therein). Both marine and terrestrial paleontological proxy data supports this picture of a low-gradient greenhouse climate (e.g., paleo-distributions of vertebrates and crocodilians, Markwick, 1994).

In light of the above heat transport mechanism, it is especially interesting to examine whether increased atmospheric heat transport may resolve the problems that the climate modeling community faces when addressing this early Cenozoic "hothouse". Employing plausible values of elevated atmospheric CO_2 concentrations, studies ranging from simplified mod-

els (e.g., Saravanan and McWilliams, 1995) over AGCM-mixed-layer models (Shellito et al., 2003) to fully coupled ocean-atmosphere GCMs (Huber and Sloan, 2001) readily reproduce the global-mean temperature increases. The shallow equator-to-pole gradients, however, still pose unresolved questions: all applicable studies show too large tropical warming and too extensive ice and snow covers at the poles. This problem is central in several ways; our desire to understand the paleoclimatic proxies cannot be fulfilled before this inconsistency is removed. Moreover, should the proxies (and their current interpretation) turn out to be correct and the models turn out to lack a powerful polar amplifier in warm climates, the current projections of future anthropogenic warming may be significantly underestimated at high latitudes.

Resolving this problem may involve any or both of the following two types of mechanisms (Huber and Sloan, 2000): 1) radiative or convective mechanisms changing the surface budget in a local manner and 2) changes in atmospheric and oceanic meridional transports of energy. A potential player of the first type are polar stratospheric clouds which have been suggested to increase as a result of increasing concentrations of methane (Sloan and Pollard, 1998) or CO_2 (Kirk-Davidoff et al., 2002). This would yield a longwave warming of the high latitudes and may help resolve the problem.

Of the second type of mechanism, oceanic heat transport increases of sufficient magnitude to diminish the equator-to-pole temperature contrast have generally been absent in coupled AO-GCM studies (e.g., Huber and Sloan, 2001). With regard to the atmospheric component of the meridional energy transport, previous studies have not provided an unambiguous answer. Employing typically only a few scenarios these studies have concluded both that atmospheric transport changes may (Manabe and Wetherald, 1980) and may not (Pierrehumbert, 2002) play a role in producing the shallow gradient.

This section is based on the work of Caballero and Langen (2005) and presents a systematic study of the dependence of the atmospheric energy transport on global mean temperatures and meridional gradients. Other investigators (e.g., Rind, 1998; Huber and Sloan, 1999) have previously employed fixed SST perturbations in studies of the very warm periods of the Earth's past, but here we consider a range of scenarios to construct regime diagrams of the atmospheric energy transport.

3.3.1 Energy transport regimes

Experimental configuration

A large set of runs was performed with the PCCM3 atmospheric GCM (run by Rodrigo Caballero). This model is the atmospheric part of the Fast Ocean-Atmosphere Model (FOAM, Jacob, 1997) and consists basically of the dynamical core of the CCM2 and the physical parameterizations of the CCM3.6. A horizontal resolution of T42 and the usual aquaplanet lower boundary condition is employed. Sea ice forms when the specified surface temperature is below the freezing point.

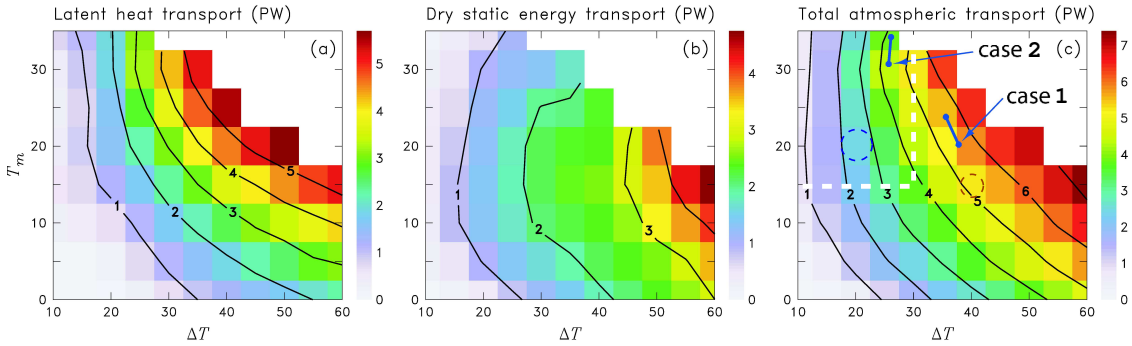

Figure 3.17: Peak (a) latent heat transport, (b) dry static energy transport and (c) total poleward energy transport. In panel c, the blue lines correspond to the climate change experiments described in the next subsection, while the dashed red and blue circles illustrate approximately the present-day and Early Cenozoic warm period climates, respectively. The white dashed line marks approximately the area where the energy transport is insensitive to T_m. White denotes the cases excluded due to the maximum temperature exceeding 45°C.

Fixed SSTs are specified as zonally symmetric combinations of zeroth and second order Legendre polynomials (see Appendix C), $T_s(\phi) = C_0 + C_2(3\sin^2\phi - 1)/2$, where C_0 equals the global-mean temperature, T_m, and ϕ is latitude. Since the equator-to-pole temperature difference is $\Delta T = -3C_2/2$, the specified profile re-writes to

$$T_s(\phi) = T_m - \Delta T \frac{3\sin^2\phi - 1}{3} \ . \tag{3.24}$$

With this formulation T_m is varied in 5°C intervals between 0°C and 35°C and ΔT is varied in 5°C intervals between 10°C and 60°C. Lacking faith in the ability of the model's parameterizations to deal properly with surface temperatures warmer than about 45°C, we have excluded cases where this temperature is reached. A total of 70 runs were thus performed and each was run for 4 years of which the last 3 were used in the following.

Results

Figure 3.17 shows the atmospheric heat transports in the 70 experiments. The total (panel c) and latent (panel a) heat transports were inferred from the TOA and surface energy budgets and the freshwater (evaporation minus precipitation) budgets, respectively (see Appendix B). The dry static energy transport (panel b) was calculated as the difference between the total and the latent heat transport. The value plotted is the maximum value poleward of 25° latitude averaged between the two hemispheres. 25° was chosen to separate the mid-latitude maximum from the Hadley cell maximum, providing for the possibility of determining it objectively.

In the vicinity of the present-day climate, i.e., $(\Delta T, T_m) \simeq (40, 15)$°C (red circle), both the

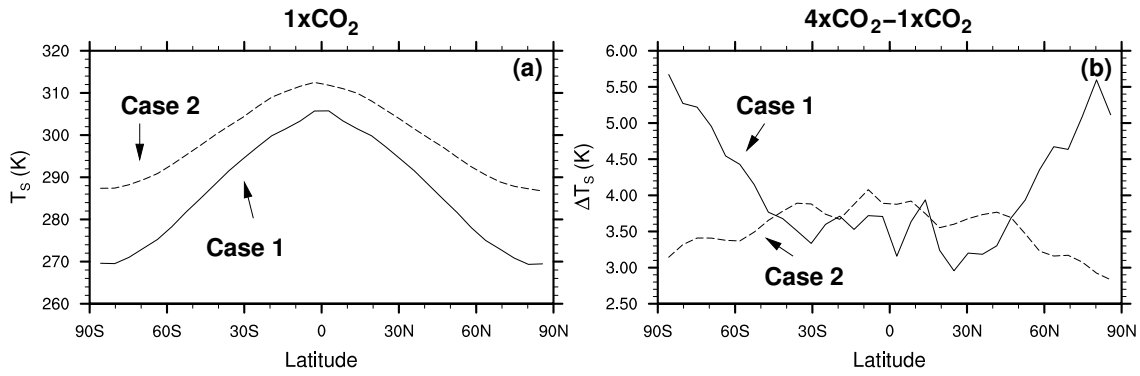

Figure 3.18: (a) Time and zonal average of the reference climates in Case 1 (solid) and Case 2 (dashed); (b) Temperature change resulting from $4\times CO_2$. This demonstrates the dependence of the meridional structure of the temperature change on the local shape of the heat transport iso-lines in Figure 3.17(c); one results in polar amplification while the other results in equatorial amplification.

latent and dry static energy transports behave much like we would expect from the variable-diffusion EBM used in the previous section: dry static energy flux increases with increasing temperature gradient but is rather insensitive to global-mean temperature, while the latent heat transport increases with both gradient and global-mean temperature. This mirrors an increase in baroclinicity with gradient and an increase in atmospheric moisture with global-mean temperature. The absolute value of atmospheric heat transport for the present-day climate agrees well with the 5.0 PW found by Trenberth and Caron (2001) in their detailed analysis of Earth Radiation Budget Experiment data and ECMWF and NCEP-NCAR re-analyses[3].

This picture changes in different climates. The dry static energy transport generally depends more strongly on ΔT than on T_m but there is some dependence on T_m: first it increases with T_m but when approximately 15°C is reached, it decreases. The latent heat transport generally increases with both ΔT and T_m but in the warm, low-gradient climate discussed above, the latent heat transport becomes almost insensitive to T_m. The resulting picture is one where the total poleward energy transport almost only depends on ΔT when $T_m > 15°C$ and $\Delta T < 30°C$. Consequently, changes in the poleward atmospheric energy transport cannot be invoked to explain the low gradients once this regime is approached. An alternative explanation of the proxy records must be sought.

3.3.2 Climate change experiments

In the Section 3.2 we considered closely the role played by the atmospheric heat transport in amplifying the polar warming in a present-day-like climate. Here we perform two fur-

[3]The 5.0 PW found by Trenberth and Caron (2001) is an enormous upward revision compared to earlier estimates of about 3 PW (by, for example, Carissimo et al., 1985)

ther warming experiments to assess the degree to which the shape of the atmospheric heat transport in Figure 3.17(c) sets the shape of the temperature change in different regimes. We employ the CCM3.6 in the same mixed-layer configuration used earlier in the thesis, namely a horizontal resolution of T21 and fixed albedos and ocean transports. To focus on the feedback associated with the sensitivity of the atmospheric heat transport we made a new addition to the simplified setup: Clouds were in each grid-point specified as the time-average taken from a reference run. Two different cases were considered:

Case 1 Clouds were sampled from a run identical to those used as the present-day-like climate in the previous sections in this chapter. These clouds were then time-averaged and re-inserted into the radiation code of the model and a new spin-up run was performed. This resulted in a warming of about 5 K and this warmer climate is the reference climate for our Case 1 experiment[4]. The coordinates of this climate in Figure 3.17 are $(\Delta T, T_m) = (37.8, 20.2)^\circ$C.

Case 2 In this second case we increased the q-flux from the typical strength of 50 used in Case 1 (and throughout most of the thesis) to strength 230 (see Section 1.4.2) resulting in a significant reduction of the meridional temperature gradient. Again, an initial run was performed from which the clouds were sampled and a new run was performed using the time-average of these clouds. This resulted in the reference climate used for Case 2. The coordinates are $(\Delta T, T_m) = (25.7, 30.7)^\circ$C.

Figure 3.18(a) shows the reference climates for the two cases while panel (b) displays the temperature change resulting from a quadrupling of the atmospheric CO_2 content (still keeping the clouds fixed at their reference value). The blue segments in Figure 3.17(c) summarize these results: in Case 1, ΔT decreases by about 2 K while in Case 2 it increases slightly as climate warms – this is actually an equatorial amplification. These findings are entirely consistent with the sensitivity of the heat transport seen in Figure 3.17(c). In the absence of sea ice and cloud feedbacks the heat transport feedback attains a dominant role in setting the temperature gradient change and the experiments (blue segments) will have a tendency to move in directions close to the heat transport iso-lines. To understand this, it is again instructive to consider an "initial" uniform temperature change resulting from the forcing (as was done in Section 3.2). In Case 1, a uniform warming (moving directly upwards in Figure 3.17(c)) will lead to a large increase in heat transport which, in turn, will decrease the temperature gradient deflecting the trajectory to look more like the nearby iso-lines. Conversely, a uni-

[4]This warming of 5 K in global average resulting from using fixed clouds rather than internally calculated clouds is the topic of Chapter 4. There we assess both the reasons for and the implications of this effect. We conclude that, when trying to eliminate cloud feedbacks, a time-varying specification of clouds should be used to avoid this effect, otherwise a completely different reference case will be considered. It is not a problem in this case, however, since we actually are interested in looking at other areas in our regime diagram than the present-day-like climate.

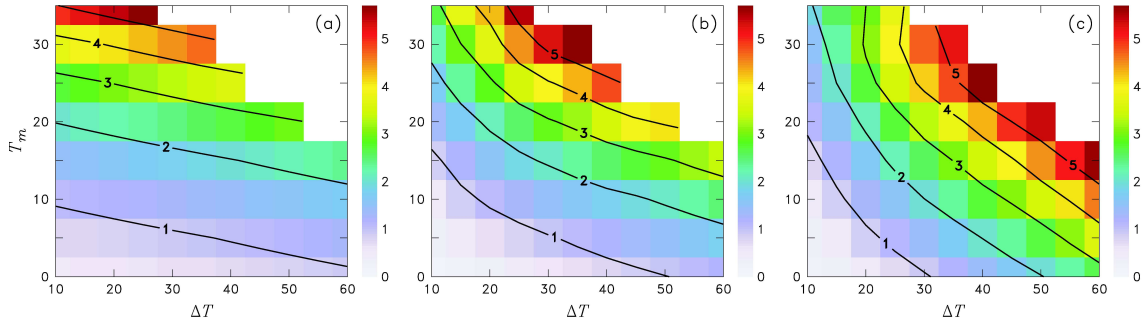

Figure 3.19: Meridional latent heat transport estimated (a) as $AVq_s(T_{Src})$ with $V = 10$ ms^{-1}, $T_{Src} = T_S(25°\text{C})$ and A an arbitrary constant; (b) as in (a) but using $V = \sqrt{2EKE}$ as plotted in Figure 3.20(a); (c) as $A\cos\phi_{ST}Vq_s(T_{Src})$ where V is as in (b), ϕ_{ST} is the latitude of the storm track axis and $T_{Src} = T_S(\phi_H)$ is the surface temperature evaluated at the poleward boundary of the Hadley cell, ϕ_H. Units are again PW, but all panels have been arbitrarily scaled.

form increase in Case 2 decreases the heat transport slightly and the temperature gradient is increased.

None of the two trajectories (in $(\Delta T, T_m)$-phase space) are, however, perfectly aligned with the heat transport iso-lines. In fact, the heat transport increases by about 0.2 PW in both cases. In light of the meridional inhomogeneities in both the forcing due to CO_2 changes and in the temperature changes, this is not surprising. In equilibrium, the collective transport of energy by the atmosphere and ocean (fixed in our case) cancels exactly the TOA radiative imbalance. If a climate change yields only small changes in the net TOA balance, the final state will be situated close to the initial iso-line. In our case, the forcing due to the CO_2 change is non-uniform and the changes in both the OLR and the absorbed solar radiation may display non-uniformities (due, for example, to changes in the moisture structure resulting from circulation changes; see Section 2.1). This leads to the slight iso-line crossing.

The result of climate changes along energy transport iso-lines is consistent with a point made by Boer (1995) in his $2\times CO_2$ study with an AGCM-mixed-layer model: Despite significant changes in circulation, the net atmospheric heat transport was unchanged in the $2\times CO_2$ climate. The general activity of the atmosphere decreased, resulting in decreased dry static energy transports, but this change was, however, canceled by an equal increase in latent heat transport due to the warmer, moister atmosphere.

3.3.3 The warm regime

The insensitivity of the heat transport to T_m in the warm regime is at variance with the situation in the present-day-like climate (as considered in Section 3.2). In this regime, uniform or even equatorially amplified (Case 2) responses to CO_2 changes are possible, and this subsection is therefore devoted to pinpointing the reasons for the insensitivity. We do this by

constructing the simplest possible parameterization of the transport that mimics the behavior.

The poleward latent heat transport across a latitude circle, ϕ, is given by

$$F_L(\phi) = \frac{L_v}{g} a \cos\phi \iint vq \; d\lambda dp, \tag{3.25}$$

where L_v is the latent heat of vaporization, g the acceleration of gravity, a the radius of the Earth, v the meridional velocity, q the humidity, λ the longitude and p the pressure. This quantity is in the extra-tropics dominated by the eddy fluxes in the storm tracks where moisture is picked up at the surface on the equatorward flank and transported upwards and polewards. Here the lower temperatures cause the moisture to condense and the latent heat is released. Thus, the eddy mixing does not act upon the contrast between the low- and high-latitude boundary-layer humidities, but rather that between the source region value and that aloft, which due to the low temperature essentially vanishes (Pierrehumbert, 2002). Hence, a plausible scaling for the latent heat transport by the eddies is

$$F_L \sim V q_s(T_{Src}), \tag{3.26}$$

where V is a typical meridional velocity scale, q_s the saturation specific humidity and T_{Src} the typical surface air temperature in the moisture source region on the equatorward flank of the storm track (Pierrehumbert, 2002). If both V and the position of the source region stays constant, the latent heat flux will, according to this scaling and the Clausius-Clapeyron relationship, increase exponentially with T_{Src}. This is plotted in Figure 3.19(a), where we have used $V = 10$ ms^{-1} and $T_{Src} = T_S(25°\text{C})$ and multiplied by an arbitrary constant, A, simply to ease comparison. Note that we are not trying to predict the absolute value of the transport; we are merely studying the dependence on ΔT and T_m. In this simple form, the scaling clearly fails to capture the important features of the actual latent heat transport in Figure 3.17(a).

We can attempt to improve the prediction by taking the velocity scale, V, from the model runs instead of the constant 10 ms^{-1}. We use $V = \sqrt{2EKE}$, where EKE is the eddy kinetic energy, $(v'^2 + u'^2)/2$, averaged over a 30° band around the storm track axis below 500 hPa. We define the storm track axis as the latitude with maximum eddy kinetic energy below 500 hPa. In this manner we capture the typical velocity scale in the region (horizontally and vertically) which actually performs the mixing. Figure 3.20(a) shows V calculated in this manner while Figure 3.19(b) shows the latent heat flux calculated with the scaling (3.26) using this V. This has led to some improvement (comparing again with Figure 3.17(a)), but the dependence on T_m is still too strong in the warm regime.

Figure 3.20(b) shows the latitude of the storm track axis, ϕ_{ST}, and we see a clear poleward migration of the axis with increasing T_m. To fully understand the insensitivity to T_m of the latent heat transport we need to examine closer the consequences of this change in the general

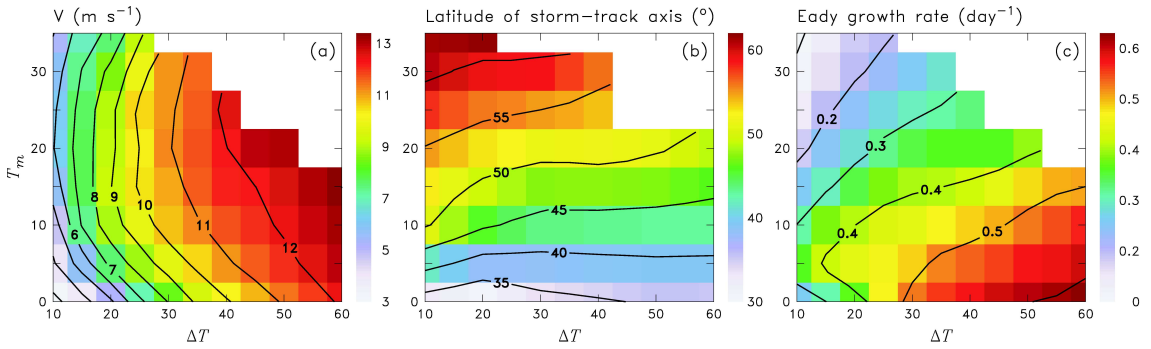

Figure 3.20: (a) Typical velocity scale, V, calculated as $\sqrt{2EKE}$ averaged over a 30° band around the storm track axis below 500 hPa, (b) latitude of storm track axis evaluated as the latitude with maximum eddy kinetic energy below 500 hPa and (c) Eady growth rate, $\sigma_{BI} = 0.31f|\partial u/\partial z|N^{-1}$, averaged over the same 30° band as in (a).

circulation. Two effects pertain: As the storm tracks migrate poleward, 1) the source region of the mid-latitude moisture migrates with them and 2) the length of the latitudinal band along which the integral in (3.25) is taken decreases with a factor of $\cos\phi_{ST}$. In Figure 3.19(c) we show the latent heat transport now accordingly proportional to

$$F_L \sim \cos\phi_{ST} V q_s(T_{Src}), \tag{3.27}$$

where V is as in Figure 3.20(a) and $T_{Src} = T_S(\phi_H)$ is the surface air temperature evaluated at the poleward boundary of the Hadley cell, ϕ_H. This boundary is evaluated as the first (from the equator) zero-crossing of the zonally averaged meridional stream function at the 500 hPa level. Our simple formulation of the transport now does a good job of capturing the main features of the dependence on ΔT and T_m, especially in the warm, low-gradient regime.

The dry static energy flux can, in analogy to the scaling (3.26) for the latent heat, be approximated by

$$F_{ds} \sim V\Delta T, \tag{3.28}$$

since ΔT is the temperature contrast being acted upon by the mid-latitude eddy mixing (e.g., Pierrehumbert, 2002). Therefore, with fixed ΔT one would expect the dry static energy transport to mirror the development of the meridional velocity scale, V. Comparing Figures 3.17(b) and 3.20(a) we confirm that this, in fact, is the case. Both quantities increase with T_m at low temperatures and decrease at high temperatures.

Since the energy transport regimes depend on V, it is desirable to account for the rather surprising behavior of first increasing and then decreasing values of this quantity with increasing T_m. According to the theory of baroclinic instability, a suitable measure of the baroclinicity (which tends to control the development of transient eddies and thereby V) is given by the

so-called Eady growth rate maximum (e.g., Hoskins and Valdes, 1990). Lindzen and Farrell (1980) considered exponentially growing solutions to the geostrophic streamfunction equation, and through a series of analytical arguments and numerical integrations they found that this growth rate takes on approximately the value

$$\sigma_{BI} = 0.31 f \left| \frac{\partial u}{\partial z} \right| N^{-1}, \tag{3.29}$$

where f is the planetary vorticity, N is the Brunt-Väisälä frequency giving the static stability and u the zonal velocity. The vertical velocity shear is, according to the thermal wind relation, proportional to the meridional temperature gradient. The local level of baroclinicity is thus proportional to the meridional temperature gradient and inversely proportional to the static stability. This growth rate, averaged over the same band as V in Figure 3.20(a), is shown in Figure 3.20(c) and decreases strongly with increasing T_m. This decrease in growth rate along lines of constant ΔT is due to a general increase in static stability with increasing T_m, since the vertical velocity shear is unchanged. This explains the decrease in eddy kinetic energy in the warm climates but is inconsistent with the increase in cold climates. Moist processes are known to increase the growth rate and Lapeyre and Held (2004) show that this effect on the flow's properties may be captured in a dry model by substituting the static stability with a reduced effective static stability. We speculate that this reduced effective static stability increases baroclinicity at low temperatures, but is overwhelmed at higher temperatures by the increase in actual static stability.

We have not pursued an explanation of the poleward migration of the storm tracks (seen in Figure 3.20(b)), but we speculate that perhaps the increase in static stability at high temperatures preferentially occurs at lower, warmer latitudes. This would favor a poleward shift in the baroclinicity maximum and thereby also the storm tracks.

3.3.4 Conclusions

By studying a broad range of climates we have constructed regime diagrams of the poleward atmospheric energy transport. We find that the transport becomes insensitive to the global mean temperature in the warm, low-gradient climates where it is most needed to explain the proxy records. We attribute the insensitivity to two main dynamical effects: 1) the mid-latitude eddy kinetic energy decreases as the global-mean temperature increases over 15°C, due to an increase in the background static stability, and 2) the storm tracks migrate poleward as the temperature increases and this decreases both their moisture supply and zonal extent.

Our results thus suggest that the heat transport mechanism identified in Section 3.2 is unable to account for the low gradients inferred from the proxies. The fact that we have employed aquaplanet lower boundary conditions may, however, be of some significance here: large scale changes in continental distribution and orography may alter the stationary wave patterns such as to modify the shape of the energy transport iso-lines in Figure 3.17(c). An-

other important caveat to the present conclusions is the question of whether the mechanisms identified actually operate in nature. On the theoretical level, we are, for example, beginning to understand the link between the meridional temperature gradient and static stability (e.g., Held, 1982; Juckes, 2000; Schneider, 2004), but we lack an understanding of the role played by the global-mean temperature. On the modeling level, transports calculated here could be inaccurate due, for instance, to mistreatment of sub-grid scale moist processes in the warm climates.

Crossing iso-lines on the scale implied by comparing the positions of the red and blue circles in Figure 3.17(c) requires major changes in the meridional structure of the TOA radiative imbalance and/or the oceanic circulation. If our results are accurate (or even reasonably so), we need such changes to account for an equivalent transport of almost 3 PW. With the rather small changes in oceanic transport implied by modeling results (e.g., Saravanan and McWilliams, 1995; Huber and Sloan, 2001), we must rely on enormous changes in the TOA radiative budget and here the proposed mechanisms associated with polar stratospheric clouds (e.g., Sloan and Pollard, 1998; Kirk-Davidoff et al., 2002) may turn out to be important.

Chapter 4

Non-linear cloud variability effects

In Section 3.3 we ran the model with the cloud field specified in each grid point as the time-mean value from a reference run. This resulted in a global average warming of 5 K relative to the reference run with internally calculated clouds. In this chapter, which is based on the work of Langen and Caballero (2005), we study closer the reasons for and the consequences of this effect. Clouds are generally observed to have a strong impact on Earth's radiative budget (Ramanathan et al., 1989) and cloud feedbacks can therefore exert potentially crucial influence on the climate system's response to external forcing, and may, as mentioned earlier, explain some outstanding features of ancient climates (Sloan and Pollard, 1998; Kirk-Davidoff et al., 2002). However, the representation of cloud processes within general circulation models (GCMs) remains problematic, and is a leading source of uncertainty in estimates of climate sensitivity (Houghton et al., 2001). This reflects the almost overwhelming complexity of clouds and cloud-climate interaction (Randall et al., 2003; Stephens, 2005), and the problem is, in fact, rich enough that, despite several decades of research, many of its aspects have yet to be explored in detail.

The question of cloud-climate interaction can be divided into two parts: 1) one involving the way in which dynamics and thermodynamics create clouds, and 2) the other concerning the way in which clouds interact with radiation and thus feed back on the thermodynamic and dynamic fields. Both are important, largely unsolved problems (Stephens, 2005). The scope of the present chapter falls into the second part; specifically, we analyze the variability effect of clouds on their mean radiative impact in the context of the CCM3. A useful measure of cloud impact on radiative transfer is cloud radiative forcing (CRF), defined as:

$$\mathrm{CRF} \;=\; R \;-\; R_{\mathrm{clr}},$$

where R is the total downward top-of-atmosphere radiative flux at a given longitude-latitude point, and R_{clr} is what R would be if clouds were instantaneously removed[1]. CRF is, as hinted

[1] This can be done explicitly in models, while, in observations, R_{clr} must be estimated from nearby (in space

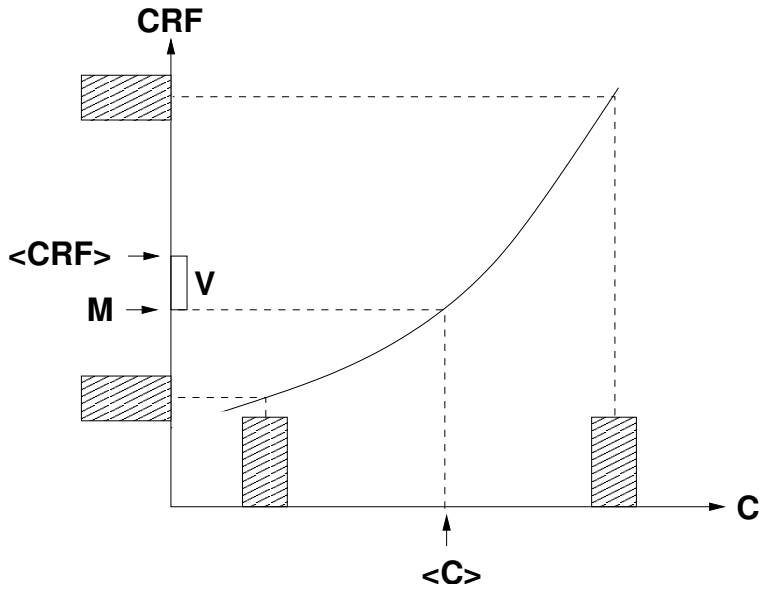

Figure 4.1: Schematic illustrating the cloud variability effect. The bars on the C-axis denote the pdf of a simple form of variability, where the cloud cover attains only two values. The solid line illustrates a non-linear relationship between cloud cover and cloud radiative forcing, CRF. The bars on the CRF-axis give the pdf of the CRF resulting from the cloud distribution, and $\langle \text{CRF} \rangle$ shows the mean of this CRF distribution. $\langle C \rangle$ shows the mean of the cloud distribution and M shows the CRF of this value. Due to the non-linearity of the relationship, there is a difference, V, between $\langle \text{CRF} \rangle$ and M.

by the warming in Section 3.3, a non-linear function of cloud properties (Harshvardhan and Randall, 1985; Taylor and Ghan, 1992). As a consequence, the time-mean CRF is not the same as CRF by time-mean clouds:

$$\langle \text{CRF} \rangle \;=\; M(\langle C \rangle) \;+\; V(\langle C \rangle, C') \tag{4.1}$$

where the brackets represent a time average and primes deviations therefrom. C represents collectively cloud properties in an atmospheric column, M is the CRF due to time-mean clouds and V is a residual. This residual is the "variability contribution" to time-mean CRF and is, as illustrated in Figure 4.1 where the CRF is a non-linear function of C, generally non-zero. This term is the focus of the present chapter.

How large is V compared to M in the current climate? Perhaps more importantly, how large a contribution does V make to cloud feedback as climate changes? Reviewing the cloud feedback literature with these questions in mind brings to light a recurring inconsistency. There are two widely used methods to quantify cloud feedback, one employing offline radiative calculations (Wetherald and Manabe, 1988) and another (Cess and Potter, 1987; Cess et al., 1996) based on changes in CRF driven by surface temperature perturbations (see Soden

and/or time) clear-sky areas.

et al., 2004, for a discussion of the relative merits of the two methods). Cloud variability is automatically included in the CRF approach, while studies using the offline approach are careful to include the variability contribution by computing feedbacks as averages over a large ensemble of instantaneous radiative calculations (snap-shots). Thus, feedback values published in the literature all include contributions from both M and V. The situation is different, though, when it comes to interpreting radiative feedback in terms of cloud changes. In this case, studies typically relate cloud feedback to changes in mean cloud properties only (Wetherald and Manabe, 1988; Senior and Mitchell, 1993; Le Treut et al., 1994; Zhang et al., 1994; Colman et al., 2001). The implicit assumption that V is negligible can be misleading. For example, the developers of a GCM may decide that discrepancies between modeled and observed CRF are due to an excess (or deficit) of mean clouds in some region. They may then modify the cloud parameterization accordingly and achieve a good match with observations. But if much of the discrepancy was actually due to a misrepresentation of cloud variability, then the model will be getting the right answer for the wrong reasons – a common feature in current GCMs (Potter and Cess, 2004).

Some previous studies give an indication of the role played by V. Bergman and Salby (1997) used a single-column radiation model driven by observed cloud, temperature and humidity fields to diagnose the diurnal variability contribution to time-mean CRF, and found that it could be as large as 20 Wm^{-2}. Taylor and Ghan (1992), using an early version of NCAR's Community Climate Model (CCM1), compared a climate change experiment in which cloud liquid water path was held fixed to another in which it was allowed to vary in time. In both cases, clouds gave a negative (cooling) feedback to global warming, with cloud variability adding about 13% to this cooling. Using a GCM derived from the NCEP forecast model, Schneider et al. (1999) found that fixing cloud fraction and optical properties at their time-mean values led to a drop of up to 80 Wm^{-2} locally in absorbed insolation when compared to a reference run with interactive clouds. Conversely, a similar experiment using GENESIS2 (Vavrus, 2004) showed that fixing clouds led to a global warming of several degrees. These results show that V can be large and strongly model- or climate state-dependent, and motivate a more detailed analysis of its origin and nature.

This chapter is intended as an exploratory study, aimed at identifying key features of the problem and examining the methods that may be brought to bear on them. To ease interpretation of the results, we employ the usual idealized aquaplanet model configuration. In Section 4.1 we study the size of the variability contribution and find it to be large, accounting for over 1/3 of total CRF, while Section 4.2 deals with the mechanisms underlying the variability contribution. We find that the key non-linearity at play is introduced by the vertical cloud overlap parameterization.

4.1 Radiative impact

Here we perform a systematic assessment of the CRF change encountered in Section 3.3 due to fixing clouds. We describe a cloud resampling technique that we use to study the effect both in the reference climate and in a climate change experiment.

4.1.1 Methodology

Our usual setup of the CCM3 is used; no sea ice or seasons and aquaplanet lower boundary conditions. The horizontal resolution is T21, the solar constant is 1367 Wm^{-2} and the albedo is fixed uniformly at 0.11 to give a present-day-like climate when running the model with a 50 m mixed-layer ocean. We generated a reference climatology for this setup by setting the CO_2 concentration at 355 ppm and running the model until the SSTs had reached a statistically steady state (corresponding to that considered in Section 3.1).

To study the role of cloud variability in the reference run, we use an approach that is a hybrid between the above mentioned offline radiative calculation method and the CRF method. It may be summarized in a number of steps:

- We run the full GCM with SST fixed at the time-mean, zonal-mean value taken from the reference run and output cloud amounts and optical properties (liquid water path, effective radius and ice fraction) at 2 hour intervals for 200 days.

- We break the data down into time-mean and time-varying components: $C = \langle C \rangle + C'$, where C can represent any (or any combination) of the cloud parameters, and produce synthetic datasets with any desired amplitude of variability by scaling the variability component:

$$C_q = \langle C \rangle + q\,C'$$

  with q a number between 0 and 1. Note that $\langle C_q \rangle = \langle C \rangle$ for all choices of q.

- We then re-run the GCM, again with fixed SST, but we prescribe cloud properties by reading them from the synthetic dataset every 2 hours (linear interpolation is used for intermediate time steps). These runs are 2 years long, looping over and re-using the 200-day cloud dataset.

The sensitivity of time-mean CRF in these fixed-SST runs to changes in q gives a quantitative measure of the role played by cloud variability in maintaining the climate of the reference run. A caveat of this method is that in the reference run, where clouds are fully interactive, the cloud and thermodynamic fields are closely correlated; this correlation is lost when using the resampled cloud data, and this can bias the CRF response, particularly in the longwave (Schneider et al., 1999): With internally calculated clouds, cloudiness and humidity are

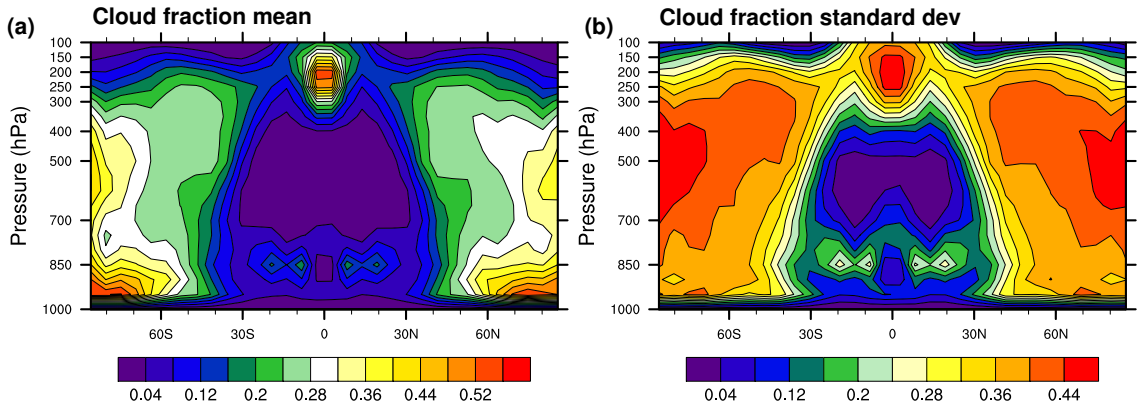

Figure 4.2: (a) Zonal-mean, time-mean cloud fraction and (b) zonal-mean standard deviation of cloud fraction in the reference run.

strongly correlated and this correlation is reduced when clouds are specified. Loss of longwave radiation to space is thus decreased in clear-sky situations due to larger humidity. In cloudy settings, however, a lower humidity will not increase the longwave flux since the opacity is already large due to the clouds. This leads to a net longwave warming.

A further bias will be introduced by the use of fixed SST, but we expect this to be small since there is actually little SST variability in the reference run. We can quantify the overall bias by comparing the time-mean CRF of the reference run and the resampled run using q=1. As shown in Section 4.1.2, the bias is very small (about 0.02 W m^{-2}) when compared to CRF changes induced by changing q. We thus feel confident that the method is accurate enough for the purposes of this study.

4.1.2 Reference climate

Here we apply the methodology of Section 4.1.1 to assess the role played by cloud variability in maintaining the climate of the reference run. For later reference, we first briefly examine some cloud statistics from the reference run. Figure 4.2(a) presents time- and zonal-mean cloud fraction. The pattern in this figure compares well with those from GCM simulations of the modern climate, indicating again that our idealized configuration is not in an unduly unrealistic regime. Cloud fraction variability (Figure 4.2(b)) roughly follows the same pattern, with maxima at the equatorial tropopause, the low-level subtropics and the mid-troposphere in high latitudes. Cloud liquid water path (Figure 4.3) shows a rather different pattern, with a large maximum in the time-mean at low levels over the equator, and a single, high-latitude variability maximum in each hemisphere.

The radiative impact of cloud variability is quantified in Figure 4.4(a). Time-mean clouds (q=0) give a global-mean CRF of about -14.5 Wm^{-2}. This cooling tendency increases with

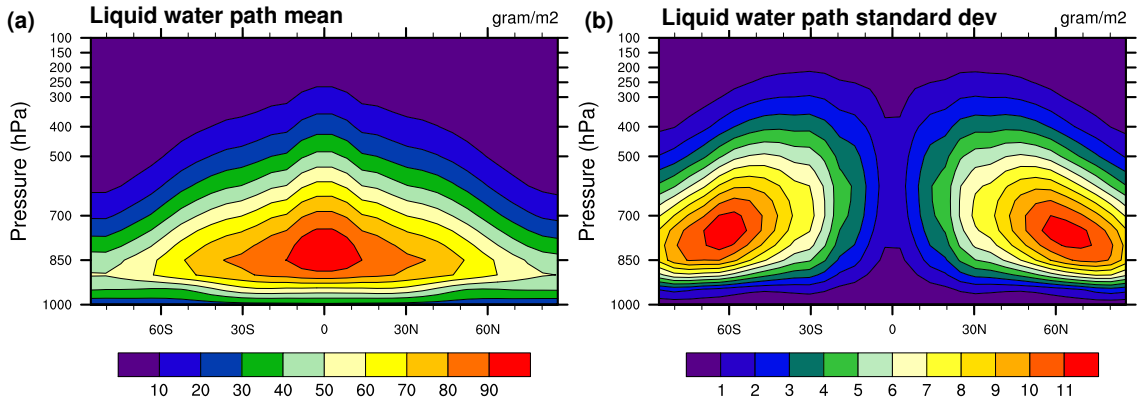

Figure 4.3: (a) Zonal-mean, time-mean cloud liquid water path and (b) zonal-mean standard deviation of cloud liquid water path in the reference run.

increasing q, reaching -22.11 Wm^{-2} when full cloud variability is used (q=1). The large crossed-circle symbol in the figure shows time- and global-mean CRF in the reference run, which has a value of about -22.13 Wm^{-2}. The difference between this value and the q=1 fixed-SST value gives a measure of the bias inherent in our method, which is clearly very small. We conclude that V, the variability contribution to CRF, plays a major role in the maintenance of the reference climate, accounting for about 8 Wm^{-2} or 35% of total CRF.

Figure 4.4(b) compares the spatial structure of CRF in the no-variability and full variability cases. The variability contribution is the difference between these two curves, which is shown in Figure 4.5(a). It is large in the tropical and subtropical regions: at 30° latitude the variability contribution actually accounts for *all* of the cloud forcing. In the mid- and high-latitudes, on the other hand, the variability contribution is very small. As shown in Figure 4.5(b), this is due to a cancellation between longwave and shortwave components, which are large but of opposite sign. This structure will become important when analyzing the role of cloud variability in climate change in the next section.

Figures 4.2 and 4.3 show substantial variability in both cloud amount and liquid water path. What is the relative contribution of each to total CRF? We address this question by conducting two further fixed-SST runs, one with fixed cloud fraction and full liquid water path variability, the other with these roles reversed. The two runs give a global-mean CRF of -14.8 and -22.7 Wm^{-2}, respectively. Comparing these values with those in Figure 4.4(a), we see that liquid water path variability plays a negligible role. Furthermore, separate examination of short- and longwave components of the liquid water path contribution (not shown) shows that they are both small, so this is not a case of cancellation between two large but opposite quantities. This implies that the radiative scheme in the model has an approximately linear response to liquid water path, at least over the range of values experienced in the present runs. Note, however, that a different cloud scheme or climate state may produce liquid water

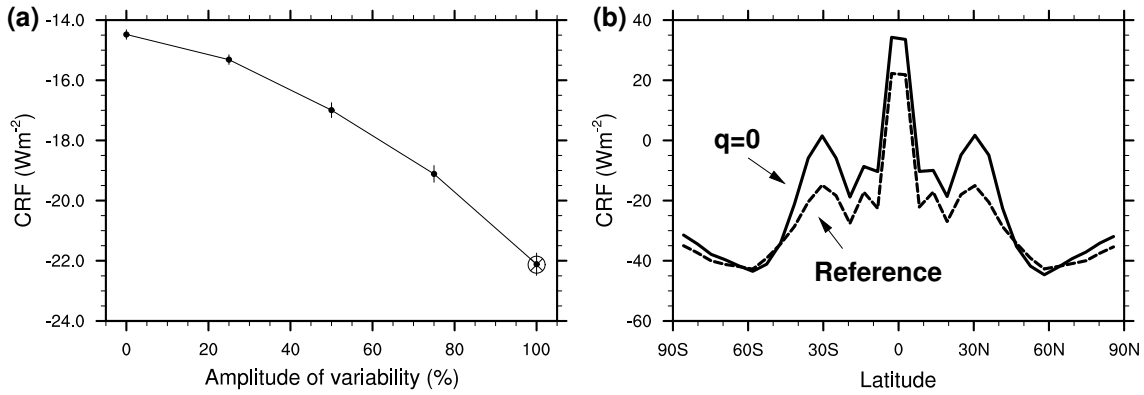

Figure 4.4: (a) Global average top-of-atmosphere CRF as function of scaling employed. Vertical bars denote one standard deviation over the two-year integration and the crossed-circle shows the case of internally calculated clouds. The $\sim$8 Wm^{-2} difference between $\sim$14 Wm^{-2} and $\sim$22 Wm^{-2} is the variability contribution, V. (b) Latitudinal structure of CRF with $q = 0$ (solid) and with internally calculated clouds (dashed).

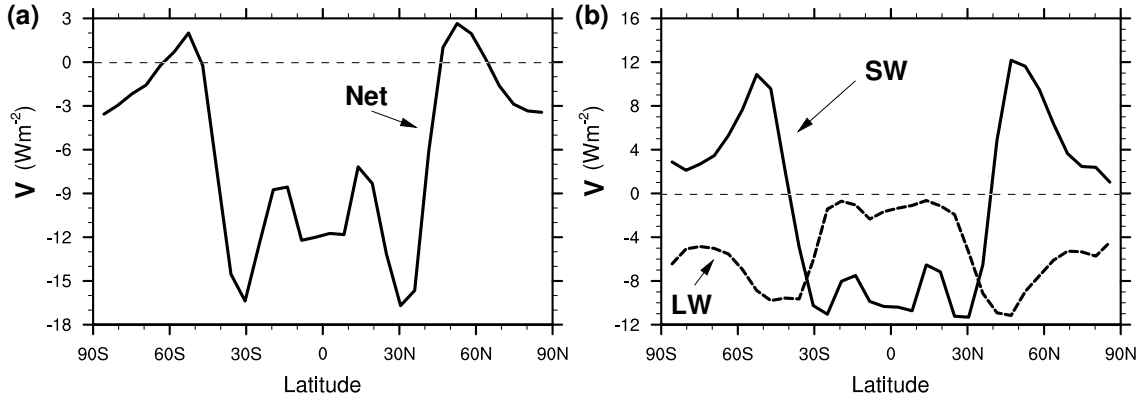

Figure 4.5: (a) Latitudinal structure of V in the reference run and (b) shortwave (solid) and longwave (dashed) contributions thereto.

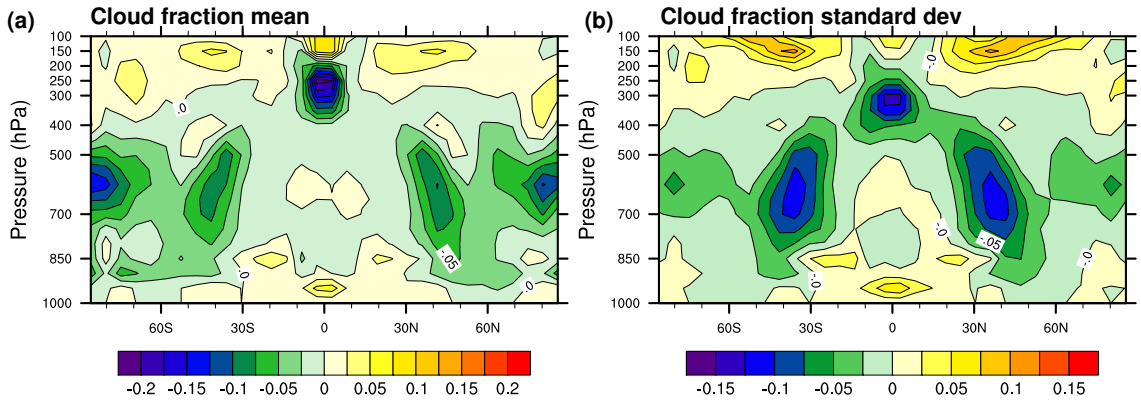

Figure 4.6: (a) Time- and zonal-mean change in cloud fraction due to quadrupling CO_2. (b) As in (a) but for standard deviation.

path values in a range where the response is non-linear, so this result may not be robust.

Given the tiny role played by liquid water path, we will not consider it further in this study. We examine the reasons for the large role of cloud fraction variability in Section 4.2.

4.1.3 Climate change

We saw above that a substantial part of the cloud forcing in the reference climate is due to cloud variability, and this forcing could be even larger were it not for a cancellation between the short- and longwave effects. How the forcing changes and whether such a cancellation continues to hold in a changed climate is not obvious. To address these issues, we perform a model integration identical in every respect to the reference run but employing quadrupled CO_2 concentration ("4×" run). This run has a global-mean SST about 5 K higher than the reference run, which results in an elevated tropopause and hence greater upper-level mean cloudiness and variability (Figure 4.6). There is also a poleward shift and slight weakening of the mid-latitude storm tracks, resulting in reduced mean cloudiness and variability in the lower troposphere, especially in mid-latitudes.

Our aim in this section is to assess the radiative impact of the cloud changes (mean state and variability) in Figure 4.6. To do this, we again employ the cloud resampling method of Section 4.1.1. We output cloud data at 2 hour intervals from the 4× run, and then perform fixed-SST runs with clouds specified by reading from this dataset. We emphasize that *all* fixed-SST runs here use SST and CO_2 values taken from the *reference* run. Thus, changes in CRF are due solely to changes in clouds and not in clear-sky radiation[2]. Our method is thus

[2]In fact, this is not quite true: since temperature and humidity are internally calculated in the fixed-SST runs, it can be argued that cloud changes may drive changes in these fields that will bias the clear-sky radiation. However, this caveat applies only to the longwave component, and considering the very strong control that

	Global	Trop	Ex-trop
$\Delta\langle\mathrm{CRF}\rangle$	1.82	-1.92	5.55
ΔM	3.06	-1.19	7.32
ΔV	-1.25	-0.73	-1.77

Table 4.1: Cloud radiative feedbacks (Eqs. (4.2)–(4.4)) averaged globally and over the tropics (30°S–30°N) and extratropics (90°S–30°S, 30°N–90°N). Units are Wm^{-2}.

closer to an offline radiation calculation than to the CRF approach of Cess and Potter (1987). Using the notation of eqn. (4.1), we may formalize this as

$$\Delta\langle\mathrm{CRF}\rangle = \langle\mathrm{CRF}_4\rangle - \langle\mathrm{CRF}_1\rangle \tag{4.2}$$

$$\Delta M = M_4 - M_1 \tag{4.3}$$

$$\Delta V = V_4 - V_1 = \Delta\langle\mathrm{CRF}\rangle - \Delta M, \tag{4.4}$$

where $\langle\mathrm{CRF}_4\rangle$ is time-mean CRF in the fixed-SST run employing fully-variable clouds (q=1) from the 4× run, while M_4 is the same quantity for the case with fixed clouds (q=0). Index 1 indicates analogous quantities using clouds from the reference run.

Results are shown in Figure 4.7 and summarized in Table 4.1. $\Delta\langle\mathrm{CRF}\rangle$ is weakly negative in the tropics and strongly positive in the extratropics, giving a global-mean warming of about 1.8 Wm^{-2}. The latitudinal structure of total cloud feedback contributes to polar amplification of surface warming (as also seen in Section 3.2). ΔM gives the dominant contribution, but ΔV also plays a significant role, offsetting much of the warming due to ΔM in the midlatitudes. Globally, ΔV cancels 40% of ΔM, in line with the 35% contribution to total CRF given by V in the reference run (Section 4.1.2).

We can qualitatively account for the observed structure of ΔM (detailed in Figure 4.7(b)) in terms of the changes in mean cloud fraction in Figure 4.6(a). At the equator, the minimum in ΔM stems from a longwave cooling tendency (Figure 4.7(b)). Figure 4.6(a) shows that a deeper convection in the ITCZ has lead to an upward shift of the high-level cloudiness. This would lead to a warming effect, but in addition to the shift there is also a general decrease in high-level clouds which is responsible for the longwave cooling. At 20° latitude there is an increase in cloudiness both in the upper and lower tropospheric layers. This leads to enhanced cloud albedo and thus shortwave cooling, partially offset by a longwave warming. At 40° latitude a large decrease in the mid-level clouds leads to a large increase in the absorbed shortwave and thus a warming tendency. At high latitudes, Figure 4.6(a) shows an upward shift of the cloud distribution with little change in vertical-mean cloud amount; this gives a

SST exerts on the climate, we expect the resulting bias to be small, on the order of the bias introduced by cloud decorrelation.

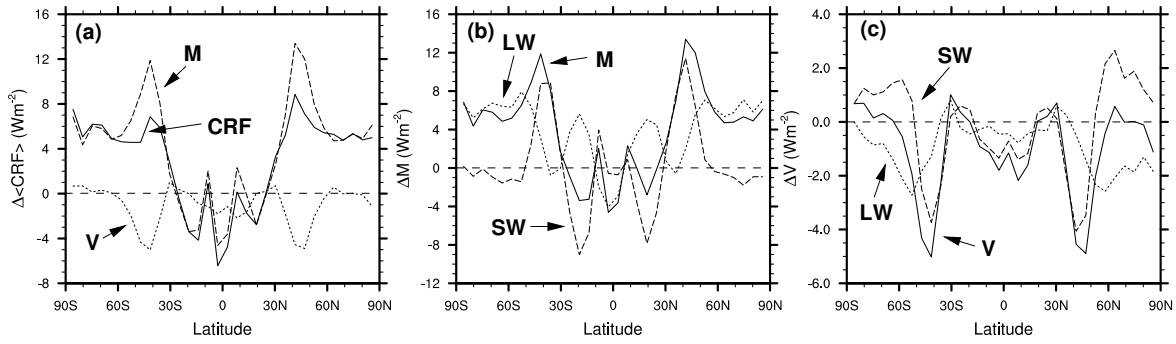

Figure 4.7: (a) Cloud radiative feedbacks in the 4× run: $\Delta\langle\text{CRF}\rangle$ (solid), ΔM (dashed) and ΔV (dotted). The total change is seen to be made up mainly of the ΔM contribution, but at mid-latitudes ΔV has a significant offsetting effect. (b) ΔM (solid) and its breakdown into shortwave (dashed) and longwave (dotted) contributions. (c) As in (b) but for ΔV.

longwave warming with little effect on the shortwave.

We cannot at this point perform a similar analysis for ΔV because we lack a simple, qualitative picture of the relation between cloud variability and CRF. We investigate aspects of this picture in the following section.

4.2 Role of cloud variability

Having in the previous section determined the impact of cloud variability on the CRF in both the reference climate and in a climate change experiment we now investigate the mechanisms underlying this variability contribution. We approach the problem by first identifying leading modes of cloud variability and then assessing their effects on CRF.

4.2.1 Patterns of cloud variability

Given the plane-parallel assumption made in the model's radiative scheme we take a column-by-column approach to studying the variability patterns of the cloud fraction field in the reference climate. We select two latitudes, 30° and 50°, representative of cases with large and small V, respectively (Figure 4.5).

We employ canonical correlation analysis (CCA) to identify the modes of cloud variability that most strongly affect top-of-atmosphere radiation. CCA analyzes the joint variability of two fields (von Storch and Zwiers, 1999) and the technique extracts pairs of patterns where the correlation between the pattern coefficients is maximized. The two fields used here are cloud amount and a vector with long- and shortwave CRF as its first and second components. We do not study cloud liquid water path variability since its effect was shown to be small in Section 4.1.2. The zonal symmetry of our model setup means that any longitude point can be used for the analysis. We use 200 days of 2-hourly column cloudiness and CRF.

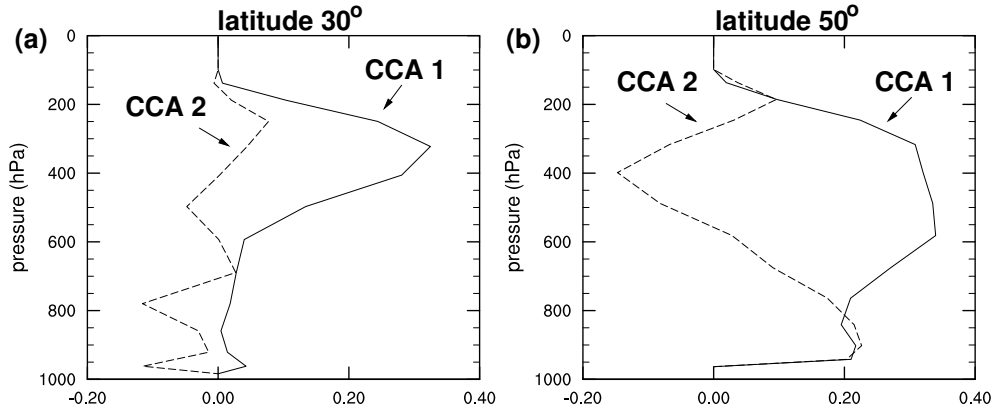

Figure 4.8: First (solid) and second (dashed) cloud CCA patterns obtained from cloud and CRF variability at (a) 30° and (b) 50°. At both latitudes, the leading CCA accounts for about 40% of the variance and describes column-wide in-phase variability.

Results are shown in Figure 4.8. The CCA patterns have physical units and show both the structure and magnitude of "typical" anomalies associated with the joint mode of variability. At 30° latitude, the leading pattern of cloud fraction variability has a single sign throughout the column but is strongly peaked in the upper troposphere (not surprisingly, in view of Figure 4.2(b)). It explains 42% of the cloud variance and corresponds to a flux pattern (LW, SW)=$(-38.13, -31.52)$ Wm^{-2}. The second mode has a more complex structure, projects mainly on the shortwave flux component and accounts for only 6% of cloud variance. At 50° latitude, the leading pattern is again single signed, but affects a much deeper layer of the troposphere. It explains 39% of cloud variance and corresponds to a flux pattern of $(-33.83, -37.88)$ Wm^{-2}. The second mode accounts for 12% of cloud variance and again projects mostly on the shortwave.

In summary, a large portion of CRF variability at both latitudes is driven by vertically coherent, in-phase cloud amount fluctuations, with subtropical fluctuations confined to upper levels and nearly troposphere-filling fluctuations in mid-latitudes. The very strong correlation between the leading cloud pattern and CRF at the subtropical location is readily apparent in Figure 4.9 showing 60 days of the short- and longwave CRFs along with the coefficient of the leading pattern. There is also a hint of the non-linearity in the relationship (compare, for instance, the relative strengths of the cloud amplitude peaks at days 6 and 10 with the corresponding peaks in longwave CRF). Note also the rather intermittent nature of the subtropical cloud variability, with much time spent in a virtually cloud-free base state interspersed with large, rapid excursions to cloudy, often almost overcast states. It would be interesting to ascertain the physical origin of this behavior (perhaps intermittent convection, or advective intrusions from other latitudes), but that would take us outside the scope of this chapter.

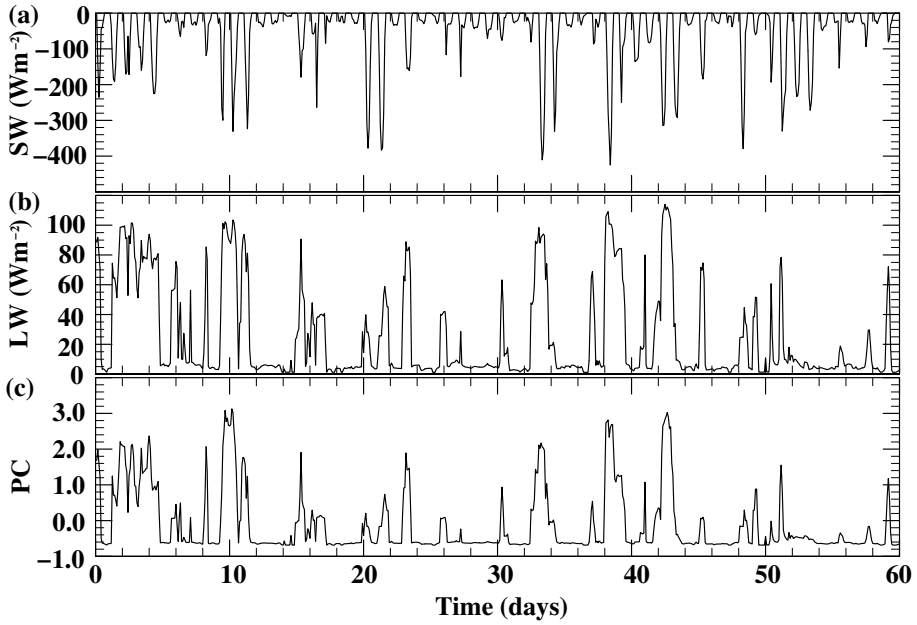

Figure 4.9: Time series of (a) shortwave CRF, (b) longwave CRF and (c) pattern coefficient corresponding to the first CCA pattern at 30° latitude. The pattern coefficient is normalized to unit standard deviation.

4.2.2 In-phase cloud variability

Here we investigate the consequences for vertically integrated total time-mean cloud cover of the in-phase variability throughout the column. We prove by induction that using the random-overlap assumption, fixed clouds give a greater total cloud cover than a situation where the cloudiness in all the layers varies in phase. First, we will consider the method of calculating the vertically integrated cloudiness.

The principle is most readily understood in terms of probabilities. The cloud fraction, c_i, of the ith level can be thought of in two ways: 1) as the fraction of the sky covered by clouds when looking up or 2) as the probability of there being a cloud directly overhead. The latter of these views will be employed in the following.

Take, as an example, a two-layer atmosphere with cloud fractions c_1 and c_2 in the two layers, respectively. The probability of having a cloud overhead in layer 1 (event CLD_1) is $P(CLD_1) = c_1$ while the complement event, CLD_1^C (clear sky overhead), has probability $P(CLD_1^c) = 1 - c_1$. The same applies for layer 2 and we can now calculate the vertically integrated cloud fraction as the probability of there being a cloud overhead in layer 1 *or* layer

2:

$$\begin{aligned} P(CLD_{12}) &= P(CLD_1 \cup CLD_2) \\ &= 1 - P(CLD_1^C \cap CLD_2^C) \\ &= 1 - [(1-c_1)(1-c_2)], \end{aligned}$$

where the last term is the probability of having clear sky overhead. Here we have assumed the cloud covers in the two layers to be independent – this is the basic (and rather unphysical) assumption of the random-overlap scheme first proposed by Manabe and Strickler (1964). The model can now be extended to an arbitrary number, N, of levels in the vertical, and the above formula readily generalizes to

$$P(CLD_{1\to N}) = 1 - \prod_{i=1}^{N}(1-c_i). \tag{4.5}$$

We will now prove that fixing the clouds increases this value relative to a situation where the cloudinesses vary in phase. By "in phase", we mean specifically that the sign of the layer cloudinesses relative to their respective mean values always are the same. In the proof we will consider the clear-sky fraction (CSF), $x_i \equiv 1 - c_i$, of each layer. To begin with we introduce some definitions and some notation:

- The CSF of each layer can be split into a mean value and a deviation from this mean which averages to zero: $x_i = \langle x_i \rangle + x_i'$. When in phase, it is the signs of the "x_i'"s that follow each other.

- $x_{\hat{n}} = \prod_{i=1}^{n} x_i$ is the time dependent, vertically integrated CSF over layers 1 through n (cf. eqn. (4.5)).

- $\langle \cdot \rangle$ denotes time-averaging

- $\langle x_{\hat{n}} \rangle^* = \prod_{i=1}^{n} \langle x_i \rangle$ is, according to eqn. (4.5), the time-averaged, vertically integrated CSF of a fixed-cloud scenario.

Our task is thus to prove that

$$\left\langle \prod_{i=1}^{N} x_i \right\rangle \geq \prod_{i=1}^{N} \langle x_i \rangle$$

or equivalently

$$\langle x_{\hat{N}} \rangle \geq \langle x_{\hat{N}} \rangle^*$$

for any number of layers, N. Our proof by induction involves the following two induction hypotheses:

(1) The CSF of a collection of layers, 1 through n, can be written

$$x_{\hat{n}} = \langle x_{\hat{n}} \rangle^* + \tilde{x}_{\hat{n}},$$

where $\tilde{x}_{\hat{n}}$ varies in the phase of all the individual layers, i.e., the sign of $\tilde{x}_{\hat{n}}$ is the same as the sign of the individual layer cloudinesses relative to their respective mean values.

(2) The time-average of $\tilde{x}_{\hat{n}}$ satisfies

$$\langle \tilde{x}_{\hat{n}} \rangle \geq 0,$$

or $\langle x_{\hat{n}} \rangle \geq \langle x_{\hat{n}} \rangle^*$, which is the point of the proof.

Base case: Let $n = 1$. We can trivially write

$$x_{\hat{1}} = \langle x_{\hat{1}} \rangle^* + \tilde{x}_{\hat{1}} = \langle x_1 \rangle + x'_1,$$

and assumptions (1) and (2) are clearly satisfied since $\langle x'_1 \rangle = 0$.
Induction Step: (1) and (2) are assumed to hold for n layers. We thus have a collection of layers with the vertically integrated CSF $x_{\hat{n}} = \langle x_{\hat{n}} \rangle^* + \tilde{x}_{\hat{n}}$. Consider the effect of adding another layer, $x_{n+1} = \langle x_{n+1} \rangle + x'_{n+1}$, varying in phase with the others. The product of the two CSF's is

$$\begin{aligned} x_{\widehat{n+1}} &= \left(\langle x_{\hat{n}} \rangle^* + \tilde{x}_{\hat{n}}\right)\left(\langle x_{n+1} \rangle + x'_{n+1}\right) \\ &= \langle x_{\widehat{n+1}} \rangle^* + \langle x_{n+1} \rangle \tilde{x}_{\hat{n}} + x'_{n+1}\tilde{x}_{\hat{n}} + \langle x_{\hat{n}} \rangle^* x'_{n+1} \\ &= \langle x_{\widehat{n+1}} \rangle^* + \tilde{x}_{\hat{n}} x_{n+1} + \langle x_{\hat{n}} \rangle^* x'_{n+1} \\ &= \langle x_{\widehat{n+1}} \rangle^* + \tilde{x}_{\widehat{n+1}}, \end{aligned}$$

where $\tilde{x}_{\widehat{n+1}} \equiv \tilde{x}_{\hat{n}} x_{n+1} + \langle x_{\hat{n}} \rangle^* x'_{n+1}$ varies in phase with all layers since $x_{n+1} \geq 0$, $\langle x_{\hat{n}} \rangle^* \geq 0$ and $\tilde{x}_{\hat{n}}$ and x'_{n+1} are in the correct phase. Thus (1) is satisfied. Now use the second line of the above equation to calculate the time-average:

$$\begin{aligned} \langle x_{\widehat{n+1}} \rangle &= \langle x_{\widehat{n+1}} \rangle^* + \langle x_{n+1} \rangle \langle \tilde{x}_{\hat{n}} \rangle \\ &\quad + \langle x'_{n+1}\tilde{x}_{\hat{n}} \rangle + \langle x_{\hat{n}} \rangle^* \langle x'_{n+1} \rangle \\ &= \langle x_{\widehat{n+1}} \rangle^* + \langle x_{n+1} \rangle \langle \tilde{x}_{\hat{n}} \rangle + \langle x'_{n+1}\tilde{x}_{\hat{n}} \rangle \\ &\geq \langle x_{\widehat{n+1}} \rangle^*, \end{aligned}$$

since $\langle x_{n+1} \rangle \geq 0$, $\langle \tilde{x}_{\hat{n}} \rangle \geq 0$ (by (2)) and $\langle x'_{n+1}\tilde{x}_{\hat{n}} \rangle \geq 0$ due to the equal phase. Thus (2) is also satisfied and the proof is complete. Note that this only holds in the case of randomly overlapped clouds. In the more recent versions, CAM2 and CAM3, of the model (and in many other modern models) a so-called maximum-random overlap assumption is employed. In that case, clouds in adjacent layers are assumed to be maximally overlapped, while such chunks of

layers are assumed to be randomly overlapped. The physical reasoning is that if two adjacent layers have clouds, they are most likely due to the same process and are therefore also co-located. If intermediate cloud free layers exist, the chunks are likely to be due to different processes and random overlap is again assumed. With this scheme, the above proof does not hold, but it seems likely that a similar effect will exist between the randomly overlapped chunks.

Having earlier found the leading patterns of cloud variability to describe column-wide in-phase variability, we can thus conclude that, in this model, the cloud variability tends to decrease the vertically integrated time-mean cloud cover. The consequences of this for the longwave CRF will be discussed next. We argue that the key non-linearity at play is exactly in the cloud overlap scheme.

4.2.3 Longwave effects

The radiation code used in CCM3.6 employs for the longwave calculation the random vertical overlap scheme described in the previous subsection (Kiehl et al., 1996). The product term in eqn. (4.5) introduces an obvious non-linearity which, as we saw, makes itself felt when cloud fraction varies in time. As a simple example, consider the case with only two cloudy layers. With cloud fraction constant at 0.5 in both layers, total cloudiness is $1 - (1 - 0.5)^2 = 0.75$. If instead the two layers vary in phase, with cloud fraction of 0 half the time and 1 the rest of the time, the time-mean total cloud cover is decreased to 0.5 without changing the mean value in each layer. Conversely, if the same variability is used in anti-phase the total cloud cover increases to 1.

Thus, we expect in-phase cloud fraction variability (as found in the leading CCA modes above) to reduce total cloud cover and thus weaken the overall cloud greenhouse effect. In other words, we expect a negative contribution to longwave CRF. To show that this actually happens, we use a single-column version of the CCM3.6 radiative scheme[3] to perform experiments along the lines of the simple example above. For simplicity, we use a moist adiabatic temperature profile and vertically uniform relative humidity (qualitative results are not affected by this choice). The model has a total of 18 equispaced pressure levels. We specify a "cloud deck" within the model as a contiguous block of cloudy layers. Liquid water path in each layer is fixed at 15 g m^{-2}. For a specified cloud deck, we compute longwave CRF with layer-wise cloud fraction fixed at 0.5 (which gives M), and compare this with the time-mean CRF when cloud fraction spends half its time at 0 and the other half at 1 (which gives V). We repeat the experiment changing the cloud deck's vertical extent and position.

The resulting values of V are displayed in Figure 4.10(a). As expected, they are all negative. Since total cloud cover depends on a product over all cloudy layers, the magnitude of

[3]The single column model is part of CliMT, a Python-based climate modeling and diagnostics toolkit maintained by Rodrigo Caballero and freely available at http://geosci.uchicago.edu/~rca/climt.

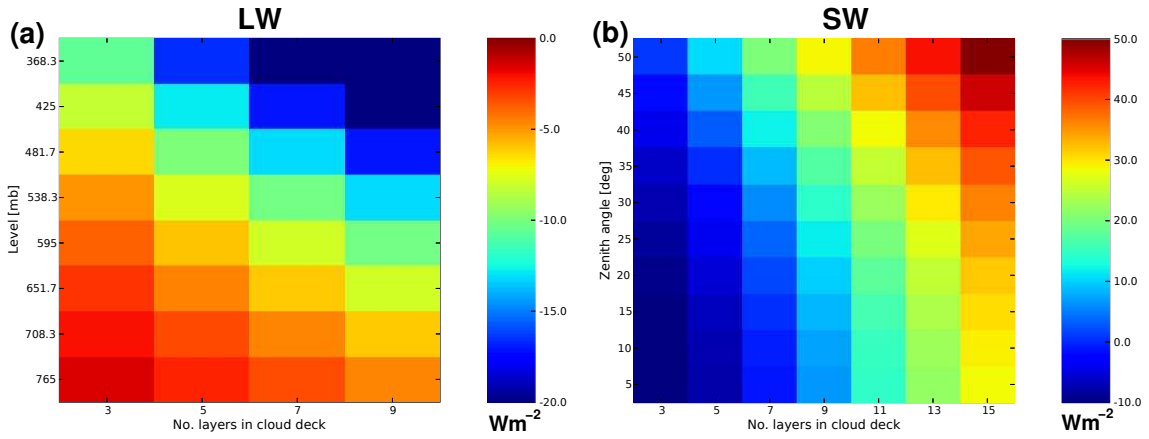

Figure 4.10: Sensitivity of the variability contribution V to time-mean longwave (a) and shortwave (b) CRF in the single-column radiative model. Units are Wm^{-2}. See text for details.

V grows with the number of layers in the deck. V also increases with deck height, since a cloud near the surface emits at a temperature not too different from the ground's and so its greenhouse effect is weak. Though not shown here, V also increases strongly as liquid water path in each layer increases.

Using these results, we can qualitatively account for some features of V found in earlier sections. Consider the longwave component of V in the reference climate (dashed line in Figure 4.5(b)). This is everywhere negative, as expected. It is weak in the tropics, since cloud variability occurs in a thin layer near the tropopause, where liquid water path is very small (Figure 4.3). In the mid and high latitudes, variability fills a thicker layer of the troposphere, leading to higher V values; the midlatitude maximum is attributable to the high liquid water path there. Turning to the change in longwave V due to quadrupling CO_2, we see (Figure 4.7(c)) that it is everywhere negative, which we may interpret as resulting from the overall upward shift of cloud variability (Figure 4.6). The change is greatest around 50–60° latitude, where strong upper-level increase in cloud variability is accompanied by weak low-level decrease.

4.2.4 Shortwave effects

The situation is somewhat more complex for shortwave radiation. This part of CCM3.6's radiative scheme parameterizes vertical cloud overlap using a scaling method due to Briegleb (1992) (see also Stephens et al., 2004). In this approach, each cloudy layer is treated as overcast, but its extinction optical depth τ is scaled by cloud fraction to the power 3/2,

$$\tau' = \tau c^{3/2}. \tag{4.6}$$

Briegleb (1992) found this to give a good match to the computationally more expensive random overlap method.

Let us consider the effect of this scheme on radiative transfer in the presence of fluctuating cloud fraction. For simplicity, we consider only direct-beam transmission (we show a posteriori using the single-column radiative model that this is enough to capture the qualitative features of the problem). The cloud contribution to direct-beam transmission, T_i, in the ith layer is given by

$$T_i = \exp\left(-\frac{\tau_i'}{\mu_0}\right), \tag{4.7}$$

where τ_i' is the modified cloud extinction optical depth of the layer and μ_0 is the cosine of the zenith angle. The transmission of the entire column is the product of these single-layer transmissions

$$T = \prod_{i=1}^{N} \exp\left(-\frac{\tau_i'}{\mu_0}\right), \tag{4.8}$$

where N is the number of cloudy layers.

Consider first the simpler case where we replace the exponent in eqn. (4.6) by 1. Then if both optical depth and cloud fraction are uniform at τ_0 and c_0, respectively, the total transmission becomes

$$T_0 = \exp\left(-\frac{N c_0 \tau_0}{\mu_0}\right). \tag{4.9}$$

Compare this with the case when cloud fraction fluctuates in a simple manner: half of the time all layers have cloud fraction $c_0 + \delta c$ and the other half of the time they have the cloud fraction $c_0 - \delta c$. The resulting time-mean transmission is

$$\langle T \rangle \;=\; T_0 \cosh\left(\frac{N \delta c\, \tau_0}{\mu_0}\right), \tag{4.10}$$

with T_0 as in eqn. (4.9). Since $\cosh x \geq 1$ for all x, $T_0 \leq \langle T \rangle$ for all δc. Cloud variability thus leads to increased transmission and thus a warming shortwave effect. Note that, as in the longwave case, this result only holds for in-phase variability.

If we instead use the original scaling formulation, eqn. (4.6), our constant cloudiness atmosphere has the time-mean transmission

$$T_0 = \exp\left(-\frac{N c_0^{3/2} \tau_0}{\mu_0}\right), \tag{4.11}$$

and the atmosphere with the simple variability has the transmission

$$\langle T \rangle \simeq T_0 \cosh\left(\frac{3}{2}\frac{N\tau_0}{\mu_0}\delta c\sqrt{c_0}\right)\exp\left(-\frac{3}{8}\frac{N\tau_0}{\mu_0}\frac{\delta c^2}{\sqrt{c_0}}\right), \tag{4.12}$$

which results from a second order Taylor expansion in δc. It is not obvious in this case whether the term multiplying T_0 on the right hand side of eqn. (4.12) is greater or less than unity for non-vanishing δc. However, the derivative of this coefficient with respect to δc can (with another Taylor expansion) be shown to be negative for

$$\frac{N c_0^{3/2}\tau_0}{\mu_0} < \frac{1}{3}, \tag{4.13}$$

and the criterion for the variability to yield a cooling effect thus becomes one on the mean state of the atmosphere (eqn. (4.11)). In a high-transmission mean atmosphere (e.g. one with little cloudiness or small zenith angle) variability will give shortwave cooling; conversely, variability in a low-transmission mean atmosphere will lead to warming.

To confirm the results of these analytical considerations, we perform a single-column radiative model sensitivity analysis analogous to that described above but this time focusing on the shortwave. Eqn. (4.13) indicates that N, μ_0, c_0 and τ_0 are all important parameters; we focus on the first two. Insolation is fixed at 400 W m^{-2} and the study is otherwise identical to the longwave case discussed above. Results are shown in Figure 4.10(b), where we see that for large N and small μ_0 (i.e. in a low-transmission mean state) the variability effect gives a strong warming. In the opposite extreme, the effect is a cooling. This is consistent with the predictions of the analytical treatment above.

These results explain the general appearance of the shortwave V curve in the reference run (solid line in Figure 4.5(b)). The low latitudes, which have few cloudy layers and small zenith angles, experience a cooling effect; the mid- and high latitudes, with more cloudy layers and larger zenith angles, experience a warming. The warming effect weakens with latitude due to decreasing liquid water path. In the climate change experiment (Figure 4.7(c)), shortwave V shows a dominant negative peak centered around 40–50° due to poleward expansion of that low-latitude variability pattern, which leads to mid-latitude cooling.

4.3 Conclusions

We have investigated the impact of cloud variability on the top-of-atmosphere radiative budget of the CCM3, run in our idealized aquaplanet configuration with no seasonality. Using a cloud resampling method (Section 4.1.1), we found that cloud variability accounts for 35% of global-mean CRF in the model's reference climate and 40% of the cloud radiative feedback attendant to a fourfold increase in CO_2 concentration. We found the correlation effect between clouds and water vapor (as discussed by Schneider et al., 1999) to be very small. We also found that

almost all of the variability contribution to CRF came from variability in cloud fraction rather than optical properties. Canonical correlation analysis of cloud fraction variability at 30° and 50° latitude showed the leading patterns to have a single sign throughout the troposphere. We showed that the random overlap assumption made in the model's longwave radiative scheme translates this variability into a time-mean cooling, while the scaling scheme used in the shortwave computation can produce either a warming or a cooling, depending on the time-mean state of the atmosphere. These findings allowed us to qualitatively account for the spatial structure of the variability contribution to CRF both in the reference run and in the climate change experiment.

Recent intercomparison studies show that cloud radiative impact is very sensitive to the details of overlap parameterization (Barker et al., 2003; Stephens et al., 2004). Our results present a concrete example of the subtle way in which this parameterization can affect the climate as a whole. They imply that a consideration of these effects is a necessary element in the evaluation of any GCM. Moreover, they stress the fact that a specification of clouds intended to eliminate the cloud feedback should be done in a time-varying snap-shot manner. Finally, when interpreting the cloud feedback, one should consider the effects of changes in the mean and the variability separately. The full change in CRF cannot a priori be ascribed to the change in the mean alone.

Chapter 5

Conclusion

This thesis has focused on the polar amplification of surface temperature change seen in numerous modeling experiments of climate warming. In particular, mechanisms unrelated to the ice-albedo feedback have been studied in GCM experiments carried out with the Community Climate Model ver 3 developed at the National Center for Atmospheric Research. The GCM was used in various idealized configurations, typically without continents and seasonal cycle. Surface albedo feedbacks were suppressed by excluding sea ice and specifying the surface albedo at a fixed uniform value. Experiments were performed both with fixed sea surface temperatures and a mixed-layer ocean model.

Results are presented in the next section followed by a discussion of the questions that the thesis leaves unanswered and possible directions of future research.

5.1 Summary and discussions

The simplified setup of the model gives it some similarities with the simple EBMs, such as zonal and hemispheric symmetry as well as time-constancy of the forcing. The detailed treatment of dynamics and physics are, however, retained in the model and Chapter 2 was therefore devoted to investigations of these similarities and differences. We found that

- The widely used linear Budyko-Sellers parameterization of the OLR in terms of the local SST holds reasonably well at high-latitudes in clear-sky settings. Clouds tend to have a shielding effect and thus reduce the sensitivity relative to the clear-sky value. At low latitudes, there is a much less direct relationship between the surface state and the TOA radiation. The OLR is heavily influenced by the moisture field which is controlled by the large scale circulation. Hence, low-latitude OLR changes are controlled mainly by the manner in which the surface temperature perturbation alters the Hadley cell structure and the position of the ITCZ rather than the local temperature change. Odd-order Legendre polynomial SST perturbations were seen to shift the ITCZ, the Hadley cells and the relative humidity field while even-order perturbations were found

to alter the strength of the circulation. Both effects have dominant influence on the OLR change, but in general, large-scale, even-order perturbations cause less problems than do small-scale, odd-order perturbations.

- The fact that the classical parameterization works best at high latitudes is fortunate, since this is where focus of most EBM studies (of, for example, the ice-albedo feedback) has been. A possible alternative to the local relationship is a matrix approach to the linear parameterization. With temperatures and the OLR represented in terms of spherical harmonics, a matrix may be constructed giving one in terms of the other. This is still a linear (and therefore computationally efficient) parameterization, but it respects the inherent non-locality of the relationship between the two quantities.

- When a thermodynamic sea ice model is included in the simple setting, the model displays multiple equilibria reminiscent of those seen in EBMs. A warm, ice-free state and a cold state with a large ice-cover were found for wide ranges of the tunable oceanic heat flux strength. For a narrower range of this parameter, a more present-day-like state was found. When seasons were included and when resolution was doubled (from T21 to T42) the warm and cold states survived, while the intermediate state was not found. Moreover, asymmetric climates were also possible, but only those combinations involving the warm and the cold state were allowed. Apparently, the intermediate climate is only marginally stable, while the two other states are very robust. This contrasts the situation in EBMs, where the present-day-climate is stable and the icy climate is unstable. It is not obvious, however, whether the cold state in the GCM corresponds to the present-day state in the EBM, whether the added detail in the GCM has reversed the stability characteristics, or whether such an identification is at all well-posed.

- Inclusion of a very simple continent had the effect of destabilizing the warm state by providing the necessary zonal asymmetry for standing waves to occur. This allowed for sea ice in localized parts of the ocean which could serve as seeds for larger-scale ice-advance. The zonal asymmetry also allowed for a more gradual retreat of the ice cover in the cold state, and the multiple equilibria stand out as a much less robust feature when the continent is included. It was concluded that the zonally symmetric setup has a profound influence on the model behavior when the sharp non-linearity of the ice-albedo feedback is included.

In Chapter 3, sea ice was again excluded and focus was on the polar amplification produced by the model in response both to ghost forcings of the surface budget and to CO_2 changes. Three different substudies were performed and it was found that

- Two ways of determining the linear stability and sensitivity properties of the system led to consistent results. It was possible to use the fluctuation-dissipation theorem to extract this information simply by observing the system's unforced variability – in a very

long run. Polar amplification was seen as a prominent feature of the linear dynamics; low-frequency fluctuations as well as the response to a uniform forcing displayed the polar amplification pattern.

- When a ghost forcing was applied to the surface budget in the tropics, in the extra-tropics and over the whole globe, the response was found to be linear, i.e., the response to the latter equals the sum of the responses to the two former. The response to the extra-tropical forcing was centered mainly at high latitudes while the tropical forcing gave a nearly globally uniform response. The polar amplification can therefore be viewed as a superposition of a global response to low-latitude forcing and a local response to high-latitude forcing.

- Using fixed, localized SST perturbations, we investigated the mechanism by which the low-latitude forcing is mediated to higher latitudes. A tropical temperature increase leads to an intensification of the meridional transport of heat and water vapor. This tends to warm and moisten the mid- to upper troposphere at high-latitudes. In fact, a tropical SST perturbation has larger impact on the polar atmosphere above 750 hPa than does a local perturbation. This, in turn, leads to an increased longwave forcing on the high-latitude surface. In producing this increased flux, off-line radiation calculations showed the tropospheric warming to dominate over the moistening.

- This effect is part of the conceptual mechanism we propose for the polar amplification based on our EBM experiments. We modified the formulation of the EBM such that the meridional heat transport increases not only with equator-to-pole temperature gradient but also with global mean temperature. This mimics the increased latent heat transport in a warmer and moister atmosphere, and leads to an exclusion of uniform (or equatorially amplified) responses to a uniform forcing: A uniform warming increases the meridional heat transport and the high latitudes must warm more to counter the added heat input. Either by intensified radiation to space or by weakening of the heat transport by a reduced temperature gradient – or both.

  This way of producing the final response may mask the underlying mechanism to an investigator comparing just the two equilibria (e.g, $1\times CO_2$ and $2\times CO_2$); when the final equilibrium is approached, the decreased temperature gradient may have countered the initial increase in heat transport. In fact, the two $4\times CO_2$ experiments performed in Section 3.3 both saw slight increases in equilibrium poleward heat transport, even though one displayed polar amplification and the other equatorial amplification. In the $2\times CO_2$ experiment by Boer (1995), a clear polar amplification was seen without any significant changes in net meridional heat transport. It would be difficult to determine whether the polar warming had been amplified by looking at the heat transport alone, and the type of experiments we have performed here seem best suited for diagnosing

the reason for polar amplification.

- The tendency for the meridional heat transport to amplify the polar response is augmented by the differences in the surface budget sensitivities. Probably due to the Clausius-Clapeyron relation, the low-latitude surface budget responds more strongly to a 1 K temperature perturbation than does the high-latitude budget. This implies that the low-latitude surface needs to warm less to counter an imposed forcing.

- The above mechanism does not necessarily carry over to other climate states. Due to an increase in static stability and a poleward migration of the storm tracks with global mean temperature, the meridional heat transport was found to become insensitive to T_m for $T_m > 15°\mathrm{C}$ and $\Delta T < 30°\mathrm{C}$. In this regime, further increases in the mean temperature no longer lead to increases in heat transport and the above polar amplifier ceases to operate. This implies that, if the results obtained here are to be taken at face value, meridional atmospheric heat transport cannot be used to explain the shallow equator-to-pole temperature gradients believed to have prevailed during the early Cenozoic.

In Sections 3.2 and 3.3, clouds were seen to play a role in determining both the global mean temperature and the meridional gradient. In particular, the climate was seen to warm when clouds were fixed at their time-mean value. The consequences of this for climate change experiments were explored in Chapter 4 where it was found that

- In the CCM3, cloud variability has a net cooling effect in the global mean relative to the situation where clouds are fixed at their time-mean value. This stems from a large shortwave cooling effect at low latitudes. At higher latitudes, a shortwave warming is countered by a longwave cooling. In-phase variability, which is the dominant pattern, was shown to lead to an increase in the time-mean total cloud cover and therefore a longwave cooling. For the shortwave, a special scaling parameterization of overlap effects was shown to give the low-latitude cooling and the high-latitude warming.

- The net change in cloud radiative forcing resulting from a quadrupling of CO_2 was found to be positive at high latitudes and negative at low latitudes, and thus to enhance the polar amplification (as also observed in Figure 3.10(b)). This effect consists mainly of a contribution from the change in the mean clouds, modified in mid-latitudes by the effects of a change in variability.

- Although the cloud scheme employed in this model is too outdated to allow for general conclusions about the workings of the real climate system, our results definitely point to certain pitfalls in this kind of model investigation. They stress the (well known) fact that time-varying cloud cover should be considered when "fixing clouds" to eliminate cloud feedback. Moreover, it is demonstrated that when interpreting cloud feedback, one cannot just compare the change in net CRF to the change in mean clouds. The change in variability needs to be considered as part of the feedback.

5.2 Outlook and future research

Not all good ideas (or bad ones) can be pursued. Sometimes an idea occurs long after new projects have been started and other times ideas are put aside since others seem more urgent or promising. Several lines of investigations therefore follow directly from the conclusions and findings presented here. Among these are the following

- It would be interesting to see how an EBM employing the proposed matrix parameterization of the OLR would behave. Would it be stable? How would its solution structure compare with that of the classical EBMs and that found here?

- The FDT method for evaluating a system's linear characteristics should be explored further. We are, in fact, working on methods for generalizing it to systems with seasonal cycle[1], sea ice and continents. We are also considering using both EMICs and AO-GCM data to test how the method would work if a dynamical deep-ocean is included.

- Based on the curves in Figure 3.11(b), it was mentioned that a forcing is most efficient for producing global warming if it is inserted at high latitudes. It is then natural to ask: What is the optimal shape of a forcing for producing global warming? Which measure should be used to determine this optimality? How does such an optimal forcing compare with current and possible future anthropogenic forcings? This is a line of inquiry we are pursuing and it can be shown that if simple ℓ_2-norms are used, the optimal forcing can be calculated from the Jacobian.

- The importance of the meridional differences in the surface budget sensitivity relative to the heat transport mechanism for producing the polar amplification was not thoroughly investigated. Exactly which processes give these differences and how? How does this effect interact with the heat transport mechanism and how does it behave under more "exotic" climate conditions (as in Section 3.3)?

- It was mentioned in the Introduction, that Graversen (2005) could ascribe some of the Arctic surface air temperature change during 1958–2001 to a change in the meridional heat transport. How do these observations compare with the heat transport mechanism proposed here?

5.3 Conclusion

Global climate warming such as that due to an increase in the atmospheric CO_2 content has been the focus of this thesis. We have specifically been interested in mechanisms leading to polar amplification of this warming, and we have investigated linear methods of determining

[1] A 1000 year run with seasonal cycle has been performed.

the characteristics of a present-day-like climate state. Many of our analyses and arguments have, in fact, been based exactly on linear causalities, and these have been demonstrated to be very useful; as long as present-day-like climate states are considered and only small climate perturbations are applied, we can achieve a healthy intuition of the system with "linear thinking".

We have also considered the relationship between our model and the simpler models often used to explore the possibility of alternative climate regimes. We found that when the non-linearity associated with sea ice effects are introduced, limitations are placed on the abilities of our linear understanding. Even without sea ice, we found that the heat transport mechanism for polar amplification could not be extrapolated linearly to just any climate of the Earth's past.

There is a generally an optimism in the climate modeling community: *The models might not agree on everything, and there is, of course, ample room for model improvements, but we are getting the basic things right.* What if we are not? What if the fact that our coupled AO-GCMs are unable to account for the very warm poles in the early Cenozoic is due to a lack of a fundamental and powerful feedback? In that case, there might be large surprises in store for us, and polar amplification of the warming will have important global ramifications. This is hopefully not the case, but only time – and perhaps continued development of the whole model spectrum – will tell.

Appendix A

List of symbols

This appendix gives a list of the symbols used throughout the text — sometimes a symbol may be used for multiple purposes.

a	the radius of Earth (6371 km)
A	parameter in linear OLR parameterization
A03	Alexeev (2003)
AGCM	atmospheric general circulation model
AO-GCM	coupled atmosphere-ocean general circulation model
b_i	expansion coefficients
$\mathbf{b}_{Srf}$	surface forcing
b.y.	billion years
B	sensitivity of OLR to SST changes in OLR parameterization
c_w	specific heat capacity of sea water
c_i	ith layer cloud fraction
C	combination of parameters determining cloud optical properties
Cld	cloud
CCM	Community Climate Model
CRF	cloud radiative forcing
CSM	Climate System Model
D	diffusion coefficient
D_{ref}	reference diffusion coefficient
E	evaporation
ECMWF	European Centre for Medium-Range Weather Forecasts
EBM	energy balance model
EKE	eddy kinetic energy
f	Coriolis parameter
F_a	poleward atmospheric heat transport
F_{ds}	poleward dry static energy transport

F_L	poleward latent heat transport
F_{LH}	upward latent heat flux at surface
F_{L+H}	upward turbulent (latent+sensible) heat flux at surface
F_{LW}	upward longwave radiation at surface
$F_{LW,clr}$	upward longwave clear-sky radiation at surface
$F_{LW,TOA}$	upward longwave radiation at top-of-atmosphere, i.e. OLR
F_{SH}	upward sensible heat flux at surface
F_{SW}	downward solar flux at surface
$F_{SW,clr}$	downward solar clear-sky flux at surface
FDT	fluctuation-dissipation theorem
FOAM	Fast Ocean-Atmosphere Model
g	acceleration of gravity
G	ghost forcing
GCM	general circulation model
GMT	Greenwich Mean Time
H	mixed-layer depth
ITCZ	Inter-tropical convergence zone
L_v	latent heat of vaporization
LWP	liquid water path
LW	longwave
M	contribution to CRF from mean clouds
N	Brunt-Väisälä frequency
N	number of layers in a cloud deck
NCAR	National Center for Atmospheric Research
NCEP	National Centers for Environmental Prediction
Ma	million years before present
My	million years
OLR	outgoing longwave radiation
p	pressure
pdf	probability density function
ppm	parts per million
P	precipitation
P_i	ith order Legendre polynomial
PC	pattern coefficient
PW	Petawatt (10^{15} W)
q-flux	Meridional oceanic heat flux convergence
q	time step in FDT method
q	absolute humidity
q	scaling of cloud variability
q_s	saturation specific humidity

Q	a fourth of the solar constant
r	derivative of diffusion coefficient with respect to T_m
rms	root-mean-square
$\boldsymbol{\mathcal{R}}$	Jacobian of surface energy budget with respect to SSTs
R	net downward TOA radiation
R_{clr}	clear-sky net downward TOA radiation
RH	relative humidity
SAT	surface air temperature
SICI	small ice cap instability
$S(x)$	heating function
$\mathbf{S}$	deterministic time-stepping operator
SST	sea surface temperature
SW	shortwave
t	time
T	temperature
T	direct-beam radiation transmission
T21,T42	Horizontal resolution in spectral model. Triangular truncation with maximum wavenumber 21 or 42
T_f	freezing temperature of sea water ($-1.9°$C)
T_S	sea surface temperature (SST)
T_{Src}	source-region surface temperature
T_m	global mean temperature
T_{ref}	reference global mean temperature
ΔT	equator-to-pole temperature gradient
TOA	top-of-atmosphere
u	zonal velocity
v	meridional velocity
$\mathbf{v}$	eigenvector
V	contribution to CRF from cloud variability
V	meridional velocity scale
x	sine of latitude
x_i	ith layer clear-sky fraction
$\mathbf{x}_S$	surface temperature vector
z	vertical coordinate, height
α	earth-atmosphere albedo
$\boldsymbol{\epsilon}$	noise vector
λ	eigenvalue

λ	longitude
Λ	collection of external parameters (solar constant, volcanic forcing, CO_2 etc.)
μ_0	sine of zenith angle
ρ_w	density of sea water
σ_{BI}	Eady growth-rate
ϕ	latitude
ϕ_H	latitude of poleward boundary of Hadley cell
ϕ_{ST}	latitude of storm track axis
$\boldsymbol{\phi}$	eigenvector
τ	cloud extinction optical depth

Appendix B

Calculating implied atmospheric energy transports

When evaluating the meridional atmospheric heat transport at a latitude circle, ϕ, from observations or model data, two methods can be used. One approach (e.g., Grotjahn, 1993) is to calculate it directly from the meridional velocity,

$$F_a = \frac{2\pi a \cos\phi}{g} \int dp \overline{[v(C_p T + \Phi + Lq]}, \tag{B.1}$$

where a is the radius of the Earth, g is the acceleration of gravity, v is the meridional velocity, C_p is the heat capacity at constant pressure, T is the temperature, Φ is the geopotential, L is the latent heat of condensation, q is the water vapor mixing ratio and p is the pressure. The integral is taken over the whole atmospheric column and the overbar and brackets denote time and zonal averages, respectively. The first two terms give the transport of sensible heat and potential energy, respectively, and their sum constitutes the dry static energy transport. The latter term gives the latent heat transport.

An alternative, and often easier and more accurate, way of calculating the energy transports is to infer them from the top-of-atmosphere (TOA) and surface budgets. In (quasi-) steady state where the long-term average of a column's energy content can be assumed constant, the energy fluxes in and out of it must balance. Consider an infinitesimal latitude band centered at ϕ, of width $a \times d\phi$, and its vertical extension from the surface to the TOA. The flux into the circular "wall" is the net downward flux at the TOA

$$2\pi a \cos\phi \ \overline{[B_{TOA}]} \ a d\phi,$$

while those leaving the "wall" are the net downward surface flux and the divergence of the meridional energy transport,

$$2\pi a \cos\phi \ \overline{[B_{Srf}]} \ a d\phi \quad \text{and} \quad dF_a.$$

Balancing these fluxes leads to

$$\frac{dF_a}{d\phi} = 2\pi a^2 \cos\phi[\overline{B_{TOA} - B_{Srf}}], \tag{B.2}$$

and integration from the south pole to the latitude, ϕ, yields

$$F_a = 2\pi a^2 \int_{-\frac{\pi}{2}}^{\phi} d\phi \cos\phi[\overline{B_{TOA} - B_{Srf}}]. \tag{B.3}$$

A similar calculation can be performed for the latent heat transport alone by considering the surface budget of evaporation, E, minus precipitation, P:

$$F_L = 2\pi a^2 L \int_{-\frac{\pi}{2}}^{\phi} d\phi \cos\phi[\overline{E - P}], \tag{B.4}$$

where E and P are in units of [kg m^{-2} s^{-1}].

Appendix C

Legendre polynomials

This appendix provides a short outline of the most important properties of the Legendre polynomials used on several occasions throughout this thesis. It can be shown that the solution to Legendre's differential equation

$$(1-x^2)y'' - 2xy' + n(n+1)y = 0, \tag{C.1}$$

is the nth order Legendre polynomial,

$$P_n(x) = \sum_{m=0}^{M} (-1)^m \frac{(2n-2m)!}{2^n m!(n-m)!(n-2m)!} x^{n-2m}, \tag{C.2}$$

where $M = n/2$ or $M = (n-1)/2$, whichever is an integer (Kreyszig, 1993). The first six Legendre polynomials are given by

$$\begin{aligned} P_0(x) &= 1 & P_1(x) &= x \\ P_2(x) &= \tfrac{1}{2}(3x^2-1) & P_3(x) &= \tfrac{1}{2}(5x^3-3x) \\ P_4(x) &= \tfrac{1}{8}(35x^4-30x^2+3) & P_5(x) &= \tfrac{1}{8}(63x^5-70x^3+15x) \end{aligned}$$

and are plotted in Figure C.1 as functions of $x = \sin(\phi)$, where ϕ is latitude. Note that the order of the polynomials corresponds to the number of roots, and that the parity of the order determines the symmetry of the polynomial. Even-ordered polynomials are symmetric about the equator, while odd ones are anti-symmetric.

Eigenfunctions of diffusion operator

The meridional coordinate $x = \sin(\phi)$ used in Figure C.1 is very common in climate literature (for example, because it has the latitudinal area-weighting built in). We will now consider the diffusion operator, $D\nabla^2 T$, where ∇ is the derivative in the meridional direction, since we are on the Earth's surface and assume zonal symmetry. In spherical coordinates this diffusion

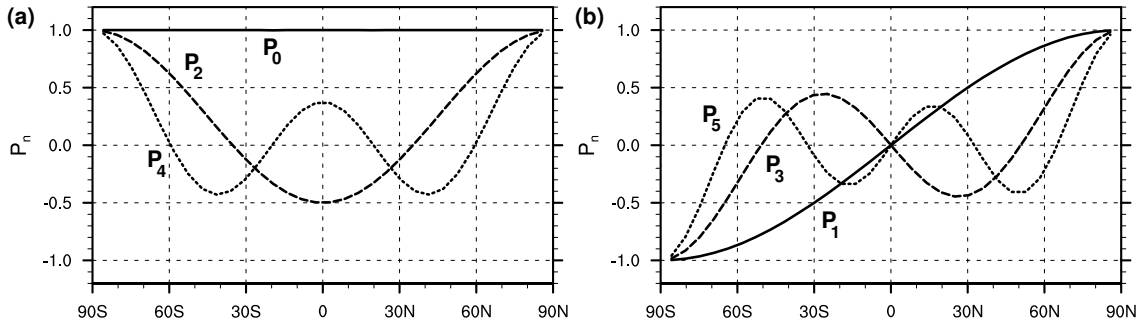

Figure C.1: The first 6 Legendre polynomials plotted as functions of latitude. (a) Even orders: 0th (solid), 2nd (dashed) and 4th (dotted), (b) Odd orders: 1st (solid), 3rd (dashed) and 5th (dotted).

(operating on the field T (temperature, for example)) is

$$D\nabla^2 T = D\frac{1}{a^2 \sin\theta}\frac{\partial}{\partial\theta}\left(\sin\theta\frac{\partial T}{\partial\theta}\right),$$

where θ is the latitude measured from the pole (as is done in mathematics). Since $d\theta = -d\phi$ and $\sin\theta = \cos\phi = \sqrt{1-x^2}$,

$$\begin{aligned} D\nabla^2 T &= \frac{D}{a^2\sqrt{1-x^2}}(-1)\frac{\partial}{\partial\phi}\left(\sqrt{1-x^2}(-1)\frac{\partial T}{\partial\phi}\right) \\ &= \frac{D}{a^2\sqrt{1-x^2}}\sqrt{1-x^2}\frac{\partial}{\partial x}\left(\sqrt{1-x^2}\sqrt{1-x^2}\frac{\partial T}{\partial x}\right) \\ &= \frac{D}{a^2}\frac{\partial}{\partial x}\left((1-x^2)\frac{\partial T}{\partial x}\right). \end{aligned}$$

But this re-writes to

$$D\nabla^2 T = \frac{D}{a^2}\left[(1-x^2)T'' - 2xT'\right],$$

and if T is expressed in terms of Legendre polynomials or, even simpler, $T = P_n$, then

$$D\nabla^2 P_n = -\frac{Dn(n-1)}{a^2}P_n$$

according to (C.1). The Legendre polynomials are in other words eigenfunctions of the meridional diffusion operator (the Laplacian). This makes them particularly useful in climate contexts and they have been used extensively in energy balance model studies (e.g., North, 1975a,b).

Other useful properties

The formula (C.2) is not very applicable in practice. Instead, Bonnet's recursion,

$$P_{n+1}(x) = \frac{1}{n+1}\left[(2n+1)xP_n(x) - nP_{n-1}(x)\right], \tag{C.3}$$

is very easy to use when the two first polynomials, 1 and x, are known. The Legendre polynomials can be shown to be orthogonal,

$$\int_{-1}^{1} P_m(x)P_n(x)dx = 0 \quad \text{if} \quad m \neq n,$$

and have ℓ_2-norm

$$\|P_m\| = \left(\int_{-1}^{1} P_m^2(x)dx\right)^{-1/2} = \sqrt{\frac{2}{2m+1}}.$$

When normalized, the Legendre polynomials give the meridional structure of the zonally symmetric spherical harmonics:

$$Y_n^0(\lambda, x) = \sqrt{\frac{2n+1}{2}}P_n(x),$$

where λ is longitude and x again equals the sine of latitude.

Bibliography

Abdalati, W. and Steffen, K. (2001). Greenland ice sheet melt extent: 1979–1999. *J. Geophys. Res.*, 106:33,983–33,988.

ACIA (2004). *Impacts of a warming Arctic: Arctic Climate Impact Assessment.* Cambridge University Press.

Alexeev, V. A. (2003). Sensitivity to CO_2 doubling of an atmospheric GCM coupled to an oceanic mixed layer: a linear analysis. *Clim. Dyn.*, 20:775–787.

Alexeev, V. A., Langen, P. L., and Bates, J. R. (2005). Polar amplification of surface warming on an aquaplanet in "ghost forcing" experiments without sea ice feedbacks. *Clim. Dyn.*, doi:10.1007/s00382-005-0018-3.

Allan, R. P., Shine, K. P., Slingo, A., and Pamment, J. A. (1999). The dependence of clear-sky outgoing long-wave radiation on surface temperature and relative humidity. *Q. J. R. Met. Soc.*, 125:2103–2126.

Allen, M. R. and Ingram, W. J. (2002). Constraints on future changes in climate and the hydrologic cycle. *Nature*, 419:224–232.

Arrhenius, S. (1896). On the influence of carbonic acid in the air upon the temperature of the ground. *Phil. Mag.*, 41:237–276.

Augustsson, T. and Ramanathan, V. (1977). A radiative-convective model study of the CO_2 climate problem. *J. Atmos. Sci.*, 34:448–451.

Barker, H. W., Stephens, G. L., Partain, P. T., Bergman, J. W., Bonnel, B., Campana, K., Clothiaux, E. E., Clough, S., Cusack, S., Delamere, J., Edwards, J., Evans, K. F., Fouquart, Y., Freidenreich, S., Galin, V., Hou, Y., Kato, S., Li, J., Mlawer, E., Morcrette, J.-J., O'Hirok, W., Räisänen, P., Ramaswamy, V., Ritter, B., Rozanov, E., Schlesinger, M., Shibata, K., Sporyshev, P., Sun, Z., Wendisch, M., Wood, N., and Yang, F. (2003). Assessing 1D Atmospheric Solar Radiative Transfer Models: Interpretation and Handling of Unresolved Clouds. *Journal of Climate*, 16:2676–2699.

Barsugli, J., Shin, S., and Sardeshmukh, P. D. (2005). Tropical climate regimes and global climate sensitivity in a simple setting. *J. Atmos. Sci.*, 62:1226–1240.

Bates, J. R. (2003). On climate stability, climate sensitivity and the dynamics of the enhanced greenhouse effect. DCESS Report No.3, available from Department of Geophysics, University of Copenhagen http://www.dclimate.gfy.ku.dk.

Baum, S. K. and Crowley, T. J. (2003). The snow/ice instability as a mechanism for rapid climate change: A Neoproterozoic Snowball Earth model example. *Geophys. Res. Lett.*, 30:doi:10.1029/2003GL017333.

Bell, T. L. (1980). Climate sensitivity from fluctuation dissipation: some simple model tests. *J. Atmos. Sci.*, 37:1700–1707.

Bergman, J. W. and Salby, M. L. (1997). The Role of Cloud Diurnal Variations in the Time-Mean Energy Budget. *J. Climate*, 10:1114–1124.

Bess, T. D., Smith, G. L., and Charlock, T. P. (1989). A ten-year monthly data set of outgoing longwave radiation from nimbus-6 and nimbus-7 satellites. *Bull. Amer. Met. Soc.*, 70(1989):480–489.

Boer, G. J. (1993). Climate change and the regulation of the surface moisture and energy budgets. *Clim. Dyn.*, 8:225–239.

Boer, G. J. (1995). Some dynamical consequences of greenhouse gas warming. *Atmos.-Oc.*, 33:731–751.

Briegleb, B. P. (1992). Delta-eddington approximation for solar radiation in the NCAR Community Climate Model. *J. Geophys. Res.*, 97(D7):7603–7612.

Budyko, M. (1969). The effect of solar radiation variations on the climate of the Earth. *Tellus*, 21(5):611–619.

Caballero, R. and Langen, P. L. (2005). The dynamic range of poleward energy transport in an atmospheric general circulation model. *Geophys. Res. Lett.*, 32:L02705, doi:10.1029/2004GL021581.

Caldeira, K. and Kasting, J. F. (1992). Susceptibility of the early Earth to irreversible glaciation caused by carbon dioxide clouds. *nature*, 359:226–228.

Callen, H. B. and Green, R. F. (1952). On a theorem of irreversible thermodynamics. *Phys. Rev.*, 86:702–710.

Carissimo, B. C., Oort, A. H., and Haar, T. H. V. (1985). Estimating the meridional energy transport in the atmosphere and ocean. *J. Phys. Oceanogr.*, 15:82–91.

Cess, R. D., Genio, A. D., Dix, M., Esch, M., Fowler, L., Fraser, J., Galin, V., Gates, W., Hack, J., Kiehl, J., Treut, H. L., Zhang, M., Lo, K., McAvaney, B., Meleshko, V., Morcrette, J., Randall, D., Roeckner, E., Royer, J., Schlesinger, M., Sporyshev, P., Timbal, B., Ingram, W., Volodin, E., Taylor, K., Wang, W., Wetherald, R., Potter, G., Alekseev, V., Barker, H., Cohen-Solal, E., Colman, R., and Dazlich, D. (1996). Cloud feedback in atmospheric general circulation models: An update. *J. Geophys. Res.*, 101D:12791–12794.

Cess, R. D. and Potter, G. L. (1987). Exploratory studies of cloud radiative forcing with a general circulation model. *Tellus*, 39:460–473.

Cess, R. D., Potter, G. L., Blanchet, J. P., Boer, G. J., Del Genio, A. D., Déqué, M., Dymnikov, V., Galin, V., Gates, W. L., Ghan, S. J., Kiehl, J. T., Lacis, A. A., Le Treut, H., , Li, Z., Liang, X., McAvaney, B. J., Meleshko, V. P., Mitchell, J. F. B., Morcrette, J.-J., Randall, D. A., Rikus, L., Roeckner, E., Royer, J. F., Schlese, U., Sheinin, D. A., Slingo, A., Sokolov, A. P., Taylor, K. E., Washington, W. M., Wetherald, R. T., Yagai, I., and Zhang, M.-H. (1990). Intercomparison and interpretation of climate feedback processes in 19 atmospheric general circulation models. *J. Geophys. Res.*, 95:16601–16615.

Cess, R. D., Potter, G. L., Zhang, M.-H., Blanchet, J.-P., Chalita, S., Colman, R., Dazlich, D. A., Genio, A. D. D., Dymnikov, V., Galin, V., Jerret, D., Keup, E., Lacis, A. A., Le Treut, H., Liang, X.-Z., Mahfouf, J.-F., McAvaney, B. J., Meleshko, V. P., Mitchell, J. F. B., Morcrette, J.-J., Norris, P. M., Randall, D. A., Rikus, L., Roeckner, E., Royer, J.-F., Schlese, U., Sheinin, D. A., Slingo, J. M., Sokolov, A. P., Taylor, K. E., Washington, W. M., Wetherald, R. T., and Yagai, I. (1991). Interpretation of snow-climate feedback as produced by 17 general circulation models. *Science*, 253:888–892.

Chapman, W. L. and Walsh, J. E. (1993). Recent variations of sea ice and air temperatures in high latitudes. *Bull. Amer. Meteor. Soc.*, 74:33–47.

Chen, D., Gerdes, R., and Lohmann, G. (1995). A 1-d atmospheric energy balance model developed for ocean modeling. *Theor. Appl. Climatol.*, 51:25–38.

Chýlek, P. and Coakley, J. A. (1975). Analytical analysis of a Budyko-type climate model. *J. Atmos. Sci.*, 32:675–679.

Cionni, I., Visconti, G., and Sassi, F. (2004). Fluctuation dissipation theorem in a general circulation model. *Geophys. Res. Lett.*, 31:doi:10.1029/2004GL019739.

Claussen, M., Mysak, L. A., Weaver, A. J., Crucifix, M., Fichefet, T., Loutre, M.-F., Weber, S. L., Alcamo, J., Alexeev, V. A., Berger, A., Calov, R., Ganopolski, A., Goosse, H., Lohmann, G., Lunkeit, F., Mokhov, I. I., Petoukhov, V., Stone, P., and Wang, Z. (2002). Earth system models of intermediate complexity: closing the gap in the spectrum of climate system models. *Clim. Dyn.*, 18:579–586.

Cohen-Solal, E. and Le Treut, H. (1997). Role of the oceanic heat transport in climate dynamics. A sensitivity study with an atmospheric general circulation model. *Tellus*, 49A:371–387.

Cohen-Solal, E. and Le Treut, H. (1999). Unstable behavior of an upper ocean-atmosphere coupled model: role of atmospheric radiative processes and oceanic heat transport. *Clim. Dyn.*, 15:895–908.

Collins, W. D., Rasch, P. J., Boville, B. A., Hack, J. J., McCaa, J. R., Williamson, D. L., Briegleb, B. P., Bitz, C. M., Lin, S.-J., and Zhang, M. (2005). The formulation and atmospheric simulation of the Community Atmosphere Model: CAM3. *Submitted to J. Clim. special issue on CCSM.*

Colman, R. (2003). A comparison of climate feedbacks in general circulation models. *Clim. Dyn.*, 20:865–873.

Colman, R., Fraser, J., and Rotstayn, L. (2001). Climate feedbacks in a general circulation model incorporating prognostic clouds. *Clim. Dyn.*, 18:103–122.

Comiso, J. C. (2003). warming trends in the Arctic from clear sky satellite observations. *J. Climate*, 16:3498–3510.

Crowley, T. J. and Hyde, W. T. (2001). CO_2 levels required for deglaciation of a "Near-Snowball" Earth. *Geophys. Res. Lett.*, 28:283–286.

Deser, C., Walsh, J. E., and Timlin, M. S. (2000). Arctic sea ice variability in the context of recent atmospheric circulation trends. *J. Climate*, 13:617–633.

Dong, B. and Valdes, P. J. (2000). Climates of the Last Glacial Maximum: Influence of model horizontal resolution. *J. Climate*, 13:1554–1573.

Durran, D. R. (1999). *Numerical methods for wave equations in geophysical fluid dynamics.* Spinger-Verlag New York, Inc.

Einstein, A. (1905). Über die von der molekularkinetischen Theorie der Wärme geforderte Bewegungen von in ruhenden Flüssigkeiten suspendierten Teilchen. *Ann. Phys.*, 17:549–560.

Ganopolski, A. and Rahmstorf, S. (2001). Rapid changes of glacial climate in a coupled climate model. *Nature*, 409:153–158.

Graversen, R. G. (2005). Do changes in mid-latitude circulation have any impact on the Arctic surface air temperature trend? *Submitted to J. Climate.*

Graves, C. E., Lee, W.-H., and North, G. R. (1993). New parameterizations and sensitivities for simple climate models. *J. Geophys. Res.*, 98(D3):5025–5036.

Grotjahn, R. (1993). *Global Atmospheric Circulations – Observations and Theories.* Oxford University Press.

Gutzler, D. S. and Stone, P. H. (1986). Infrared flux parameterizations derived from climate changes in a three-dimensional climate model. *J. Geophys. Res.*, 91(D7):7797–7802.

Hack, J. J. (1992). *Climate system simulation: basic numerical & computational concepts, in Climate System Modeling, ed. K. E. Trenberth.* Cambridge University Press, pp 788.

Hack, J. J., Kiehl, J. T., and Hurrell, J. W. (1998). The hydrologic and thermodynamic characteristics of the NCAR CCM3. *J. Climate*, 11:1179–1206.

Hall, A. (2004). The role of surface albedo feedback in climate. *J. Climate*, 17:1550–1568.

Hansen, J., Sato, M., and Ruedy, R. (1997). Radiative forcing and climate response. *J. Geophys. Res.*, 102(D6):6831–6864.

Harshvardhan and Randall, D. A. (1985). Comments on "The parameterization of radiation for numerical weather prediction and climate models". *Mon. Wea. Rev.*, 113:1832–1833.

Hartmann, D. L. (1994). *Global Physical Climatology.* Academic Press.

Held, I. M. (1982). On the height of the tropopause and the static stability of the troposphere. *J. Atmos. Sci.*, 32:412–417.

Hewitt, C. D., Senior, C. A., and Mitchell, J. F. B. (2001). The impact of dynamic sea-ice on the climatology and climate sensitivity of a GCM: a study of past, present, and future climates. *Clim. Dyn.*, 17:655–668.

Hoffman, P. F., Kaufman, A. J., Halverson, G. P., and Schrag, D. P. (1998). A Neoproterozoic Snowball Earth. *Science*, 281:1342–1346.

Hoffman, P. F. and Schrag, D. P. (2000). Snowball Earth. *Scientific American*, 282:50–57.

Holopainen, E. O. (1965). On the role of mean meridional circulations in the energy balance of the atmosphere. *Tellus*, 17:285–294.

Hoskins, B. J. and Valdes, P. J. (1990). On the existence of storm-tracks. *J. Atmos. Sci.*, 47:1854–1864.

Houghton, J. T., Ding, Y., Griggs, D. J., Noguer, M., van der Linden, P. J., and D. Xiaosu, *Eds.* (2001). *IPCC, Climate Change 2001: The Scientific Basis.* Cambridge University Press, 944pp.

Huber, M. and Sloan, L. C. (1999). Warm climate transitions: A general circulation modeling study of the Late Paleocene Thermal Maximum (∼56 Ma). *J. Geophys. Res.*, 104:16,633–16,655.

Huber, M. and Sloan, L. C. (2000). Climatic responses to tropical sea surface temperature changes on a "greenhouse" Earth. *Paleoceanography*, 15:443–450.

Huber, M. and Sloan, L. C. (2001). Heat transport, deep waters and thermal gradients: Coupled climate simulation of an Eocene greenhouse climate. *Geophys. Res. Lett.*, 28:3481–3484.

Hurrell, J. W., Hack, J. J., Boville, B. A., Williamson, D. L., and Kiehl, J. T. (1998). The dynamical simulation of the NCAR Community Climate Model Version 3 (CCM3). *J. Climate*, 11:1206–1236.

Hyde, W. T., Crowley, T. J., Baum, S. K., and Peltier, W. R. (2000). Neoproterozoic 'snowball Earth' simulations with a coupled climate/ice-sheet model. *Nature*, 405:425–429.

Ide, K., Le Treut, H., Li, Z.-X., and Ghil, M. (2001). Atmospheric radiative equilibria. Part II: bimodal solutions for atmospheric optical properties. *Clim. Dyn.*, 18:29–49.

Jacob, R. (1997). *Low frequency variability in a simulated atmosphere ocean system.* PhD thesis, Univ. of Wisc.-Madison.

Jenkins, G. S. and Smith, S. R. (1999). GCM simulations of Snowball Earth conditions during the late Proterozoic. *Geophys. Res. Lett.*, 26:2263–2266.

Johannessen, O. M., Bengtsson, L., Miles, M. W., Kuzmina, S. I., Semenov, V. A., Alekseev, G. V., Nagurnyi, A. P., Zakharov, V. F., Bobylev, L. P., Pettersson, L. H., Hasselmann, K., and Cattle, H. P. (2004). Arctic climate change: observed and modelled temperature and sea-ice variability. *Tellus*, 56A:328–341.

Johnsen, S. J., Dahl-Jensen, D., Dansgaard, W., and Gundestrup, N. (1995). Greenland paleotemperatures derived from GRIP bore hole temperature and ice core isotope profiles. *Tellus*, 47B:624–629.

Juckes, M. N. (2000). The static stability of the midlatitude troposphere: The relevance of moisture. *J. Atmos. Sci.*, 57:3050–3057.

Kasting, J. F. (1989). Long-term stability of the Earth's climate. *Palaeogeogr. Palaeoclimatol. Palaeoecol.*, 75:83–95.

Kiehl, J. T. (1992). *Atmospheric general circulation modeling, in Climate System Modeling, ed. K. E. Trenberth.* Cambridge University Press, pp 788.

Kiehl, J. T. and Gent, P. R. (2004). The Community Climate System Model, Version 2. *J. Climate*, 17:3666–3682.

Kiehl, J. T., Hack, J. J., Bonan, G. B., Boville, B. A., Briegleb, B. P., Williamson, D. L., and Rasch, P. J. (1996). Description of the NCAR Community Climate Model (CCM3). Technical Report TN-420, CGD, National Center for Atmospheric Research.

Kiehl, J. T., Hack, J. J., Bonan, G. B., Boville, B. A., Williamson, D. L., and Rasch, P. J. (1998a). The National Center for Atmospheric Research Community Climate Model: CCM3. *J. Climate*, 11:1131–1149.

Kiehl, J. T., Hack, J. J., and Hurrell, J. W. (1998b). The energy budget of the NCAR Community Climate Model: CCM3. *J. Climate*, 11:1151–1178.

Kirk-Davidoff, D. B., Schrag, D. P., and Anderson, J. G. (2002). On the feedback of stratospheric clouds on polar climate. *Geophys. Res. Lett.*, 29:doi:10.1029/2002GL014659.

Kraichnan, R. H. (1959). Classical fluctuation-relaxation theorem. *Phys. Rev.*, 113:1181–1182.

Kreyszig, E. (1993). *Advanced engineering mathematics*. John Wiley & Sons, Inc., 7th ed, 1271pp.

Langen, P. L. and Alexeev, V. A. (2004). Multiple equilibria and asymmetric climates in the CCM3 coupled to an oceanic mixed layer with thermodynamic sea ice. *Geophys. Res. Lett.*, 31:doi: 10.1029/2003GL019039.

Langen, P. L. and Alexeev, V. A. (2005a). Estimating $2\times CO_2$ warming in an aquaplanet GCM using the fluctuation-dissipation theorem. *Submitted to Geophys. Res. Lett.*

Langen, P. L. and Alexeev, V. A. (2005b). A study of non-local effects on the Budyko-Sellers infrared parametrization using atmospheric general circulation models. *Tellus*, 57A:654–661.

Langen, P. L. and Caballero, R. (2005). Climate impact of temporal cloud variability in a general circulation model. *Submitted to J. Climate.*

Lapeyre, G. and Held, I. M. (2004). The role of moisture in the dynamics and energetics of turbulent baroclinic eddies. *J. Atmos. Sci.*, 61:1693–1710.

Le Treut, H., Li, Z. X., and Forichon, M. (1994). Sensitivity of the LMD General Circulation Model to Greenhouse Forcing Associated with Two Different Cloud Water Parameterizations. *J. Climate*, 7:1827–1841.

Lee, W.-H. and North, G. R. (1995). Small ice cap instability in the presence of fluctuations. *Clim. Dyn.*, 11:242–246.

Leith, C. E. (1975). Climate response and fluctuation dissipation. *J. Atmos. Sci.*, 32:2022–2026.

Leith, C. E. (1978). Predictability of climate. *Nature*, 276:352–355.

Li, Z.-X., Ide, K., Le Treut, H., and Ghil, M. (1997). Atmospheric radiative equilibria in a simple column model. *Clim. Dyn.*, 13:429–440.

Lin, R. Q. and North, G. R. (1990). A study of abrupt climate change in a simple nonlinear climate model. *Clim. Dyn.*, 4:253–261.

Lindzen, R. S. (1990). Some coolness concerning global warming. *Bull. Amer. Met. Soc.*, 71:288–299.

Lindzen, R. S. and Farrell, B. F. (1980). A simple approximate result for the maximum growth rate of baroclinic instabilities. *J. Atmos. Sci.*, 37:1648–1654.

Lindzen, R. S., Hou, A. Y., and Farrell, B. F. (1982). The role of convective model choice in calculating the climate impact of doubling CO_2. *J. Atmos. Sci.*, 39:1189–1205.

Lohmann, G., Gerdes, R., and Chen, D. (1996). Sensitivity of the thermohaline circulation in coupled oceanic GCM - atmospheric EBM experiments. *Clim. Dyn.*, 12:403–416.

Lorenz, E. N. (1963a). Deterministic nonperiodic flow. *J. Atmos. Sci.*, 20:130–141.

Lorenz, E. N. (1963b). The predictability of hydrodynamic flow. *Trans. New York Acad. Sci.*, Ser 2, 25:409–432.

Lorenz, E. N. (1969). The predictability of a flow which possesses many scales of motion. *Tellus*, 21:289–307.

Manabe, S., Smagorinsky, J., Holloway, J. L., and Stone, H. M. (1970). Simulated climatology of a general circulation model with a hydrologic cycle. III: Effects of increased horizontal resolution. *Mon. Wea. Rev.*, 98:175–212.

Manabe, S., Smagorinsky, J., and Strickler, R. F. (1965). Simulated climatology of a general circulation model with a hydrological cycle. *Mon. Wea. Rev.*, 93:769–798.

Manabe, S. and Stouffer, R. J. (1980). Sensitivity of a global climate model to an increase of CO_2 concentration in the atmosphere. *J. Geophys. Res.*, 85:5529–5554.

Manabe, S. and Stouffer, R. J. (1988). Two stable equilibria of a coupled ocean-atmosphere model. *J. Climate*, 1:841–866.

Manabe, S., Stouffer, R. J., Spelman, M. J., and Bryan, K. (1991). Transient responses of a coupled ocean-atmosphere model to gradual changes in atmospheric CO_2. Part I: annual mean response. *J. Climate*, 4:785–818.

Manabe, S., Stouffer, R. J., Spelman, M. J., and Bryan, K. (1992). Transient responses of a coupled ocean-atmosphere model to gradual changes in atmospheric CO_2. Part II: seasonal response. *J. Climate*, 5:105–126.

Manabe, S. and Strickler, R. F. (1964). Thermal equilibrium of the atmosphere with a convective adjustment. *J. Atmos. Sci.*, 21:361–385.

Manabe, S. and Wetherald, R. T. (1967). Thermal equilibration of the atmosphere with a given distribution of relative humidity. *J. Atmos. Sci.*, 24:241–259.

Manabe, S. and Wetherald, R. T. (1975). The effects of doubling the CO_2 concentration on the climate of a general circulation model. *J. Atmos. Sci.*, 32:3–15.

Manabe, S. and Wetherald, R. T. (1980). On the distribution of climate change resulting from an increase in the CO_2 content of the atmosphere. *J. Atmos. Sci.*, 37:99–118.

Marani, M. (1999). Parametrizations of global thermal emissions for simple climate models. *Clim. Dyn.*, 15:145–152.

Markwick, P. J. (1994). Equability, continentality and Tertiary climate: The crocodilian perspective. *Geology*, 22:613–616.

Marotzke, J. and Stone, P. H. (1995). Atmospheric transports, the thermohaline circulation, and flux adjustments in a simple coupled model. *J. Phys. Oceanogr.*, 25:1350–1364.

McGuffie, K. and Henderson-Sellers, A. (2001). Forty years of numerical climate modelling. *Int. J. Climatol.*, 21:1067–1109.

Mengel, J. G., Short, D. A., and North, G. R. (1988). Seasonal snowline instability in an energy balance model. *Clim. Dyn.*, 2:127–131.

Nakamura, M., Stone, P. H., and Marotzke, J. (1994). Destabilization of the thermohaline circulation by atmospheric eddy transport. *J. Climate*, 7:1870–1882.

Nazarenko, L., Hansen, J., Tausnev, N., and Ruedy, R. (2001). Response of the northern hemisphere sea ice to greenhouse forcing in a global climate model. *Ann. Glac.*, 33:513–520.

Neeman, B. U., Joseph, J. H., and Ohring, G. (1987). The sensitivity of the outgoing longwave radiation to surface temperature: Modeling the opacity feedback and experiments with a variable cloud-top temperature provision. *J. Atmos. Sci.*, 44:2995–3006.

North, G. R. (1975a). Analytical solution to a simple climate model with diffusive heat transport. *J. Atmos. Sci.*, 32:1301–1307.

North, G. R. (1975b). Theory of energy-balance climate models. *J. Atmos. Sci.*, 32:2033–2043.

North, G. R. (1984). The small ice cap instability in diffusive climate models. *J. Atmos. Sci.*, 41:3390–3395.

North, G. R. (1990). Multiple solutions in energy balance climate models. *Palaeogeogr., Palaeoclimatol., Palaeoecol.*, 82:225–235.

North, G. R., Bell, R. E., and Hardin, J. W. (1993). Fluctuation dissipation in a general circulation model. *Clim. Dyn.*, 8:259–264.

North, G. R., Cahalan, R. F., and Coakley, J. A. (1981). Energy balance climate models. *Rev. Geophys. Space Phys.*, 19:91–121.

North, G. R. and Crowley, T. J. (1985). Application of a seasonal climate model to Cenozoic glaciation. *J. Geol. Soc. London*, 142:475–482.

North, G. R., Mengel, J. G., and Short, D. A. (1983). Simple energy balance model resolving the seasons and the continents: application to the astronomical theory of the ice ages. *J. Geophys. Res.*, 88:6576–6586.

Nyquist, H. (1928). Thermal agitation of electric charge in conductors. *Phys. Rev.*, 32:110–113.

Parkinson, C. L., Cavalieri, D. J., Gloersen, P., Zwally, H. J., and Comiso, J. C. (1999). Arctic sea ice extents, areas, and trends, 1978–1996. *J. Geophys. Res.*, 104:20,837–20,856.

Petit, J. R., Jouzel, J., Raynaud, D., Barkov, N., Barnola, J.-M., Basile, I., Benders, M., Chappellaz, J., Davis, M., Delayque, G., Delmotte, M., Kotlyakov, V. M., Legrand, M., Lipenkov, V. Y., Lorius, C., Pépin, L., Ritz, C., Saltzman, E., and Stievenard, M. (1999). Climate and atmospheric history of the past 420,000 years from the Vostok ice core, Antarctica. *Nature*, 399:429–436.

Phillips, N. A. (1956). The general circulation of the atmosphere: A numerical experiment. *Quart. J. Roy. Meteor. Soc.*, 82:123–164.

Pierrehumbert, R. T. (2002). The hydrological cycle in deep-time climate problems. *Nature*, 419:191–198.

Pierrehumbert, R. T. (2004). High levels of atmospheric carbon dioxide necessary for the termination of global glaciation. *Nature*, 429:646–649.

Pollard, D. and Thompson, S. L. (1994). Sea-ice dynamics and CO_2 sensitivity in a global climate model. *Atmos.-Oc.*, 32:449–467.

Polyakov, I. V., Alekseev, G. V., Bekryaev, R. V., Bhatt, U., Colony, R. L., Johnson, M. A., Karklin, V. P., Makshtas, A. P., Walsh, D., and Yulin, A. V. (2002). Observationally based assessment of polar amplification of global warming. *Geophys. Res. Lett.*, 29(18):1878.

Pope, V. D. and Stratton, R. A. (2002). The processes governing horizontal resolution sensitivity in a climate model. *Clim. Dyn.*, 19:211–236.

Potter, G. L. and Cess, R. D. (2004). Testing the impact of clouds on the radiation budgets of 19 atmospheric general circulation models. *J. Geophys. Res.*, 109D(18):doi:10.1029/2003JD004018.

Poulsen, C. J., Pierrehumbert, R. T., and Jacob, R. L. (2001). Impact of ocean dynamics on the simulation of the Neoproterozoic "snowball Earth". *Geophys. Res. Lett.*, 28(8):1575–1578.

Räisänen, J. (1998). CO_2- and aerosol-induced changes in vertically integrated zonal momentum budget in a GCM experiment. *J. Climate*, 11:625–639.

Räisänen, J. (2001). CO_2-induced climate change in CMIP2 experiments: quantification of agreement and role of internal variability. *J. Climate*, 14:2088–2104.

Räisänen, J. and Palmer, T. N. (2001). A probability and decision-model analysis of a multimodel ensemble of climate change simulations. *J. Climate*, 14:3212–3226.

Ramanathan, V. (1981). The role of ocean-atmosphere interactions in the CO_2 climate problem. *J. Atmos. Sci.*, 38:918–930.

Ramanathan, V., Cess, R. D., Harrison, E. F., Minnis, P., Barkstrom, B. R., Ahmad, E., and Hartmann, D. (1989). Cloud-radiative forcing and climate: Results from the earth radiation budget experiment. *Science*, 243:57–63.

Ramanathan, V., Crutzen, P. J., Kiehl, J. T., and Rosenfeld, D. (2001). Aerosols, climate, and the hydrological cycle. *Science*, 294:2119–2124.

Randall, D., Khairoutdinov, M., Arakawa, A., and Grabowski, W. (2003). Breaking the cloud parameterization deadlock. *Bull. Amer. Meteor. Soc.*, 84:1547–1564.

Raval, A., Oort, A. H., and Ramaswamy, V. (1994). Observed dependence of outgoing longwave radiation on sea surface temperature and moisture. *J. Climate*, 7:807–821.

Rennó, N. O. (1997). Multiple equilibria in radiative-convective atmospheres. *Tellus*, 49A:423–438.

Rigor, I. G., Colony, R. L., and Martin, S. (2000). Variations in surface air temperature observations in the Arctic, 1979–97. *J. Climate*, 13:896–914.

Rind, D. (1998). Latitudinal temperature gradients and climate change. *J. Geophys. Res.*, 103:5943–5971.

Rind, D. and Chandler, M. (1991). Increased ocean heat transports and warmer climate. *J. Geophys. Res.*, 96(D4):7437–7461.

Rind, D., Healy, R., Parkinson, C., and Martinson, D. (1995). The role of sea ice in 2 × CO_2 climate model sensitivity. Part I: The total influence of sea ice thickness and extent. *J. Climate*, 8:449–463.

Rind, D., Healy, R., Parkinson, C., and Martinson, D. (1997). The role of sea ice in 2 × CO_2 climate model sensitivity: Part II: Hemispheric dependencies. *Geophys. Res. Lett.*, 24(12):1491–1494.

Rodgers, K. B., Lohmann, G., Lorenz, S., Schneider, R., and Henderson, G. M. (2003). A tropical mechanism for Northern Hemisphere deglaciation. *Geochem. Geophys. Geosys.*, 4(5):1046, doi:10.1029/2003GC000508.

Rosen, R. D. and Gutowski, W. J. (1992). Response of zonal winds and atmospheric angular momentum to a doubling of CO_2. *J. Climate*, 5:1391–1404.

Rothrock, D. A., Yu, Y., and Maykut, G. A. (1999). Thinning of the Arctic sea-ice cover. *Geophys. Res. Lett.*, 23:3469–3472.

Saravanan, R. and McWilliams, J. C. (1995). Multiple equilibria, natural variability, and climate transitions in an idealized ocean-atmosphere model. *J. Climate*, 10:2296–2323.

Schneider, E. K., Kirtman, B. P., and Lindzen, R. S. (1999). Tropospheric water vapor and climate sensitivity. *J. Atmos. Sci.*, 56:1649–1658.

Schneider, E. K., Lindzen, R. S., and Kirtman, B. P. (1997). A tropical influence on global climate. *J. Atmos. Sci.*, 54:1349–1358.

Schneider, T. (2004). The tropopause and the thermal stratification in the extratropics of a dry atmosphere. *J. Atmos. Sci.*, 61:1317–1340.

Seager, R., Battisti, D. S., Yin, J., Gordon, N., Naik, N., Clement, A. C., and Cane, M. A. (2002). Is the Gulf Stream responsible for Europe's mild winters? *Quart. J. Roy. Meteor. Soc.*, 128:2563–2586.

Sellers, W. D. (1969). A global climatic model based on the energy balance of the Earth-atmosphere system. *J. Appl. Meteor*, 8:392–400.

Senior, C. A. (1995). The dependence of climate sensitivity on the horizontal resolution of a GCM. *J. Climate*, 8:2860–2880.

Senior, C. A. (1999). Comparison of mechanisms of cloud-climate feedbacks in GCMs. *J. Climate*, 12:1480–1489.

Senior, C. A. and Mitchell, J. F. B. (1993). Carbon Dioxide and Climate: The Impact of Cloud Parameterization. *J. Climate*, 6:393–418.

Shellito, C. J., Sloan, L. C., and Huber, M. (2003). Climate model sensitivity to atmospheric CO_2 levels in the Early-Middle Paleogene. *Palaeogeogr., Palaeoclimatol., Palaeoecol.*, 193:113–123.

Shine, K. P., Cook, J., Highwood, E. J., and Joshi, M. M. (2003). An alternative to radiative forcing for estimating the relative importance of climate change mechanisms. *Geophys. Res. Lett.*, 30(20):2047.

Short, D. A., North, G. R., Bess, T. D., and Smith, G. L. (1984). Infrared parameterizations and simple climate models. *J. Clim. Appl. Met.*, 23:1222–1233.

Sloan, L. C. and Pollard, D. (1998). Polar stratospheric clouds: A high latitude warming mechanism in an ancient greenhouse world. *Geophys. Res. Lett.*, 25:3517–3520.

Smagorinsky, J. (1963). General circulation experiments with the primitive equations: I. the basic experiment. *Mon. Wea. Rev.*, 91:99–164.

Smagorinsky, J., Manabe, S., and Holloway, J. L. (1965). Numerical results from a nine-level general circulation model of the atmosphere. *Mon. Wea. Rev.*, 93:769–768.

Soden, B. J., Broccoli, A. J., and Hemler, R. S. (2004). On the use of cloud forcing to estimate cloud feedback. *J. Climate*, 17:3661–3665.

Stephens, G. L. (2005). Cloud feedbacks in the climate system: A critical review. *J. Climate*, 18:237–273.

Stephens, G. L., Wood, N. B., and Gabriel, P. M. (2004). An assessment of the parameterization of subgrid-scale cloud effects on radiative transfer. part I: Vertical overlap. *J. Atmos. Sci.*, 61:715–732.

Stommel, H. (1961). Thermohaline convection with two stable regimes of flow. *Tellus*, 13:224–230.

Straus, D. M. and Ditlevsen, P. D. (1999). Two-dimensional turbulence properties of the ECMWF reanalyses. *Tellus*, 51A:749–772.

Strogatz, S. H. (1998). *Nonlinear dynamics and chaos*. Perseus Books.

Taylor, K. E. and Ghan, S. J. (1992). An analysis of cloud liquid water feedback and global climate sensitivity in a general circulation model. *J. Climate*, 5:907–919.

Thompson, S. L. and Warren, S. G. (1982). Parameterization of outgoing infrared radiation derived from detailed radiative calculations. *J. Atmos. Sci.*, 39:2667–2680.

Thorndike, A. S. (1992). A toy model linking atmospheric thermal radiation and sea ice growth. *J. Geophys. Res.*, 97(C6):9401–9410.

Trenberth, K. E. and Caron, J. M. (2001). Estimates of meridional atmosphere and ocean heat transports. *J. Climate*, 14:3433–3443.

Vavrus, S. J. (2004). The impact of cloud feedbacks on arctic climate under greenhouse forcing. *J. Climate*, 17:603–615.

Vinnikov, K. Y., Robock, A., Stouffer, R. J., Walsh, J. E., Parkinson, C. L., Cavalieri, D. J., Mitchell, J. F. B., Garrett, D., and Zakharov, V. F. (1999). Global warming and northern hemisphere sea ice extent. *Science*, 286:1934–1937.

von Storch, H. and Zwiers, F. W. (1999). *Statistical Analysis in Climate Research*. Cambridge University Press, 494 pp.

von Storch, J.-S. (2004). On statistical dissipation in GCM-climate. *Clim. Dyn.*, 23:1–15.

Walsh, J. E., Kattsov, V. M., Chapman, W. L., Govorkova, V., and Pavlova, T. (2002). Comparison of arctic climate simulations by uncoupled and coupled global models. *J. Climate*, 15(12):1429–1446.

Wang, W.-C. and Stone, P. H. (1980). Effect of ice-albedo feedback on global sensitivity in a one-dimensional radiative-convective climate model. *J. Atmos. Sci.*, 37:545–552.

Warren, S. G. and Schneider, S. H. (1979). Seasonal simulation as a test for uncertainties in the parameterizations of a Budyko-Sellers zonal climate model. *J. Atmos. Sci*, 36:1377–1391.

Washington, W. M. and Meehl, G. A. (1984). Seasonal cycle experiment on the climate sensitivity due to a doubling CO_2 with an atmospheric general circulation model coupled to a simple mixed-layer ocean model. *J. Geophys. Res.*, 89:9475–9503.

Watterson, I. G., O'Farrel, S. P., and Dix, M. R. (1997). Energy and water transport in climates simulated by a general circulation model that includes dynamic sea ice. *J. Geophys. Res.*, 102(D10):11027–11037.

Wetherald, R. T. and Manabe, S. (1988). Cloud feedback processes in a general circulation model. *J. Atmos. Sci.*, 45:1397–1415.

Williamson, D. L. (1999). Convergence of atmospheric simulations with increasing horizontal resolution and fixed forcing scales. *Tellus*, 51A:663–673.

Williamson, D. L., Kiehl, J. T., and Hack, J. J. (1995). Climate sensitivity of the NCAR Community Climate Model (CCM2) to horizontal resolution. *Clim. Dyn.*, 11:377–397.

Zachos, J. C., Pagani, M., Sloan, L. C., Thomas, E., and Billups, K. (2001). Trends, rhythms and aberrations in global climate 65 Ma to present. *Science*, 292:686–693.

Zachos, J. C., Stott, L. D., and Lohmann, K. C. (1994). Evolution of early Cenozoic marine temperatures. *Paleoceanogr.*, 9(2):353–387.

Zhang, M. H., Hack, J. J., Kiehl, J. T., and Cess, R. D. (1994). Diagnostic study of climate feedback processes in atmospheric general circulation models. *J. Geophys. Res.*, 99(18):5525–5538.

Zhang, X., Walsh, J. E., Zhang, J., Bhatt, U. S., and Ikeda, M. (2004). Climatology and interannual variability of Arctic cyclone activity: 1948–2002. *J. Climate*, 17:2300–2317.

Zhang, Y. and Wang, W.-C. (1997). Model-simulated northern winter cyclone and anticyclone activity under a greenhouse warming scenario. *J. Climate*, 10:1616–1634.